

X-ray and Radio Variability of Cygnus X-1

Dissertation
zur Erlangung des Grades eines
Doktors der Naturwissenschaften
der Fakultät für Mathematik und Physik
der Eberhard-Karls-Universität Tübingen

vorgelegt von

Thomas Gleißner

aus Weiden i. d. OPf.
2004

Selbstverlegt von: Th. Gleißner, Hegelstr. 38, 72108 Rottenburg
Tag der mündlichen Prüfung: 14. Juni 2004
Dekan: Prof. Dr. H. Müther
1. Berichterstatter: Prof. Dr. R. Staubert
2. Berichterstatter: Prof. Dr. K. Werner

Zusammenfassung

Gleißner, Thomas

Variabilität von Cygnus X-1 im Röntgen- und Radiobereich

Stellare Schwarze Löcher und Neutronensterne, sogenannte kompakte Objekte, sind Endstadien in der Entwicklung massiver Sterne mit mehr als ~ 8 Sonnenmassen. Falls die Masse eines kompakten Objekts größer ist als die theoretische Grenzmasse eines Neutronensterns, ist im Rahmen der Allgemeinen Relativitätstheorie ein Schwarzes Loch die logische Konsequenz.

Cygnus X-1 ist ein Röntgendoppelstern, der aus einem O-Überriesen und einem Schwarzen Loch besteht, das von seinem Begleiter Masse akkretiert. Ein Kennzeichen derartiger Systeme ist die starke Emission von Röntgenstrahlung mit hoher zeitlicher und spektraler Variabilität. Grundsätzlich werden zwei Zustände unterschieden, die man als *hard state* und *soft state* bezeichnet.

Obwohl Cygnus X-1 zu den am besten untersuchten Schwarzloch-Röntgendoppelsternen zählt, ist die genaue Geometrie dieser, wie auch anderer derartiger Quellen nach wie vor ungeklärt. Fester Bestandteil aller Modelle ist eine Massenakkretionsscheibe, die weiche Röntgenstrahlung abgibt. Weniger Konsens herrscht in Bezug auf den Ursprung der harten Röntgenstrahlung im *hard state*. Die Mehrheit der bisherigen Modelle nimmt Bereiche an, in denen weiche Photonen aus der Akkretionsscheibe durch inverse Comptonstreuung in harte Röntgenstrahlung umgewandelt werden. In den letzten Jahren wurden im Radiobereich zunehmend Masseausflüsse von Schwarzloch-Röntgendoppelsternen, sogenannte Jets, entdeckt. Neben offenen Fragen zu ihrer Entstehung ist noch ungeklärt, inwieweit Jets zur Röntgenstrahlung beitragen.

In dieser Dissertation wird die variable Emission von Cygnus X-1 im Röntgen- und im Radiobereich untersucht. Dazu werden eine langjährige Beobachtungsreihe des Röntgensatelliten RXTE sowie simultane Radiobeobachtungen des Ryle Telescope in Cambridge (UK) analysiert.

Nachdem im Kapitel 1 auf die oben skizzierten Grundlagen eingegangen wird, widmet sich das Kapitel 2 den mathematischen Methoden zur Beschreibung von veränderlichen Signalen mit Hilfe der Fourieranalyse und stellt theoretische Modelle für die der Variabilität zugrunde liegenden physikalischen Mechanismen vor. Neben phänomenologischen Ansätzen wie dem Shot-Noise-Modell wird auch eine erst vor kurzem im Röntgenbereich gefundene lineare Beziehung zwischen Variabilität und Fluss behandelt.

Im Kapitel 3 wird diese Korrelation am Beispiel von Cygnus X-1 genauer untersucht. Es wird gezeigt, dass sie auf allen Zeitskalen > 5 s, sowohl im *hard state* als

auch im *soft state*, Gültigkeit besitzt. Die Tatsache, dass diese lineare Beziehung, deren Steigung k die Stärke der Variabilität widerspiegelt, nicht durch den Nullpunkt verläuft, sondern einen Abschnitt C auf der Flussachse markiert, ist ein Indiz dafür, dass die Röntgenlichtkurve von Cygnus X-1 z.B. aus einer konstanten und einer variablen Komponente besteht, oder dass eine konstante Variabilitätskomponente vorliegt. Die Beziehung zwischen diesen beiden angenommenen Komponenten kann durch eine fundamentale Abhängigkeit von k und C vom Mittelwert des Flusses beschrieben werden.

Die beiden folgenden Kapitel beschäftigen sich mit Korrelationen zwischen der Radio- und der Röntgenemission, wie sie in vielen Schwarzsloch-Röntgendoppelsternen mit Jets, den sogenannten Mikroquasaren, beobachtet werden.

Das Kapitel 4 rekapituliert einige Grundlagen der Radioastronomie, fasst das bisherige Wissen über die Radioemission aus den Jets der Mikroquasare zusammen und stellt mögliche physikalische Szenarien vor, die zu den beobachteten Radio-Röntgen-Korrelationen führen könnten.

In Kapitel 5 werden simultane Röntgen- und Radiobeobachtungen von Cygnus X-1 unter dem Aspekt von Korrelationen auf kurzen (= Minuten bis ~ 5 Stunden) und langen Zeitskalen (= Tage bis Monate) ausgewertet. Die in der Forschung schon länger bekannten Korrelationen auf langen Zeitskalen können, besonders bei harten Energien, mit dem vorliegenden Datensatz bestätigt werden. Für Korrelationen auf kurzen Zeitskalen, wie sie z.B. bei GRS 1915+105, einem anderen Schwarzsloch-Röntgendoppelstern beobachtet werden, gibt es dagegen keine Anhaltspunkte. Vielmehr müssen bei Cygnus X-1 scheinbare Korrelationen auf kurzen Zeitskalen als zufälliges Resultat von weißem Rauschen gedeutet werden. Interpretiert man diese Ergebnisse als Zusammenbruch der Korrelationen auf kurzen Zeitskalen, so führt dies zur Abschätzung einer relativ niedrigen Geschwindigkeit des Jets von Cygnus X-1.

Im letzten Kapitel 6 werden die Kernpunkte dieser Arbeit zusammengefasst und ein kurzer Ausblick gegeben.

Abstract

Gleissner, Thomas X-ray and Radio Variability of Cygnus X-1

Stellar black holes and neutron stars, so-called compact objects, are the final stages in the evolution of massive stars with more than ~ 8 solar masses. If the mass of a compact object is greater than the theoretical mass limit of a neutron star, the existence of a black hole is the logical consequence within the framework of the general relativity theory.

Cygnus X-1 is an X-ray binary which consists of an O-type supergiant and a black hole accreting mass from its companion. One characteristic of such systems is the powerful emission of temporally and spectrally variable X-ray radiation. Basically, the system can be found in either of two states, referred to as *hard state* and *soft state*.

Although Cygnus X-1 is to be counted among the best studied black hole X-ray binaries, its exact geometry is not clear, just as for similar sources. A definite constituent of all models is a mass accretion disk releasing soft X-rays. Less agreement exists with regard to where the hard X-rays originate during the *hard state*. Most models assume regions where soft disk photons are energized by inverse Compton scattering to hard X-rays. In recent years, several X-ray binaries have been detected to possess matter outflows, so-called jets. Apart from open questions concerning their formation, the contribution of jets in the X-ray regime remains to be clarified.

The subject of this thesis is the variable emission of Cygnus X-1 in the X-ray and in the radio band. The analyzed data span several years and were taken in an X-ray monitoring with the satellite RXTE and simultaneous radio observations with the Ryle Telescope at Cambridge (UK).

After an introductory description of the basic issues in chapter 1, the following chapter 2 summarizes the mathematics to describe variability by Fourier analysis as well as theoretical models of variability and of the underlying physical mechanisms. Apart from phenomenological approaches like the shot noise model, a recently discovered linear relationship between the rms variability and the flux of X-ray lightcurves, the so-called rms-flux relation, is outlined.

In chapter 3 this relation is investigated using the lightcurves of Cygnus X-1. It is shown that the relationship is valid on all time scales > 5 s, both in the *hard state* and in the *soft state*. The existence of a non-zero intercept C on the flux axis argues for two lightcurve components, for example, one variable and one non-variable component, or a possible constant variability component. The slope k of the linear rms-flux relation mirrors the fractional variability. The relationship between these two hypothesized components can be described by a fundamental dependence of k and C with

long term averages of the flux.

The two following chapters deal with radio–X-ray correlations as they are observed in many black hole X-ray binaries with jets, the so-called microquasars.

Chapter 4 reviews basics of radio astronomy, gives a summary of the radio emission from the jets of microquasars, and introduces possible physical scenarios which could cause the observed radio–X-ray correlations.

In chapter 5 simultaneous X-ray and radio observations of Cygnus X-1 are studied with regard to correlations on short (= minutes to ~ 5 hours) and long time scales (= days to months). The existence of correlations on long time scales, as observed in many microquasars, can be confirmed also with the used database of Cygnus X-1, particularly at hard energies. On the other hand, there is no indication for correlations on short time scales, as they are known, e.g., for GRS 1915+105, another prominent black hole X-ray binary. Apparent correlations on short time scales in the lightcurves of Cygnus X-1 are rather the coincidental outcome of white noise statistics. Interpreting this result as a breakdown of radio–X-ray correlations on shorter time scales, this sets a limit to the speed of the jet of Cygnus X-1.

The last chapter 6 summarizes the main issues of this thesis and gives a brief outlook.

Contents

1	The Nature of Black Hole X-ray Binaries	10
1.1	The Black Hole	10
1.2	Black Hole X-ray Binaries	13
1.3	Accretion	14
1.3.1	Roche Lobe Overflow	17
1.3.2	Wind Accretion	18
1.3.3	Outflows	19
1.4	States	20
1.4.1	Comptonization	21
1.4.2	The Hard State	22
1.4.3	The Soft State	23
1.4.4	The Intermediate State	24
1.5	Models	24
1.5.1	Comptonization Models	25
1.5.2	The ADAF	27
1.5.3	The Jet Model	28
1.6	Observing the Prototype: Cygnus X-1	30
1.6.1	System Parameters	30
1.6.2	Data Acquisition with <i>RXTE</i>	32
1.6.3	Radio Observations with the Ryle Telescope	35
I	X-ray Variability	37
2	Variability of BH XRBs	39
2.1	Introduction	39
2.2	Measuring Variability	39
2.2.1	Fourier Analysis	39
2.2.2	Power Spectral Density	40
2.2.3	Noise and Dead Time	41
2.3	Variability Patterns and Variability Models	41

2.3.1	Shot Noise Models	42
2.3.2	Quasi-Periodic Oscillations	44
2.3.3	Magnetic Reconnection	46
2.3.4	The Thundercloud Model	46
2.3.5	The Propagation Model	46
2.3.6	The rms-Flux Relation	48
3	The rms-Flux Relation in Cygnus X-1	49
3.1	Observations and Data Analysis	49
3.1.1	Data Extraction	49
3.1.2	Computation of the rms Variability	50
3.1.3	rms versus Flux	51
3.1.4	Buffer Overflows in <i>RXTE</i> Binned Data Modes	53
3.2	Results	55
3.2.1	Evolution of Slope and Intercept	55
3.2.2	The rms-Flux Relation in the Hard and Soft State and During “Failed State Transitions”	59
3.2.3	Spectral Dependence of the rms-Flux Relation	62
3.2.4	The rms-Flux Relation on Short Time Scales	66
3.3	Discussion	67
3.3.1	The Origin of the rms-Flux Relation	67
3.3.2	The Long Term rms-Flux Relation	69
3.3.3	The hard state $k-C-\langle F \rangle$ fundamental plane	70
II	Radio–X-ray Relations	71
4	Radio Emission of BH XRBs	73
4.1	Radio Emission	73
4.1.1	Basic Issues of Radio Observations	73
4.1.2	Thermal Radiation	75
4.1.3	Synchrotron Radiation	76
4.2	Radio–X-ray Observations of BH XRBs	79
4.2.1	On Long Time Scales	80
4.2.2	On Short Time Scales	81
4.3	Jets	83
4.3.1	Relativistic Effects	83
4.3.2	Production Mechanisms	85
4.3.3	The Jet of Cygnus X-1	88
4.4	Models of Radio–X-ray Correlations	90

4.4.1	The Coronal Outflow Model	91
4.4.2	The Depletion Model	91
4.4.3	The Unifying Jet Model	92
5	Radio–X-ray Correlations of Cygnus X-1	94
5.1	Observations and Data Analysis	94
5.2	Sensitivity of the Procedure: Application to GRS 1915+105 . . .	96
5.3	Results for Cygnus X-1	100
5.3.1	Short Term Correlations	100
5.3.2	Rescaling GRS 1915+105 to the Level of Cygnus X-1 . .	102
5.3.3	Long Term Correlations	103
5.4	Estimating the Time Scale for Traversing the Jet	105
5.5	Discussion	108
6	Summary	110
6.1	The rms-Flux Relation	110
6.2	Radio–X-ray Correlations	111
6.3	Outlook	112
	Bibliography	113
	Acknowledgments	119
	Lebenslauf	120

CHAPTER 1

The Nature of Black Hole X-ray Binaries

“It’s black, and it looks like a hole. I’d say it’s a Black Hole.”

from a cartoon by Sidney Harris

1.1 The Black Hole

Black holes (BHs) are fascinating astronomical objects which have become a kind of symbol for highly sophisticated astrophysics in the public. Nevertheless the idea of a body which “locks” everything, even light, was already born in the 18th century, independently by Michell (1784) and by Laplace (1796). The motivation of these people becomes clearer against the background of the Newtonian theory of gravity. For an object to completely leave a celestial body with mass M and radius R , its velocity v must be equal to or greater than the escape velocity v_{escape} of that celestial body, given by

$$v_{\text{escape}} = \sqrt{\frac{2GM}{R}} \quad (1.1)$$

where G denotes the gravitational constant. When light with a wavelength λ is considered as single photons with mass $m = h/\lambda c$, then a celestial body can be imagined whose escape velocity is greater than the speed of light c , i.e., photons cannot escape from that body. With the detection of the wave character of light the idea of massive photons was forgotten, and with it the notion of any *corps obscur*¹.

It was not until the beginning of the 20th century when Albert Einstein had developed the general relativity theory (GRT) that these ideas were re-introduced as a singularity in the 4-dimensional space-time continuum. In 1916 Schwarzschild, then a German front soldier, published a solution of the GRT equations for the case of a spherical non-rotating body with mass M , featuring a singularity of the “metric” at

¹*Corps obscur*, i.e., hidden body, is the term which was used by Laplace (1796) to denote this kind of gravitationally invisible stars.

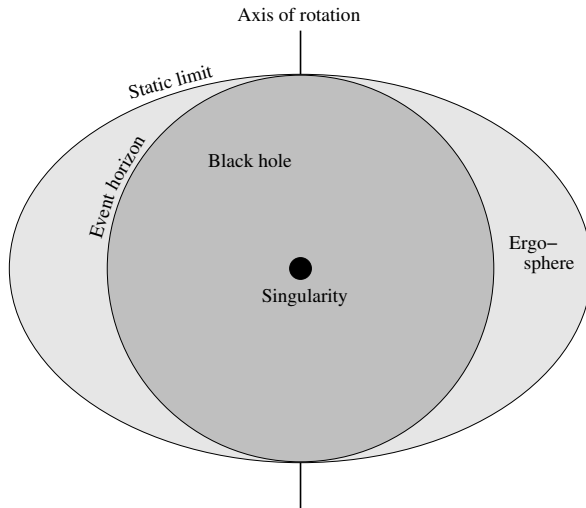


Figure 1.1: Geometry of a black hole. The event horizon at $R = R_S$ marks the area from which no signal can escape. Due to the frame-dragging effect, an ellipsoidal region within the static limit forms around a rotating BH, the ergosphere, inside of which accreting material must corotate with the BH and from which rotational energy can be extracted (after Karttunen et al. 2003, Fig. 14.9).

the Schwarzschild radius

$$R_S = \frac{2GM}{c^2} \approx 3 \text{ km} \left(\frac{M}{M_\odot} \right) \quad (1.2)$$

(Schwarzschild 1916). If the radius R of that body is smaller than R_S , neither matter nor photons – thus no information – can escape from it.

The belief that highly compact objects like this could really exist grew with the advances in the theory of star evolution that were made at that time. In 1931 Chandrasekhar’s calculations for a white dwarf suggested that beyond a mass limit of $1.4M_\odot$ the Fermi-Dirac-degenerate electron gas cannot withstand the gravitational pressure any more and the white dwarf would collapse (Chandrasekhar 1931). By 1934 the existence of a neutron star as the result of a supernova was considered possible by Baade & Zwicky (1934) and some years later Oppenheimer & Volkoff (1939) presented detailed theoretical models for this compact object. They had not failed to notice that even a neutron star – just like a white dwarf – has an upper mass limit. Due to the uncertainty with respect to the equation of state for matter denser than atomic nuclei, the Oppenheimer-Volkoff mass limit for neutron stars is thought to be in the

Table 1.1: Short Typology of Black Holes. All BH types possess mass.

BH type	angular momentum	charge
Schwarzschild	$J = 0$	$Q = 0$
Kerr	$J > 0$	$Q = 0$
Reissner-Nordström	$J = 0$	$Q \neq 0$
Kerr-Newman	$J > 0$	$Q \neq 0$

range $1.8\text{--}3 M_{\odot}$ (Shapiro & Teukolsky 1983). Beyond this limit no stable configuration to counteract gravity is possible and matter will contract to a collapsar, for which the more popular term “black hole” was established in the 1960’s².

The gravitational potential around a non-rotating massive sphere according to the Schwarzschild metric is a modification of the Newtonian theory, leading to consequences for the orbital geometry around the mass. One effect is that the innermost stable circular orbit (ISCO) is at a radius $R = 3R_S$, which plays a role in the formation of accretion disks. Another result is the advance of the periastron for an elliptical orbit. This second effect was confirmed with the orbit of Mercury, thus solving a longtime puzzle and formidably validating the GRT.

BHs have been a favorite object of study for theoreticians for many decades and more and more of their nature has been discovered (Fig. 1.1). The theorem “black holes have no hair” means they have no observable external characteristics that can be used to determine what they are like inside. The only properties a BH can possess are mass M , angular momentum J , and electric charge Q , and it can be completely specified by these three parameters (Table 1.1). In the case of a rotating BH ($J \neq 0$) the GRT predicts the dragging of inertial frames around the rotating mass. This so-called Lense-Thirring effect causes matter falling toward the spinning BH to be dragged around it (Bardeen & Petterson 1975). Hawking & Ellis (1973) and Hawking (1974, 1975) confirmed the hypothesis that the entropy of a BH is proportional to its horizon area and found that BHs can emit thermal radiation, the so-called “Hawking radiation”. Recently, Wilms et al. (2001) found spectral features that suggest the extraction of energy from a Kerr BH via the Blandford & Znajek (1977) process.

The defining characteristic of a black hole, an event horizon holding back everything inside, names the dilemma astronomers are faced with to provide direct observational evidence for this weird class of celestial bodies. The only way to “detect” a BH is by the impact it exerts on its environment. One way to identify a BH is to find a compact object with a mass well in excess of the Oppenheimer-Volkoff mass limit.

²In literature on BHs the rumor is spread that J. A. Wheeler in 1967 or 1968 was the first to refer to a collapsar as a “black hole”. However, this term has obviously been in use already years before (Rosenfeld 1964).

As it is per definitionem impossible to directly observe a BH many authors prefer to use the term BH “candidate” (BHC).

This thesis deals with observational results from Cygnus X-1, a typical representative of stellar BHs in a binary system, which have masses of the order of $10^1 M_{\odot}$ and in many cases are bright sources due to intense interactions with their companion. For stellar-mass black holes which are located in our Galaxy the acronym GBHC for galactic black hole candidate is regularly found in the literature. It is suggested, though, that the vast majority of GBHC are isolated BHs which remain undetected because hardly any radiation can theoretically be expected from them (Reynolds & Nowak 2003). Another class of BHs, the so-called supermassive BHs (SMBHs) with masses in the range of 10^6 – $10^9 M_{\odot}$, reside in the cores of active galactic nuclei (AGN), actually of most galaxies. For the existence of a SMBH in our Galactic center, designated Sgr A*, convincing evidence was supplied by Schödel et al. (2003). The formation process of the SMBHs is yet unclear, though. A third, but rather speculative class are the primordial BHs: it is possible that tiny BHs which evaporate by emitting gamma rays could have formed in the primordial universe (Page & Hawking 1976). Lastly, evidence has accumulated for a class of intermediate-mass BHs, with $M \sim 10^2$ – $10^4 M_{\odot}$, in the cores of dense stellar clusters (Miller & Colbert 2003).

More than 300 years ago, BHs were introduced as a Gedanken experiment. Today, BHs – fascinating both by their mathematical elegance, elusive character, and sheer power – are conceded a firm position in the cosmic orchestra and seem to play a major role in the symphony of the universe. In our near cosmic neighborhood we are constantly reminded of the actual existence of stellar-mass BHs by the immense X-ray emission we receive from BH binaries. The next section will deal with their properties.

1.2 Black Hole X-ray Binaries

X-ray binaries (XRBs), named for their conspicuous X-ray emission, consist of a “normal” star and a compact object. Leaving aside the white dwarf systems – also known as cataclysmic variables – where nova and dwarf nova eruptions predominantly shine in the ultraviolet and visible wavelength range, neutron star and BH X-ray binaries (BH XRBs) are characterized by enormous and highly variable X-ray emission. The compact objects are remnants of relatively massive stars that evolved in a binary. During their evolution they transferred mass to the then smaller companion, and mass transfer in the binary keeps remaining an essential process in XRBs, as is shown in section 1.3.

Spectroscopic binary stars with an assumed BH companion afford an opportunity to “weigh” the compact object. The Doppler shift of the spectral lines of the companion

star gives the radial velocity v of this binary component. In combination with the orbital period P , a lower limit for the mass of the compact object M_{compact} is provided by the mass function

$$f(M_{\star}, M_{\text{compact}}, i) = \frac{(M_{\text{compact}} \sin i)^3}{(M_{\star} + M_{\text{compact}})^2} = \frac{Pv^3}{2\pi G} \quad (1.3)$$

where M_{\star} is the mass of the companion star, and i is the inclination of the orbit. With reference to the Oppenheimer-Volkoff mass limit, a mass function $f > 3 M_{\odot}$ is considered proof of a BH. If the mass function is not available, an XRB is taken to contain a BH if the spectral and temporal characteristics of the compact object are similar to an established GBHC. In other cases emission properties may help to identify the compact object. Type I X-ray bursts, spin pulsations, or spectral single-color blackbody components are expected only from a neutron star because they require a surface to be produced (Tanaka & Lewin 1995).

Currently ~ 18 confirmed BH X-ray binaries in the Galaxy are known (McClintock & Remillard 2004). They are divided in two classes according to the mass of the secondary, i.e., star component: in low-mass X-ray binaries (LMXBs), the stellar companion with $M \leq 1M_{\odot}$ consists of a late type star (G or later), whereas high-mass X-ray binaries (HMXBs) possess an early type star companion (O or B) with $M \geq 10M_{\odot}$. The spectral type may be inferred from optical identification and/or from the mass function. Three sources, all of them HMXBs, show truly persistent activity (LMC X-1, LMC X-3, Cyg X-1), while the majority belongs to the transient sources which semi-regularly experience large amplitude outbursts followed by long periods of quiescence.

BH XRBs form a laboratory for the study of high-energy astrophysics. Their immense energy output is powered by the flow of atmospheric material from the stellar companion to the BH where it falls into the deep gravitational well of this compact object, setting free its potential energy in the form of radiation, mainly in the X-ray range. Details of these processes are given in the next section.

1.3 Accretion

Accretion, i.e., the growth of a body by means of the gravitational force it exerts on surrounding matter, is a common mechanism in the universe. An in-depth description of accretion can be found in Shapiro & Teukolsky (1983), Frank et al. (1992), and King (1995). Due to the conservation of omnipresent angular momentum, particles cannot fall radially on the accreting body but form an accretion disk (AD), as can be seen, e.g., in very young stars (T Tauri), in AGN, in proto-planetary systems, and in

XRBs, where they circle the accretor on quasi-Keplerian orbits with angular velocity

$$\Omega_K \approx \sqrt{GM/R^3}, \quad (1.4)$$

where R is the radius of the orbit around the accretor. In many cases, the accreting matter is limited very closely to the orbital plane so that the disk flow can be considered as two-dimensional, known as the thin disk approximation. This thin disk is relatively cold and can be regarded as optically thick (apart from the innermost region of the disk). Because of differential rotation of the disk, the particles lose angular momentum due to turbulent friction (most likely involving magnetic fields) between adjacent layers, and spiral inward. The frictional force F which is transmitted to an area A is given by

$$F = \rho \nu A dv/dx \quad (1.5)$$

where ρ is the mass density, ν is the kinematic viscosity, and dv/dx is the velocity gradient perpendicular to A . It was found that the common molecular viscosity is far too weak to account for the accretion disk particles to lose angular momentum in an efficient way (Pringle 1981). In absence of an exact theory of turbulent viscosity, Shakura & Sunyaev (1973) introduced the parameter $\alpha \leq 1$, which is related to the viscosity ν by

$$\nu = \alpha c_s H \quad (1.6)$$

where c_s is the sound speed, and H is the typical vertical scale-height of the disk, i.e., broadly speaking the half-thickness of the disk, which is related to c_s and Ω_K as

$$H \simeq \frac{c_s}{\Omega_K} \quad (1.7)$$

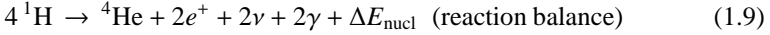
(see, e.g., Frank et al. 1992). The angular momentum of the particles is transported outward and – spiraling into the deep potential well of the central object – a considerable fraction of the potential energy of the particles is dissipated as heat locally within the disk, and subsequently emitted as thermal radiation. The other fraction, one half of the potential energy of the particles, is transformed into kinetic energy (Tanaka & Lewin 1995), continuously accelerating the particles as they approach the innermost region around the compact object, where most of the gravitational energy is released. This standard picture of an AD is known as α -disk or Shakura-Sunyaev-disk.

Apart from the thin disk approximation, several other solutions to the hydrodynamic equations of the accretion flow are known, which have given rise to a multitude of geometric/physical accretion models for GBHCs (see section 1.5). Changes of luminosity and of other system parameters like spectral energy distribution or variability observed from GBHCs, apparently are related to different accretion conditions (see section 1.4).

The enormous luminosities observed from AGN or XRBs are powered by the release of potential energy through accretion. Accretion is by far the most efficient astrophysical energy source, even in comparison to nuclear fusion, as will be shown by the following estimation. The accretion of mass m from infinity to the surface of a neutron star with mass $M \sim 1M_{\odot}$ and radius $R \sim 10$ km sets free potential energy of

$$\Delta E_{\text{acc}} = \frac{GMm}{R} \cong 1.3 \times 10^{20} \text{ erg g}^{-1} \quad (1.8)$$

The typical astrophysical nuclear reaction of hydrogen fusion to helium, the proton-proton chain



releases a maximum energy yield of $\Delta E_{\text{nucl}} \sim 0.007mc^2 \cong 6.3 \times 10^{18} \text{ erg g}^{-1}$, i.e., only about a twentieth of ΔE_{acc} . In case of a neutron star it is possible that the total of ΔE_{acc} is set free, as there is a surface where the kinetic energy of the mass can be transformed to thermal and then radiation energy. In case of a BH, however, the mass and its kinetic energy is lost beyond the event horizon. In Newtonian theory, the total energy of a Keplerian orbit according to the virial theorem is equal to $GMm/2R = \Delta E_{\text{acc}}/2$. As this energy is lost to the BH, this gives an upper estimate to the energy that is set free in the disk around the BH.

An order-of-magnitude estimate for the accretion luminosity with great practical importance is obtained when making the assumption that the steady accreting material is mainly hydrogen and fully ionized. Then radiation from the central object exerts an outbound force on the spherically symmetrically accreting material, mainly the electrons, via Thomson scattering, whereas gravitation, acting on electron-proton-pairs, drags inwards. At the Eddington limit

$$L_{\text{Edd}} = 4\pi GMm_p c / \sigma_T \cong 1.3 \times 10^{38} (M/M_{\odot}) \text{ erg s}^{-1} \quad (1.10)$$

with the proton mass m_p and the Thomson scattering cross section σ_T , these two contrary forces cancel and the accretion process stops.

If the fraction of released gravitational potential energy that is transformed to radiation in the AD is given by the dimensionless efficiency quantity η , the accretion luminosity is

$$L_{\text{acc}} = 2\eta GM\dot{m}/R_S = \eta \dot{m}c^2 \quad (1.11)$$

where \dot{m} is the accretion rate (Frank et al. 1992). For a solar mass neutron star $\eta \sim 0.15$. For a BH, a precise calculation in the GRT metric results in typical efficiency values of $\eta = 0.057\text{--}0.42$ for Schwarzschild and Kerr type, respectively (Shapiro & Teukolsky 1983). Inserting realistic values in eq. (1.11) ($\eta \approx 0.1$, $\dot{m} \approx 10^{-9} M_{\odot} \text{ a}^{-1}$)

delivers a typical accretion luminosity of $L_{\text{typ,BH}} \sim 10^{37} \text{ erg s}^{-1}$ in a BH binary system. Assuming the disk thermally radiating as a black body and a BH mass of $10 M_{\odot}$, the luminosity of a typical accreting BH, $L_{\text{typ,BH}}$, corresponds to a typical photon energy of $\sim 0.5 \text{ keV}$ ($T_{\text{bb}} \approx 5 \times 10^6 \text{ K}$), which can be derived from equating

$$\sigma T_{\text{bb}}^4 = L_{\text{typ,BH}}/4\pi R_{\text{S}}^2 \quad (1.12)$$

where σ is the Stefan-Boltzmann constant. If for the thin disk approximation it is assumed that all released gravitational potential energy is emitted locally as blackbody radiation, the temperature of the plasma inside the disk is $T(r) \propto r^{-3/4}$, where r is the distance to the central object. The disk temperature increases from a low value near the outer edge to a maximum T_{in} at the inner edge of the disk at $R_{\text{in}} \approx 3R_{\text{S}}$, so most of the luminosity is set free in the central zone of the AD (Tanaka & Lewin 1995).

In order to maintain the luminosity on long time scales, the accreted material that is lost to the BH has to be substituted. In the case of an isolated BH, there is large uncertainty about the efficiency of accretion from the interstellar medium (ISM), setting free low-level X-ray radiation (Bondi & Hoyle 1944; Bondi 1952; Reynolds & Nowak 2003). In an XRB the companion star can deliver gaseous matter mainly in two ways which are discussed in the next paragraphs.

1.3.1 Roche Lobe Overflow

To study the equipotential surfaces in a close binary with angular velocity ω and masses M_{\star} and M_{compact} it is convenient to describe the system in a frame of reference rotating with the binary system, where the stars keep a fixed position. Under these conditions, it is possible to derive the potential (gravitational plus centrifugal) and its corresponding equipotential surfaces. In a point with distance r_{\star} to the center of M_{\star} , distance r_{compact} to the center of M_{compact} , and distance z to the rotating axis, the potential is given by

$$\Phi = -G \left(\frac{M_{\star}}{r_{\star}} + \frac{M_{\text{compact}}}{r_{\text{compact}}} \right) - \frac{1}{2} z^2 \omega^2 \quad (1.13)$$

(Unsöld & Baschek 2002). Close to each companion, the potential is dominated by the gravitational potential of each mass, thus the surfaces are almost spherical. As one moves farther from a center of mass, the tidal and centrifugal forces increase, and the surfaces become flatter and more elongated. The first common equipotential surface that is shared by each companion is shaped like an hour glass and is called Roche surface, the two volumes enclosed by this surface are the Roche lobes. The Roche surface intersects between the companions at the gravitational potential saddle point, the inner Lagrangian point L_1 , forming a pass between the Roche lobes. Beside L_1 , Lagrangian points L_2 – L_5 exist near the binary system, where the gravitational forces

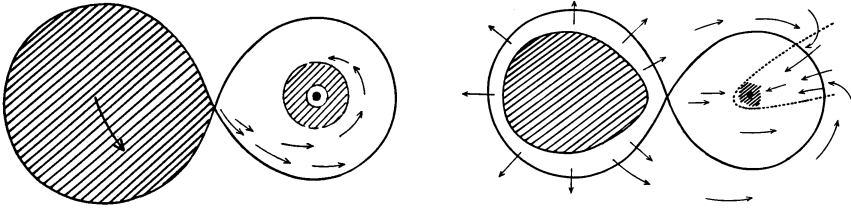


Figure 1.2: Mass accretion in an XRB can work in two ways: via Roche lobe overflow (left) or via star wind (right). In some systems as, e.g., Cyg X-1, a situation intermediate between accretion by Roche lobe overflow and pure, spherical wind accretion is found (Friend & Castor 1982).

of the two masses cancel out. In the case of our solar system, these Lagrangian points, especially L_4 and L_5 , represent ideal parking positions for satellites and are favored places to find asteroids, the so-called Trojans. Farther out each equipotential surface envelops both companions.

If the normal companion star evolves to a giant and fills its Roche lobe, matter is spilled across L_1 into the Roche lobe of the compact object, where it is captured by its gravitational force and accreted via an AD. In this process, the mass-donating star can lose mass at rates of $3 \times 10^{-8} - 3 \times 10^{-4} M_{\odot} \text{ a}^{-1}$ (Shapiro & Teukolsky 1983). Apart from Roche lobe overflow, which is the best understood process of feeding the AD, the mechanism of wind accretion is rather important with HMXB, among various other possibilities, and will be discussed next.

1.3.2 Wind Accretion

In XRB systems where the normal companion star is of spectral type O or B with strong stellar wind loss rates of $10^{-6} - 10^{-5} M_{\odot} \text{ a}^{-1}$ (Frank et al. 1992), wind accretion can be a relevant process in case the mass-losing star does not fill its Roche lobe. A small fraction ($\leq 0.1\%$; Shapiro & Teukolsky 1983) of the highly supersonic plasma that is symmetrically ejected from the early type star passes the compact object close enough to get caught in its gravitational potential well and contributes to the accretion material. The formation of an AD around the accretor is impaired by the little angular momentum the stellar wind carries, and if an AD forms, it will be smaller than in the case of Roche lobe overflow.

The strength of the wind loss rate is usually measured by the strength of the stellar wind emission in $H\alpha$ (Puls et al. 1996; Gies et al. 2003). In sparse stellar winds the $H\alpha$ spectral line is present as an absorption line, and grows to an emission line due to recombination near the stellar photosphere in the case of dense winds.

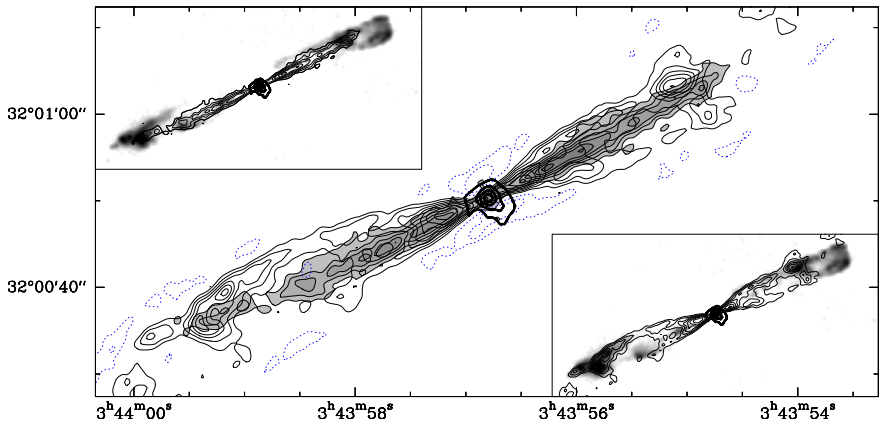


Figure 1.3: The high-velocity CO jet of HH 211, a young low-mass protostar, taken at 1.3 mm with IRAM. The small panels show the CO jet superimposed on H₂ line emission (Richer et al. 2000, Fig. 1).

1.3.3 Outflows

Collimated outflows from accreting objects seem to be a common feature in the universe. The observation of very young stars has revealed that ADs are closely connected to bipolar outflows along the rotation axis of the AD (Fig. 1.3). Once the AD, which reaches until close to the central object and feeds material into the jets, has dissolved, the jets disappear (Bachiller 1996). The only readily available energy source for the expulsion of matter at very high velocities is the gravitational potential energy set free during the accretion process. The underlying mechanism for the jet collimation seems to be the rotation of the AD by which a helical configuration of the magnetic field is built up, possibly assisted by external pressure (cf. section 4.3.2).

Radio-emitting jets from galactic cores had long been a familiar phenomenon in radio astronomy, when the “kinematic model” proposed by Fabian & Rees (1979) and Milgrom (1979) as explanation for the periodically Doppler-shifted Balmer and He lines of SS 433 provided the link between AGN and XRBs (Margon 1984), making come true theoretical work that predicted outflows from compact objects (e.g., Shakura & Sunyaev 1973). At the latest since the discovery of the superluminal jet source GRS 1915+105 it has become generally accepted that our Galaxy harbors a class of XRBs with relativistic outflows (Fender et al. 1999). They show an intriguing similarity to quasars and, more generally, to AGN except for the fact that they

are a factor 10^6 – 10^9 smaller in mass. Thus they have been referred to as ‘micro-quasars’ (MQs; Mirabel et al. 1998). One of the key properties of MQs is the ejection of matter at relativistic speeds in jets. Non-thermal radio emission is detected from these outflows, which due to its properties is thought to be synchrotron radiation from relativistic electrons in the jet (see chapter 4).

These outflows can be divided in two categories: the continuous jets which appear as uninterrupted stretched emission regions, and the blobby ejections, with separated emission knots, which bear similarity with beads on a thread. Jets and radio emission are no constant feature of X-ray binaries. They are subject to change depending on the spectral state of the central object. The presence of radio emission seems to be related to the hard state whereas the soft state shows a considerable reduction of radio emission or even its quenching below detectability (cf. section 1.4).

1.4 States

GBHCs are generally found in one of several states which are mainly characterized by their X-ray and radio spectral and timing properties (see, e.g., Nowak 2003, and references therein). These states are spectrally distinguished by different X-ray broad-band luminosity, L , and by the different relative contribution of a soft, quasi-thermal and a hard, power-law-like spectral component to this luminosity. These two basic components are generally associated with soft thermal radiation from a cold AD, and high-energy emission produced by upscattering of photons in a hot environment, respectively (e.g., Sunyaev & Trümper 1979).

Figure 1.4 gives a schematic view of the four main states. In the very high state (VHS), L is close to the Eddington luminosity, L_{Edd} , and both spectral components contribute about equally. In the high/soft state, L is at a slightly lower level, the soft component dominates the spectrum, and the weak power-law component has a high photon index Γ . In the hard state, the two spectral components have changed their roles, this time with a dominant hard power-law and a very weak or even absent soft part contributing to a relatively low luminosity $L \lesssim 0.05 L_{\text{Edd}}$. In the transition between the hard and the soft state, occurring at a threshold luminosity of $\sim 10^{37}$ erg s $^{-1}$, GBHCs are sometimes observed in the so-called intermediate state, which has similar features to the VHS, and where the variability and X-ray spectral properties are mostly intermediate between the hard and the soft state (Belloni et al. 1996). Additionally, some GBHCs, especially transient sources, display a quiescent state with very low luminosity.

Transitions between different states are now usually associated with changes in the mass accretion rate, providing a link to the different observed levels of luminosity (Esin et al. 1997). This concept explains the high luminosity of the soft state with an

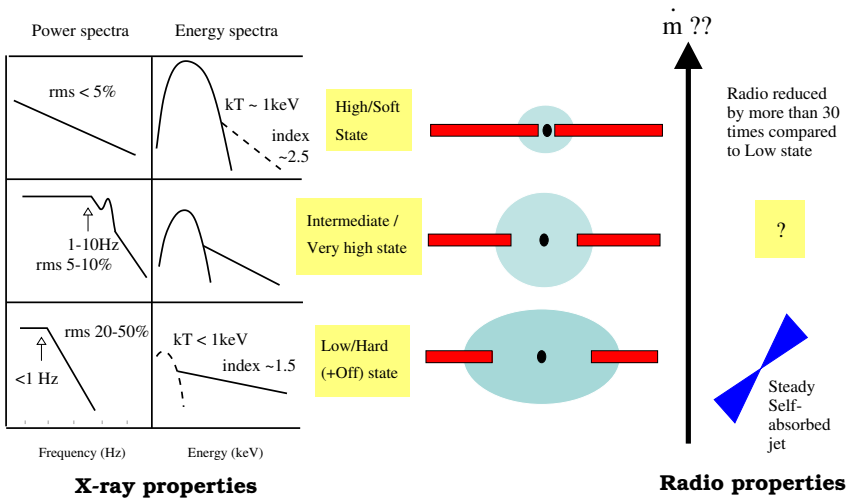


Figure 1.4: Diagram summarizing the main characteristics of the different states of BH XRBs. Major differences found in the observational data concern the extent of variability and the spectral shape (left). The physical interpretation results in different geometries, associated with a variation of the mass accretion rate \dot{m} (center). Since the consolidation of the MQ concept, radio features are assumed to be an integral part of the state typology (right) (Fender 2002, Fig. 4).

AD that reaches inwards until the ISCO, providing good conditions for an effective accretion process. In contrast to this, the AD of the hard state is truncated at a distance of several hundred R_S and at smaller distances to the BH replaced by a geometrically thick, optically thin hot medium, leading to a lower accretion rate and luminosity.

Since the physical process of scattering photons to higher energies by hot electrons, the so-called Comptonization, is indispensable for a deeper understanding of the states of GBHCs, its basic ideas are briefly outlined in the following section.

1.4.1 Comptonization

Compton scattering is the scattering of a photon by an electron. As the results can be explained within the framework of conservation of energy and momentum, Compton scattering supplies evidence for the wave-particle duality of light. The energy loss of the incident photon is dependent only on the scattering angle θ and its initial energy $E = h\nu$, when the electron is taken to be initially at rest. The energy of the photon

after the scattering process, E' , is then given by

$$E' = \frac{E}{1 + \frac{E}{m_e c^2} (1 - \cos \theta)} \quad (1.14)$$

If the scattering electrons are not stationary, but obey a Maxwellian velocity distribution (Rybicki & Lightman 1979, eq. 10.60)

$$f(v)dv = \sqrt{\frac{2}{\pi}} \left(\frac{m_e}{kT_e} \right)^{3/2} v^2 \exp(-m_e v^2 / 2kT_e) dv \quad (1.15)$$

where $kT_e/m_e c^2 \ll 1$, it can be shown that, averaging over all solid angles, the average relative energy change of the photon is given by

$$\frac{\Delta E}{E} \cong \frac{4kT_e - E}{m_e c^2} \quad (1.16)$$

In the case of $E < 4kT_e$, the photons undergo inverse Compton scattering, on average gaining energy in their encounter with the electrons. The process of multiple inverse Compton scattering events is referred to as Comptonization. The electron cloud is cooled by this process.

1.4.2 The Hard State

The hard state spectrum is similar to the high-energy spectra of AGN and is characterized by a power-law with photon index Γ and an exponential cutoff with folding energy E_f

$$\frac{dN}{dE} \propto E^{-\Gamma} \exp(-E/E_f) \quad (1.17)$$

where N is the number of photons detected. Typical values of the parameters are $\Gamma \approx 1.4-1.8$ and $E_f \approx 250$ keV.

This hard power-law component represents the signature of a physical process which releases highly energized photons. It is usually modeled by thermal Comptonization of cool seed photons to very high energies by an optically thin, hot plasma with temperatures $kT > 100$ keV (Thorne & Price 1975; Shapiro et al. 1976; Sunyaev & Trümper 1979; Dove et al. 1998). Unsaturated inverse Compton scattering, i.e., the photons on average gain energy by each scattering event, predicts a power-law modified by an exponential cutoff at energies $E \approx kT_e$, which fits well to the observed spectrum of BH XRBs. The low-energy seed photons are thought to be supplied by the cold AD, while the hot electron cloud, which in analogy to the extremely hot and rarefied plasma of the solar corona is called accretion disk corona, is situated somewhere in its neighborhood. The exact geometric arrangement of these two components, disk and corona, is still debated.

Two main properties of the plasma medium that determine the shape of the Comptonized spectrum are the electron temperature T_e , also referred to as coronal temperature T_c , and its optical depth τ . For a given T_e , an increase in τ results in a harder power-law. For a given τ , an increase in T_e results in both a harder power-law and an increase in the folding energy E_f . Thus E_f provides an estimate of T_e ($E_f \approx 50$ keV gives a plasma temperature of $T_e \approx 10^6$ K), and the photon index Γ provides an estimate of the opacity τ .

Below 1 keV the spectrum may show a soft excess: a quasi-thermal component which is thought to be radiation from a cold, optically thick AD with $kT_{bb} \approx 0.1$ – 0.3 keV. Additionally, a weak iron line feature (Fe $K\alpha_{1,2}$) at ~ 6.4 keV and a slight hump between 10 and 50 keV are present in the spectrum.

Iron is the end point of thermonuclear fusion, making it a relatively abundant element in the universe. Also, the K fluorescence yield increases with atomic number Z and is ~ 0.34 for neutral iron (Kortright 2001). This accounts for the prominence of the Fe $K\alpha_{1,2}$ fluorescent lines in many sources, excited by X-ray irradiation of relatively cold, dense gas very close to the central compact object.

An optically thick cool disk irradiated with X-ray photons in the energy range 0.1 keV–1 MeV reflects about 10% of the incoming photons. The rest is absorbed and re-radiated as soft radiation, the so-called reprocessing. The shape of the reflected spectrum is a result of the energy dependence of Compton scattering and photo absorption. For $E \gg 15$ keV Compton scattering with $-\Delta E/E \propto E$ is the dominant process, i.e., high energy photons lose much more energy than low energy photons. For the reflection spectrum this means that the absorptivity is stronger at high energies and decreases for lower energies. For $E < 10$ keV photo absorption dominates over other interactions, with an absorptivity $\propto E^{-3}$. Both processes together provide that high energy photons are Compton scattered to low energies, photons at low energies are absorbed, forming a reflection hump in the shape of the reflection spectrum.

In the hard state, MQ sources show a considerable radio activity which is assumed to be driven by synchrotron radiation from a plasma outflow off the central BH. Also, the X-ray emission is significantly more variable than in the soft state, at a root mean square (rms) variability of $\sim 40\%$ (Reynolds & Nowak 2003, for a definition of rms variability see section 2.2.2).

At energies $\lesssim 10$ keV, the flux is relatively low in the hard state. As the first generation X-ray detectors were limited to this lower energy range, this state historically is also called the low state.

1.4.3 The Soft State

In analogy to the hard/low state, the soft state is also referred to as high state. The spectrum is dominated by a soft quasi-thermal component which can be described by a black-body spectrum with a characteristic temperature of ≈ 0.5 – 3 keV. The thermal

X-ray spectrum in the soft state is generally associated with a geometrically thin, optically thick accretion disk (Shakura & Sunyaev 1973; Novikov & Thorne 1973; Gierliński et al. 1999). In some sources, a highly variable power-law component with $\Gamma \approx 2.0\text{--}2.5$ has to be added (e.g., in LMC X-3, a HMXB BHC with $\Gamma = 2.5$ or softer in the soft state).

Usually found at higher luminosities than the hard state, the lightcurves and spectra of the soft state exhibit less variability than in the hard state (rms variability $\leq 20\%$; Reynolds & Nowak 2003). The radio activity is usually reduced to quiescence (Fender 2002).

1.4.4 The Intermediate State

The intermediate state bears temporal and spectral features very similar to the VHS, but at a significantly lower luminosity. It seems to occur when a transition between the hard and soft state has undergone, but the increase of the accretion rate is not sufficient to enter the soft state (Belloni et al. 1996).

The analysis of the lag in the arrival time of hard photons with respect to soft photons has become a valuable tool to classify transitional states of BH XRBs (Nowak & Vaughan 1996; Nowak et al. 1999). Within the framework of the Comptonization models (section 1.5.1) this time lag was explained as a delay due to scattering in the electron plasma, until it was found that – contrary to former assumptions – the X-ray time lag in the hard state is comparable to the lag in the soft state, whereas the time lag is considerably increased during transitions between the hard and the soft state (Pottschmidt et al. 2000). In fact, an enhanced time lag is better suited to determine an intermediate state than spectral criteria (Pottschmidt et al. 2003; Benlloch 2003; Benlloch et al. 2004).

1.5 Models

The simplest AD model and regular ingredient of most models for BH XRBs has already been mentioned in section 1.3: the α -disk model of Shakura & Sunyaev (1973) features an optically thick, geometrically thin, i.e., relatively cool AD. If the mass accretion rate does not vary in time, the disk is in a “steady state”. Its eponymous viscosity parameter α is usually set at a value ~ 0.1 . Assuming blackbody emission from the surface of the disk with an innermost radius $R_{\text{in}} \approx 3R_{\text{S}}$, the resulting spectrum is given by the surface integral of the blackbody spectra at all different radii, and consequently different temperatures $T(r)$ (Tanaka & Lewin 1995). This multicolor disk model can be satisfactorily fit to the quasi-thermal spectrum of the soft state, but is not applicable to the power-law component which is characteristic to the hard state. For the hard state, workers in this field have developed a number of different models

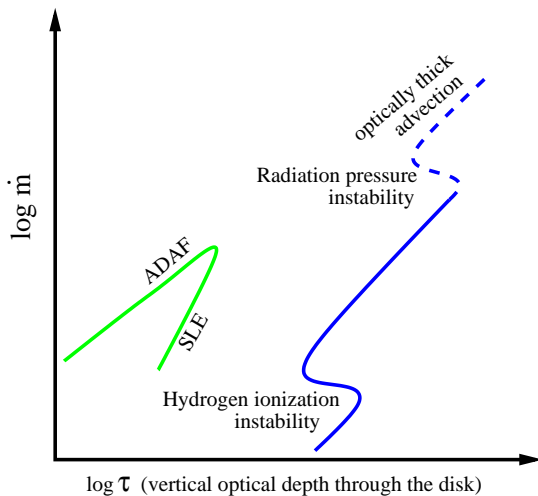


Figure 1.5: Branches of accretion disk solutions as a function of accretion rate \dot{m} and vertical optical depth τ . Apart from the hot solutions of ADAF and the two-temperature disk model (SLE), the right hand line at high τ shows the α -disk model (Done 2002, Fig. 1a).

(for an overview, see Nowak et al. 2002). The most discussed concepts are described in the next sections.

1.5.1 Comptonization Models

The steady cool α -disk model is not the only solution to the hydrodynamic equations describing an AD (see Fig. 1.5). An overview over the most discussed Comptonization models is given, e.g., in Nowak et al. (2002). For low accretion rates, alternatively two hot solution branches with optically thin disks exist (Narayan & Yi 1995).

In the two-temperature disk model, also known as SLE-model after the authors Shapiro, Lightman, and Eardley, $T_e \neq T_{\text{ion}}$ and all of the energy is dissipated into the ions (Shapiro et al. 1976). Although the two-temperature solution is valid for all radii, a hybrid disk was proposed: the inner region of the AD is optically thin, hot and geometrically thick, while the outer region corresponds to the steady α -disk model, optically thick, cold, and geometrically thin. This way, many features needed to explain the high energy spectra of GBHCs are contained: seed photons from the outer cold disk are upscattered in the inner hot corona-like region. A fraction of the coronal radiation is backscattered to the cold disk and reprocessed, giving rise to the reflection features observed in the spectra (cf. 1.4.2). The problem with the SLE-disk is that it is thermally unstable as small perturbations of the electron temperature can

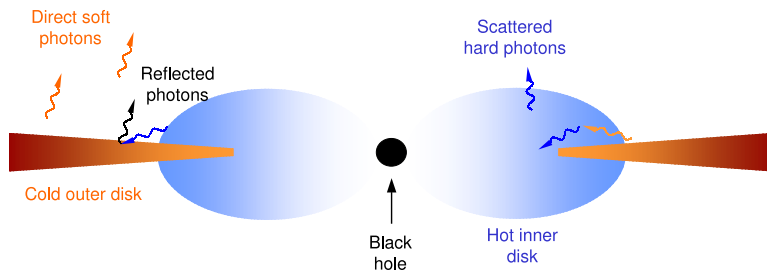


Figure 1.6: Possible geometry for the hard state. The inner edge of the accretion disk is truncated at a fairly large transition radius from the BH, which is inferred from spectral analysis to be of the order of $50\text{--}100 R_S$ for Cyg X-1 (Esin et al. 1997; Done 2002). The inner region near the BH is filled with an expanded rarefied medium responsible for the hard energy photons (Zdziarski et al. 2002, Fig. 15).

cause the corona to collapse or to evaporate (Piran 1978).

The atmospheric Accretion Disk Corona (ADC) model is closely related to the SLE-disk. A hot, optically thin, and geometrically thick ADC sandwiches the cold accretion disk in a slab geometry. The heating of the ADC is realized by reconnection of twisted magnetic flux tubes (di Matteo 1998), a process well-known from our sun. Because of the differential rotation in the accretion disk threaded by a magnetic field, an amplification of local magnetic fields can take place which results in the formation of magnetic flux tubes (Galeev et al. 1979). As these loop-like structures rise above the accretion disk due to magnetic buoyancy, the disk rotation twists the flux tubes. When regions of oppositely directed magnetic fields meet within the disk or between the disk and the corona, they may explosively reconnect, causing significant power to be dissipated via magnetic flares, thus providing a mechanism to heat the corona.

It was shown that a self-sustaining magnetic dynamo process is indeed able to operate (Tout & Pringle 1992). To make this process work, a magneto-rotational instability (MRI; Balbus & Hawley 1991) which enhances the magnetic field and accounts for the transport of angular momentum by producing the turbulence needed for viscosity is utilized. The MRI, developing in weakly magnetized disks, thus bridges the theoretical gap to the ad hoc α -prescription (cf. eq. (1.6)).

The ADC faces several problems that are predominantly connected to the sandwich geometry, i.e., the high covering fraction of the disk by the corona: due to strong re-processing in the disk, which increases the Compton cooling of the ADC, the coronal temperature is low, the equivalent width of iron is large, and a strong soft excess is present, so that this model is not able to explain the hard state spectra of, e.g., Cyg X-1.

To circumvent those shortcomings, a highly ionized transition layer on top of the cold AD was introduced which reduces the reprocessing features by its high reflectivity with respect to coronal photons (Young et al. 2001). However, the physical possibility of such a layer was strongly called into question (Nayakshin & Dove 2001).

A passable way instead seems to be the sphere + disk geometry (Dove et al. 1997). A central spherical corona with radius $R_c \approx 100 R_S$ and coronal temperature $kT_e \approx 90$ keV around the BH is surrounded by a thin disk with $kT_{\text{disk}}(r) = 150 (r/R_c)^{-3/4}$ eV (Dove et al. 1998). On account of the reduced covering fraction, the former problems are avoided. The reflection features can be adjusted by the overlap of disk and corona. Similar geometries have been proposed also by other authors (Fig. 1.6).

In the converging inflow (CI) model, also known as bulk motion Comptonization, Shrader & Titarchuk (1997) propose that the power-law spectrum in the hard and soft state is brought about by a radial flow of matter at high speeds (Laurent & Titarchuk 1999). Close to the event horizon the accreting matter moves in nearly free fall, the so-called converging inflow. The such accelerated electrons with $v \approx c$ possess enough energy in order to upscatter soft disk photons by inverse Compton scattering, and to account for an extended power-law as observed in the soft state spectra, e.g., of Cyg X-1 (cf. Fig. 1.9).

This extended power-law of the soft state without cutoff up to several MeV is in sharp contrast to the power-law of the hard state (see Fig 1.9). As Comptonization in a Maxwellian electron cloud (eq. (1.15)) leads to a power-law with exponential cutoff (Coppi 1999), the applicability of thermal Comptonization to the soft state power-law is questioned and instead a hybrid (=thermal/non-thermal) plasma model is postulated (Gierliński et al. 1999). Inverse Compton scattering with non-thermal electrons, i.e., e^\pm from pair production, bulk motion electrons, and synchrotron electrons, which possess a power-law velocity distribution, leads to a spectral power-law without cutoff, in compliance with the soft state observation.

1.5.2 The ADAF

The advection-dominated accretion flow (ADAF; Narayan & Yi 1995; Narayan et al. 1998) was discovered by Ichimaru (1977) as a second hot solution except the SLE-solution which is thermally unstable (see 1.5.1). Both hot solutions, SLE and ADAF, work only if the mass accretion rate \dot{m} is below a critical value \dot{m}_{crit} . For $\dot{m} > \dot{m}_{\text{crit}}$ neither of the two hot solutions is existent and the only solution available is the cool thin accretion disk (Fig. 1.5).

The two key assumptions of ADAFs are: (1) most of the energy released by viscous dissipation is not radiated immediately, as in a thin disk, but goes into heating the ions, i.e., the protons which are inefficient radiators, (2) the energy transfer from ions to electrons is restricted to Coulomb collisions (Esin et al. 1997). As the density in the thin plasma is so low, Coulomb transfer is inefficient, so that the gas becomes a

two-temperature plasma (Ichimaru 1977). Energy must be transferred from the ions to the electrons before it can be radiated, but that process is slow and the gas reaches the event horizon first, so that the energy is advected with the flow to the BH – hence the name ADAF. As the gas falls into the deep potential well of the compact object, it becomes extraordinarily hot, $T_{\text{ion}} \sim 10^{12}/r$ K, where r is the radius in units of R_S (Narayan & Yi 1995). At such temperatures, the gas bloats up around the compact object in a quasi-spherical cloud of low density gas.

ADAFs are attractive models for explaining the emission of low-luminosity AGN (LLAGN) or underluminous supermassive BHCs such as Sgr A* (see, however, Falcke & Markoff 2000) because most of the energy is carried along with the the gas and is lost into the BH, thus not contributing to radiative emission (Narayan et al. 1995). It has also had significant success in explaining the hard state of XRBs in general, and in particular quiescent states of several soft X-ray transients. In these objects, the transition radius R_{tr} between the outer thin disk and the inner ADAF zone is assumed to be of the order $\approx 10^2 - 10^4 R_S$ (Esin et al. 1997; Liu et al. 1999; Merloni & Fabian 2002). Moreover, the ADAF model has triggered the development of many variants like, e.g., the convection-dominated accretion flow (CDAF; Stone et al. 1999; Narayan et al. 2000), or the advection-dominated inflow-outflow solutions (ADIOS; Blandford & Begelman 1999). The ADIOS model, including outflows from the accreting object, leads over to the jet model described in the next section.

1.5.3 The Jet Model

A basically different approach to explain the hard state X-ray spectrum, challenging the currently favored Comptonization models which ignore any jet contributions, is the concept that synchrotron radiation from a jet dominates the X-ray flux (Falcke & Markoff 2000; Markoff et al. 2001, and references therein). The motivation of this model is drawn from the close analogy of AGN and MQs (see, e.g., Falcke & Biermann 1996).

Fig. 1.7 shows the disk/jet symbiosis model originally designed for quasars (Falcke & Biermann 1995), which in a scaled-down version is applicable also to MQs, assuming a scaling factor $10^6 - 10^9$ corresponding to the respective BH masses. A fraction of the plasma contained in the hot accretion flow is redirected into the jet nozzle, where it is accelerated by some magnetic processes and becomes supersonic. One such acceleration process is diffusive shock acceleration (Marscher & Gear 1985, and references therein) by a shock wave passing through the adiabatic, conical, relativistic jet, triggered by a minor pressure disturbance. Downstream from the nozzle, the plasma flow expands sideways with its initial sound speed. To maintain the energy density of the non-thermal particles producing the broad-band spectrum, repeated and distributed acceleration is assumed (Markoff et al. 2003). The jet power Q_{jet} stems from the mass accretion \dot{m}_{d} in the disk and is assumed to be of the order $Q_{\text{jet}} \sim q_{\text{jet}} \dot{m}_{\text{d}} c^2$,

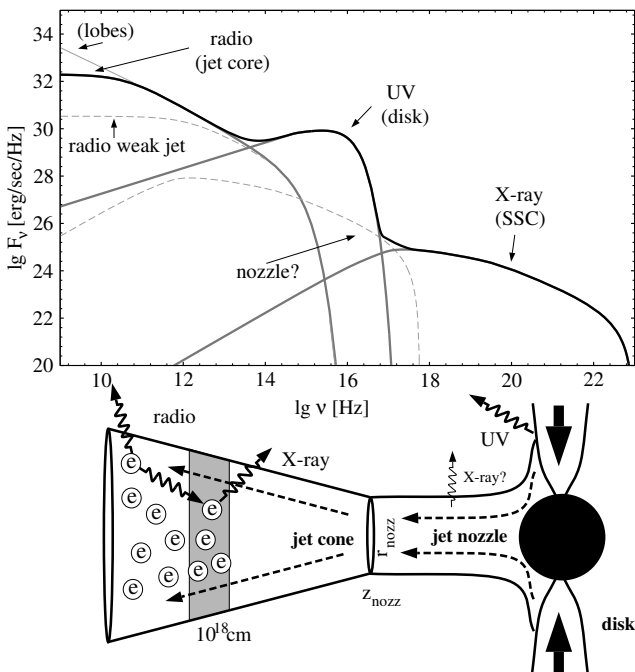


Figure 1.7: The spectrum of a radio loud AGN is shown as a composite of radiative contributions from both disk and jet. SSC is the synchrotron self Compton effect, i.e., the Compton scattering of synchrotron photons by the synchrotron electrons (cf. section 4.1.3). In a down-scaled version, this model is applied to the jets of MQs (Falcke & Biermann 1995, Fig. 5).

with efficiency $q_{\text{jet}} = 10^{-3} - 10^{-1}$ (Meier 2001; Markoff et al. 2003).

The common jet theory assuming that the smallest jet sizes scale linearly with the BH mass (section 4.3.2.2), MQs should emit synchrotron radiation which reaches well into the X-ray regime. By including the spectral properties of an ADAF, this model is able to explain the radio to X-ray broadband spectral data of several GBHCs (Markoff et al. 2001, 2003), contrary to the common exclusively inverse Comptonization models, which fail to address the radio/IR wavelengths. It was noticed that the interpretation of the jet base close to the BH as a hot, magnetized plasma offers the chance to unify the powerful aspects of both jet and Comptonization models, possibly providing a natural explanation for increased time lags in the transitional states (Markoff et al. 2003; Pottschmidt et al. 2003).

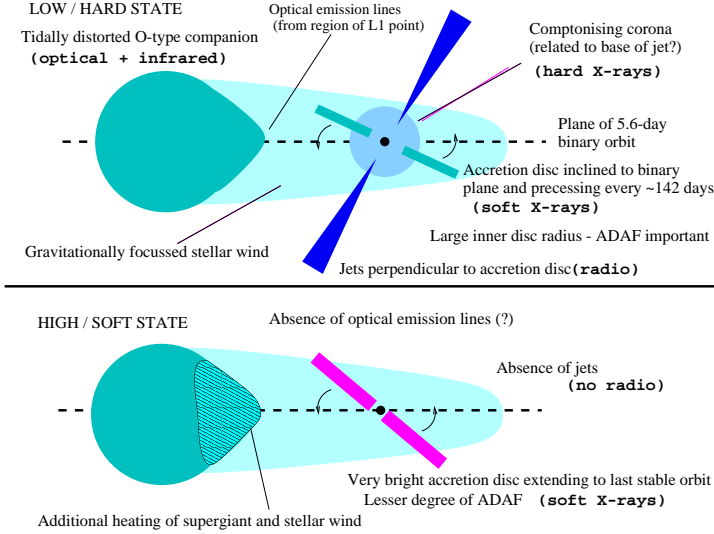


Figure 1.8: Diagram of the binary system of Cyg X-1, depicting the origin of the major spectral components for the hard (upper panel) and the soft state (lower panel) (Brocksopp et al. 1999a, Fig. 7).

1.6 Observing the Prototype: Cygnus X-1

1.6.1 System Parameters

Cyg X-1 was discovered as a bright X-ray source in 1964 (Bowyer et al. 1965), the optical counterpart (V1357 Cyg, HDE 226868) identified at a distance of ~ 2.5 kpc as an O9.7Iab supergiant almost filling its Roche lobe (Bolton 1972; Ninkov et al. 1987, and references therein). Spectral analysis of HDE 226868 leads to a mass determination of $M_{\star} \approx 18M_{\odot}$ (Herrero et al. 1995) and an observed radial velocity of $v \sin i \approx 76 \text{ km s}^{-1}$ (Gies & Bolton 1982). With an orbital period $P = 5.6$ d (Brocksopp et al. 1999b) and an estimated orbital inclination $i \approx 35^{\circ}$ (Herrero et al. 1995), the spectroscopic mass function (eq. (1.3)) $f = 0.252M_{\odot}$ (Gies & Bolton 1982) made it the first established GBHC with $M_{\text{BH}} \approx 10M_{\odot}$.

Because of the certainty of its high mass – even very conservative estimations lie well above the theoretical mass limit of a neutron star – the compact companion of HDE 226868 has been considered as a prototype GBHC, its energy spectrum and variability characteristics serving as a standard to classify various other BHCs. The mass loss rate of HDE 226868 derived from infrared excess is $3.5 \times 10^{-6} M_{\odot} \text{ a}^{-1}$ (Persi et al. 1980), a typical value for OB supergiants which show a strong stellar wind. Of

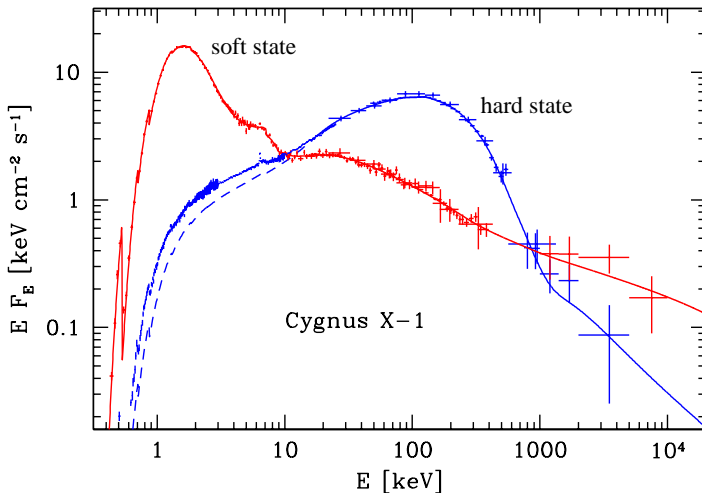


Figure 1.9: Typical spectra of Cyg X-1 in the soft state and in the hard state. The hard power-law seen at energies above ~ 600 keV in the soft state has been attributed to a non-thermal electron component (Gierliński et al. 1999) (modified diagram after McConnell et al. 2002, Fig. 9).

this, about 0.1–1% is accreted onto the BH via focused stellar wind (Friend & Castor 1982), leading to a typical luminosity of 4×10^{37} erg s^{-1} .

The radio, IR, optical, and X-ray flux shows a modulation at the orbital period of 5.6 d and at ~ 150 d (Pooley et al. 1999; Brocksopp et al. 1999a). Sometimes the long term variability is instead attributed a period of ~ 300 d (Priedhorsky et al. 1983). The prevalent explanation for this long term effect is precession or warping of the AD, the perturbing mechanism of which is either the high gravitational potential of the companion responsible for tidal forces on the AD (Larwood 1998), or strong radiative pressure from the center of the X-ray source which changes the structure of the disk and leads to a warped and tilted disk (Petterson 1977).

Cyg X-1 is in $\sim 70\%$ of time found in the hard state, only rarely changing into the soft state. The last transition from the hard into the canonical soft state occurred in 1996, since then the soft state was reached only intermittently. Generally, it shows spectrally flat radio emission at ~ 10 – 20 mJy in the hard state, whereas this emission is quenched during the soft state. Radio flares are seen only rarely.

The spectrum at energies > 2 keV in the hard state is a power-law with a photon-index of $\Gamma \sim 1.4$ – 1.7 , modified by an exponential cutoff with an e-folding energy $E_f \sim 150$ keV (cf. eq. (1.17)). Due to a rather small luminosity difference between

the hard and the soft state (Zhang et al. 1997a) and the presence of a power-law component during the soft state (Gierliński et al. 1999), the soft state of Cyg X-1 is not assumed to be identical to the canonical soft state as seen in other BHCs but rather comparable to the very high state and intermediate state, respectively (Nowak 2003; McClintock & Remillard 2004, and references therein).

The PSD of Cyg X-1 in the hard state shows a characteristic shape. Below a break frequency ν_1 at $\sim 10^{-1}$ Hz, the PSD is flat. At higher frequencies, the PSD follows a f^{-1} course, and at a second break frequency ν_2 at a few Hz, the slope steepens to 2 (Belloni & Hasinger 1990; Nowak et al. 1999). The hard state rms variability (see section 2.2.2) is $\sim 30\%$, while the soft state rms variability is suppressed to a level of only a few percent (Nowak et al. 1999). The break frequency of the PSD seems to be correlated with the total source rms variability (Belloni & Hasinger 1990).

Cyg X-1 is even suspected to be the source of two gamma-ray outbursts observed in 1995 and 2002 (Golenetskii et al. 2002; Schmidt 2002).

1.6.2 Data Acquisition with RXTE

Cyg X-1 has been observed continuously in a long observing program, a so-called monitoring, by the X-ray satellite Rossi X-ray Timing Explorer (*RXTE*). *RXTE* was launched on December 30, 1995 on board a Delta II rocket from Cape Canaveral and deployed in a low earth orbit (altitude 580 km, orbit 96 min, inclination 23°). Originally designed for a mission duration expected to last two to five years, it still fulfills a remarkable workload every day. Besides the All Sky Monitor (*ASM*), *RXTE* carries two co-aligned pointing instruments, the Proportional Counter Array (*PCA*), and the High Energy X-ray Timing Experiment (*HEXTE*), which allow simultaneous observation in the energy range 1–300 keV (Fig. 1.10). The outstanding feature of *RXTE* is the high temporal resolution power of the *PCA* ($1\mu\text{s}$) and the *HEXTE* ($7.6\mu\text{s}$).

The *ASM*, sensitive in the low X-ray energy range between 1.5 keV and 12 keV, daily scans the whole celestial sphere and provides current lightcurves of ~ 350 monitored sources. It consists of three rotating Scanning Shadow Cameras, each containing a position-sensitive proportional counter under a slit mask with a pseudorandom pattern (Levine et al. 1996).

The *PCA*, mainly sensitive to photons in the energy range from ~ 2 keV to ~ 50 keV, consists of 5 co-aligned Proportional Counter Units (*PCUs*; Jahoda et al. 1996) with a large total collecting area of 6250 cm^2 . Pointed observations with a field of view of 1° FWHM are made possible by metal collimators. The *PCUs* are filled with several propane and Xe/methane layers, providing anticoincidence and science information, respectively. Very energetic events above the upper counter discriminator, so-called Very Large Events (VLE), are filtered out as spurious, as they are mostly due to cosmic particles. Nevertheless, the VLE rate is an important input for the calculation of the *PCA* dead time correction. Due to a failure of the propane layer since 2000

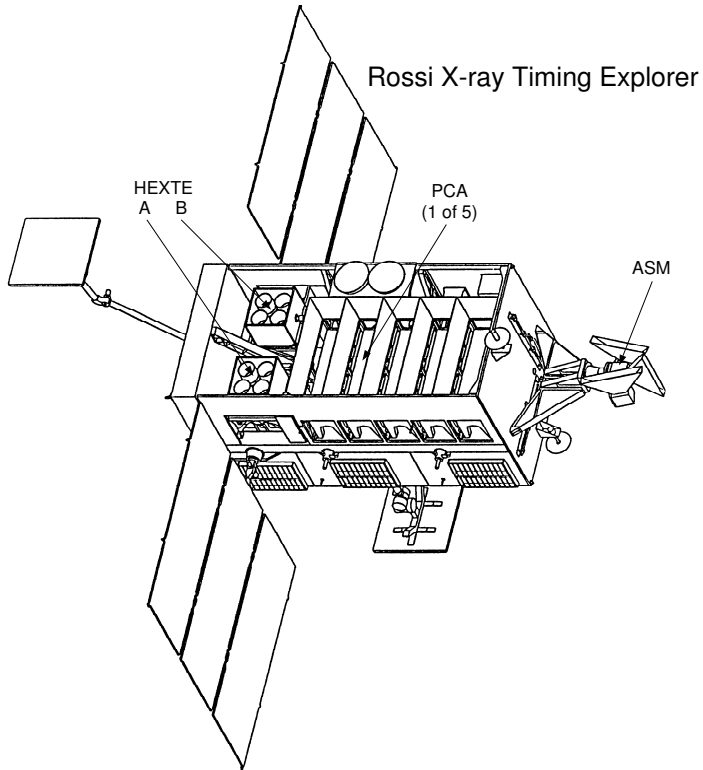


Figure 1.10: Diagram of the Rossi X-ray Timing Explorer (RXTE), with instruments labeled (Rothschild et al. 1998, Fig. 1).

May 12, the measured VLE rate is influenced by a higher event rate in PCU number 0. Since the *PCA* data modes used in this thesis do not contain the PCU number, it is not possible to ignore data from this PCU in the data analysis, and it is not possible to compute a reliable dead time correction.

The high energy range from 15 keV to 250 keV is covered by the detector *HEXTE* which consists of eight NaI(Tl)/CsI(Na) phoswich scintillation counters grouped into two independent clusters, called A and B, with a total collecting area of 1600 cm² (Gruber et al. 1996; Rothschild et al. 1998). Like in the *PCA*, collimators provide a field of view of 1° FWHM.

The data analyzed in this thesis span the time from 1996 until early 2003, covering

Table 1.2: Definition of the energy bands and data modes of the *PCA* high resolution data.

	band 1	band 2	band 3	band 4	band 5
<i>PCA</i> Epoch 3: data taken until 1999 March 22					
P10236 ^a					
channels	0–9	10–15	16–21	22–35	36–189
E [keV]	~2–3.7	3.7–5.8	5.8–8.0	8.0–13.0	13.0–73.5
P10241 ^b					
channels	0–10	11–16	17–22	23–35	36–189
E [keV]	~2–4.1	4.1–6.2	6.2–8.3	8.3–13.0	13.0–73.5
P10257 ^c					
channels	0–13	14–23	24–35	36–249	
E [keV]	~2–5.1	5.1–8.7	8.7–13.0	13.0–100.4	
P10412 ^d					
channels	0–9	10–15	16–21	22–35	36–174
E [keV]	~2–3.7	3.7–5.8	5.8–8.0	8.0–13.0	13.0–67.1
P10512 ^e					
channels	0–9	10–15	16–21	22–35	36–174
E [keV]	~2–3.7	3.7–5.8	5.8–8.0	8.0–13.0	13.0–67.1
P30157 ^f					
channels	0–10	11–16	17–22	23–35	36–49
E [keV]	~2–4.1	4.1–6.2	6.2–8.3	8.3–13.0	13.0–18.1
P40099-01 to P40099-05 ^g					
channels	0–10	11–16	17–22	23–35	36–189
E [keV]	~2–4.1	4.1–6.2	6.2–8.3	8.3–13.0	13.0–73.5
<i>PCA</i> Epoch 4: data taken after 1999 March 22					
P40099-06 to P40099-28, P50110, P60090, P70414 ^h					
channels	0–10	11–13	14–19	20–30	36–159
E [keV]	~2–4.6	4.6–5.9	5.9–8.4	8.4–13.1	15.2–71.8

^a data modes B_4ms_8A_0_35_H and E_62us_32M_36_1s

^b data modes B_2ms_8B_0_35_Q and E_125us_64M_36_1s

^c data mode E_4us_4B_0_1s

^d data modes B_4ms_8A_0_35_H and E_62us_32M_36_1s

^e data modes B_4ms_8A_0_35_H and E_16us_16B_36_1s

^f data mode B_16ms_46M_0_49_H

^g data modes B_2ms_8B_0_35_Q and E_125us_64M_36_1s

^h data modes B_2ms_8B_0_35_Q and E_125us_64M_36_1s

the *RXTE* monitoring programs since Announcement of Opportunity 3 (AO3, 1998) through AO6 (2002/2003). Typical exposure times were 3 ks on a weekly schedule in 1998, and 10 ks observations performed every two weeks since then.

After screening the data for episodes of increased background, we extracted *Stan-*

dard2f lightcurves with a resolution of 16 s from the *PCA* data using the standard *RXTE* data analysis software, *HEASOFT*. From the same detector, also high resolution data with a resolution of 2^{-6} s (~ 16 ms; AO3) or 2^{-8} s (~ 4 ms; other data) were obtained, processed as lightcurves in 5 different energy bands (Table 1.2). Also high energy data from the *HEXTE* with a time resolution of 1 s were extracted. A detailed description of the data extraction issues is given by Pottschmidt (2002) and Pottschmidt et al. (2003).

1.6.3 Radio Observations with the Ryle Telescope

Besides X-ray data from *RXTE*, simultaneous radio data from the Ryle Telescope at the Mullard Radio Astronomy Observatory at Cambridge (UK) are used in this thesis, which allows to look for correlations among the different wavelength regimes (see section 5).

The basic parameters of the radio telescope are described by Jones (1991). It consists of a total of 8 equatorially mounted 13 m-Cassegrain antennas on an E-W baseline, with 4 moveable aerials on a 1.2 km rail track, and 4 stationary aerials fixed at 1.2 km intervals.

The radio data were taken at 15.2 GHz ($\lambda \approx 2$ cm), with a bandwidth of 350 MHz (Pooley & Fender 1997). The resulting lightcurves have a time resolution of 8 s, and every ~ 30 min there is a data gap of ~ 3.5 min in the radio lightcurves due to calibration (section 4.1.1). The radio flux of Cygnus X-1 at this frequency is in the range of 10–20 mJy when the source is in the hard state, while it is undetectable in the soft state.

Part I

X-ray Variability

CHAPTER 2

Variability of BH XRBs

“The noise is the signal.”

Rolf Landauer (1927–1999)

2.1 Introduction

Variability is one of the characteristics of nature, and some variability patterns are in fact rather common: the flux from quasars, the water level of rivers, or the stock exchange price indices all show a characteristic behavior, the so-called flicker noise (Bak et al. 1988). Analysis of the variability parameters, e.g., the time scales on which these variations take place, allows a deeper understanding of these systems and provides information that is not present in the time-averaged signal (Beenakker & Schönberger 2003). In the case of BH XRBs short-time variability of X-ray emission is considered especially interesting since it could provide better insight into the physical processes at work near the black hole.

One of the basic tools to do these analyses is supplied by the Fourier techniques. To receive unaltered results it has to be made sure that the derived parameters are decoupled from any biasing processes like, e.g., counting noise, or detector dead time. There have been numerous attempts to explain the origin of variability by various models. In the past the focus was set on shot noise theories. The continuously developing capabilities of the observatories have broadened the horizon to a wider range of sources, adding new interesting alternative explanations.

2.2 Measuring Variability

2.2.1 Fourier Analysis

Fourier techniques are of widespread use in many fields of science. The following description adopts the conditions in X-ray astronomy and is based on van der Klis

(1989). To determine the variability, also called flickering, of a lightcurve the count rate $x(t_k) =: x_k$ is determined for a series of n time intervals t_k ($k = 0, \dots, n-1$) with duration Δt . Then the discrete Fourier transform which decomposes the lightcurve into n sine curves is defined by

$$X_j = \sum_{k=0}^{n-1} x_k \exp(2\pi i j k / n) \quad (2.1)$$

where $j = -\frac{n}{2}, \dots, \frac{n}{2} - 1$ and $i = \sqrt{-1}$, the imaginary unit. The relation between the zeroth coefficient X_0 and the total number of observed photons N_{ph} becomes clear when transforming

$$X_0 = \sum_{k=0}^{n-1} x_k = \frac{1}{\Delta t} \sum_{k=0}^{n-1} x_k \Delta t = \frac{N_{\text{ph}}}{\Delta t} = n \langle x \rangle \quad (2.2)$$

with $\langle x \rangle$ the mean count rate of all time bins.

The discrete Fourier coefficients X_j are calculated for the independent frequencies, the so-called Fourier frequencies

$$f_j = \frac{j}{T} = \frac{j}{n\Delta t} \quad (2.3)$$

where $T = n\Delta t$ is the length of the lightcurve. In practice the negative values of j are disregarded and the usable frequency range is between $f_{\text{min}} = 1/T$ for $j_{\text{min}} = 1$ and $f_{\text{max}} = 1/2\Delta t$, the Nyquist frequency, for $j_{\text{max}} = n/2$.

2.2.2 Power Spectral Density

With the result of eq. (2.1) the corresponding periodogram is defined as the squared absolute value of the Fourier coefficients

$$P_j = A |X_j|^2 \quad (2.4)$$

where $j \in [0, \dots, n/2]$ and the normalization constant A is introduced. When dealing with a continuous set of values, the mathematically correct term would be power spectral density (PSD) instead of periodogram. In X-ray astronomy both terms are used in parallel regardless of the discrete or continuous nature.

The most common normalizations of the PSD are the Leahy et al. (1983) normalization with

$$A_{\text{Leahy}} = 2\Delta t^2 / N_{\text{ph}} = 2\Delta t / X_0 \quad (2.5)$$

and the Miyamoto et al. (1992) normalization with

$$A_{\text{Miyamoto}} = 2\Delta t^2 / (N_{\text{ph}} \langle x \rangle) = A_{\text{Leahy}} / \langle x \rangle. \quad (2.6)$$

As van der Klis (1995) put it, the PSD “. . . is a measure of the variance of the time series around its mean. The strength of the QPO and noise components as measured from power spectra is usually expressed in terms of fractional root-mean-square (rms) amplitude . . . It can be thought of as some kind of mean amplitude of the intensity variations, expressed as a fraction of the average intensity.”

This rms amplitude or rms variability, σ , in short referred to simply as “rms”, is defined for a set of n values x_k with mean $\langle x \rangle$ as (van der Klis 1989)

$$\sigma \equiv \sqrt{\frac{1}{n} \sum_{k=0}^{n-1} (x_k - \langle x \rangle)^2} \quad (2.7)$$

Normalizing σ to the mean $\langle x \rangle$ gives the dimensionless fractional rms variability. The advantage of the Miyamoto normalization (eq. (2.6)) is that integrating the PSD over positive Fourier frequencies and then taking the square root yields the fractional rms variability (Nowak et al. 1999). Thus, in Miyamoto normalization the PSD is usually given in units of squared fractional rms per frequency interval, $(\text{rms}/\langle x \rangle)^2/\text{Hz}$ (cf. Fig. 2.1).

2.2.3 Noise and Dead Time

Due to the random character of the spontaneous emission of photons, incoming radiation is subject to Poisson statistics, where the standard deviation, σ_{SD} , of the count rate is related to the mean $\langle x \rangle$ as

$$\sigma_{\text{SD}} = \sqrt{\langle x \rangle}. \quad (2.8)$$

Thus the relative contribution of Poisson noise, also known as counting noise, to the signal decreases with count rate. In the Leahy normalization of the PSD (eq. (2.5)), the Poisson noise level amounts to a value of 2, independently of the count rate. This relation is very useful in order to subtract Poisson noise from the PSD.

Apart from the intrinsic Poisson noise, the observed noise level is also influenced by the dead time of the radiation detectors. In the case of the *PCA* onboard *RXTE* (section 1.6.2), dead time is of the order of 10–100 μs depending on the energy of the triggering event. The procedure how to account for *PCA* dead time when calculating the PSD has been thoroughly studied (Zhang et al. 1995; Jernigan et al. 2000; Pottschmidt 2002).

2.3 Variability Patterns and Variability Models

With the time resolution of satellite X-ray detectors entering the ms and μs regime, it became clear that the irregular X-ray variability of BH XRB seen on longer time

scales is continued also on the smallest time scales. While the assumption of the X-ray variability on small time scales being a fingerprint of black holes had to be given up, workers in this field have never ceased to propose new explanations for X-ray variability. Two of the models presented in this section will be discussed further in chapter 3.

For the characterization of the overall shape of a PSD, a set of terms is used which were coined in analogy to light (Harris & Ledwidge 1974). A signal with no correlation in time will give a “white noise” PSD whose powers are constant over all the frequency range. On the other hand, the “red noise” PSD as a function of the frequency f decreases with increasing frequency. A special case of red noise is represented by the omnipresent flicker noise, also called “ $1/f$ noise”: the PSD behaves like $P(f) = 1/f^A$, where the exponent A is very close to 1.

The hard state PSD of Cygnus X-1 can be thought to consist of three separate frequency segments with a variability pattern of its own (see Fig. 2.1). Below a break at 0.04–0.4 Hz, the PSD is flat, the mid segment up to a break at 1–6 Hz approximately $\propto f^{-1}$, and approximately $\propto f^{-2}$ at higher frequencies (Belloni & Hasinger 1990; Nowak et al. 1999).

It has been shown that the presence of $1/f$ fluctuations in BH XRBs and also AGN is compatible with a cellular automaton process (Mineshige et al. 1994a; Zurita et al. 2003), which acts on the assumption of an array of cells with discrete state variables. The values of the variables of each cell, i.e., its state, are updated at every time step by a small set of rules which define the new state of the cell based on its current state and on the current states of neighboring cells. A cellular automaton process is capable of producing a range of behaviors with complex spatial and temporal patterns, e.g., a $1/f$ noise, from very simple rules (Wolfram 1986). This concept of individual cells producing a large-scale temporal pattern has been taken up by some of the following models, e.g., the shot noise models, or the process of magnetic reconnection.

2.3.1 Shot Noise Models

The term shot noise, suggesting an analogy to the pellets of lead loaded in a cartridge, was introduced by Walter Schottky who analyzed the causes of time-dependent current fluctuations of a vacuum tube. Noise comes from the thermal motion of the electrons, the thermal noise, and from the irregular arrival of electrons at the anode. This second effect, the shot noise, is due to the discrete nature of electrons which are randomly and independently emitted by the cathode in a Poisson process (Beenakker & Schönberger 2003).

Shot noise models, where the lightcurve is thought of as a superposition of individual events, have been used as a phenomenological model to explain the aperiodic variability of XRBs (Tanaka & Lewin 1995). In a mathematical description following Pottschmidt et al. (1998), a shot noise time series $I(t)$ is given as the sum over all

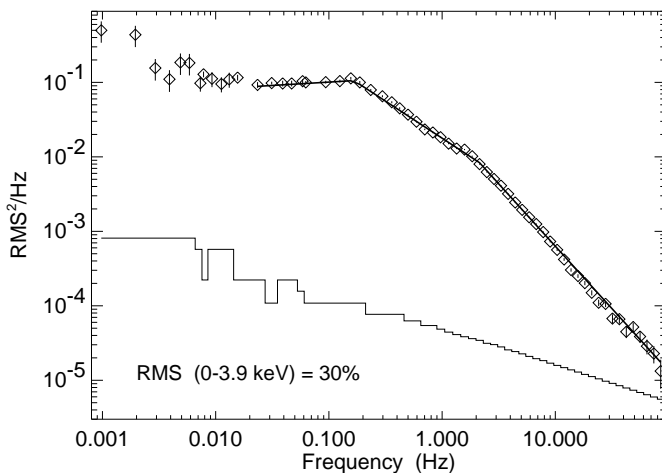


Figure 2.1: Noise-subtracted hard state PSD of Cyg X-1 in Miyamoto et al. (1992) normalization for the energy band 0–3.9 keV. The solid line represents the “effective noise” level, which is essentially the minimum level of variability that could have been detected with this observation (Nowak et al. 1999, Fig. 2a).

events $F(t)$ that have taken place at times t_i

$$I(t) = \sum_i F(t - t_i) \quad (2.9)$$

The profile of $F(t)$ can take various shapes, for example an instantaneous rising and exponentially decaying shot with decay time τ

$$F(t) = U(t)e^{-t/\tau} \quad (2.10)$$

where $U(t)$ is constant for $t \geq 0$, and zero otherwise. Then the theoretical power spectrum of the shot noise process is given as (Lehto 1989)

$$P_{\text{SN}}(f) \propto \frac{\lambda}{(1/\tau)^2 + (2\pi f)^2} \quad (2.11)$$

where λ is the mean event rate. To account for all observed features of the PSD, a multitude of profiles with different shapes and durations lasting from milliseconds to a few seconds has been studied (Terrell 1972; Lochner et al. 1991).

The big drawback of the theoretical description of variability by the shot noise model is that many parameters, especially a variety of different relaxation time scales, are needed for a satisfactory modeling of observed PSDs. An improved approach using a linear space state model (LSSM) provides a good description of the lightcurve variability of accreting compact objects as an auto-regressive process of first order (König et al. 1997). In the case of Cyg X-1 it was possible to reduce the intrinsic variability to a single relaxation time scale $\tau = 0.19 \pm 0.03$ s, leading to the interpretation of the system variability as stochastic superposition of individual shot events with a single relaxation time (Pottschmidt et al. 1998).

2.3.2 Quasi-Periodic Oscillations

Both BHCs and low-magnetic field neutron stars in accreting binary systems may exhibit well defined peaks in the PSD, the so-called quasi-periodic oscillations (QPOs) (Fig. 2.2). They are specified by a quality factor

$$Q_i = \frac{f_i}{\Delta f_{\text{FWHM}}} \quad (2.12)$$

where f_i is the central, i.e., resonance frequency, and Δf_{FWHM} is the full frequency width of the QPO profile at the half maximum value. QPOs are usually modeled by a Gaussian or a Lorentzian profile, the latter in the literature usually given by

$$L_i(f) = \pi^{-1} \frac{2R_i^2 Q_i f_i}{f_i^2 + 4Q_i^2 (f - f_i)^2} \quad (2.13)$$

where R_i is a normalization constant (Nowak 2000; Pottschmidt et al. 2003). Broader QPO features as seen in BHCs are also referred to as peaked noise components (van der Klis 1995).

The manifestations of QPOs are complex, and workers in this field faced with a variety of specialties. In spite of that, four distinct classes of QPOs can be distinguished in accreting neutron stars with a low magnetic field (Psaltis & Norman 2000): in the frequency range below 100 Hz the normal branch oscillations and the horizontal branch oscillations (HBO) are present, while in the range $\sim 200 - 1300$ Hz the twin phenomenon of the lower and upper kHz QPOs with centroid frequencies f_1 and f_2 , respectively, has been detected (see review by van der Klis 2000). QPOs in BHCs are less established because only few observable sources are known. However, the QPOs in BHCs and neutron stars seem to follow similar tight correlations (Psaltis et al. 1999; Wijnands & van der Klis 1999).

The analogy of the QPO phenomenon in BHCs and neutron stars has favored interpretations which work under assumptions that are common to both systems. Among the most straightforward parameters one would think of are the accretion mass rate,

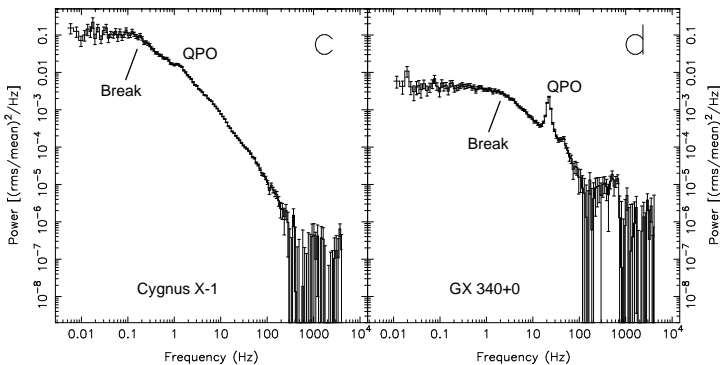


Figure 2.2: PSDs of the BHC Cyg X-1 (left) and the neutron star GX 340+0 (right) at low accretion rates: below a break frequency, f_{break} , the band-limited noise component approximately following a $1/f$ dependence turns into a flat spectrum. Superimposed on this broad-band noise is a bump-like feature, a so-called QPO. The dead time-modified Poisson level has been subtracted from the PSD values (Wijnands & van der Klis 1999, Fig. 1).

\dot{m} , or the inner disk radius, r_{in} . The correlation of QPO frequencies with flux, which according to energy conservation is expected to be proportional to \dot{m} , is not satisfactory, though (van der Klis 1995). On the other hand, beat frequency models which associate QPOs with the Keplerian frequency at r_{in} and the spin frequency of the neutron star are not applicable to BHCs (Alpar & Shaham 1985; Miller et al. 1998). Nevertheless, the variability expressed by the QPOs should be somehow connected to the irregular nature of the accretion flow, particularly the kHz QPOs serving as a probe of the innermost regions near the accretor where strong-field gravitational effects are manifest (van der Klis 1995).

The relativistic precession model assumes that the motion of matter in the AD is governed only by the gravitational potential of the central object (Stella & Vietri 1998, 1999), which facilitates its applicability to both BHCs and neutron stars. QPOs arise from the fundamental frequencies of the motion of blobs near the compact object. While the Keplerian motion of inhomogeneities in the innermost disk regions gives rise to the higher frequency kHz QPOs at f_2 , the lower frequency kHz QPOs at f_1 are excited by the relativistic periastron precession of eccentric orbits, and the HBOs by the nodal precession of tilted orbits due to the Lense-Thirring effect in the same regions (Marković & Lamb 1998).

This model is able to incorporate similar approaches: Psaltis & Norman (2000) showed that a change of the disk properties at a transitional radius separating, e.g., the outer thin disk and the inner ADAF, acts as a low band-pass filter giving response

only to certain frequencies dominating the inner disk. This is similar to the concept of normal modes of acoustic oscillations within the inner region of the accretion disk (Nowak & Wagoner 1991).

2.3.3 Magnetic Reconnection

One most likely explanation for variability, e.g., flares, are local magnetic reconnection events in or above the accretion disk. A dynamo mechanism driven by the strong shear due to differential rotation in the accretion disk is thought to generate magnetic fields (Tout & Pringle 1992). When magnetic loops of opposite direction reconnect, energy is released in single, shot-like events (see section 1.5.1). The superposition of all reconnection events may be causing the variability of radiation from accreting BHCs.

The shot-like character of the recombination events establishes a close relation to the shot noise model discussed in section 2.3.1. The mechanism of magnetic reconnection has also been used for a model which will be outlined in the next section.

2.3.4 The Thundercloud Model

Named after its similarity to the properties of terrestrial lightning, the thundercloud model proposes that magnetic field reconnection of flux tubes takes place in the corona above the AD in a spatially and temporally correlated manner (Merloni & Fabian 2001). Referring to the stochastic pulse-avalanche model of Poutanen & Fabian (1999) which assumes that hard X-rays are mainly produced by Comptonization of disk seed photons in magnetic flares in the ADC, each flare has a certain probability to ignite a neighboring flare, sometimes giving rise to long correlated trains of events. The distribution of duration and size of the avalanches determines the PSD of the resulting X-ray emission. The advantage of this model is that it not only accounts for the temporal features of accreting BHs but at the same time is able to explain the spectral variability.

2.3.5 The Propagation Model

The disk propagation model (Lyubarskii 1997) tries explain the $1/f^{1...2}$ flicker noise of XRBs by fluctuations of the viscosity parameter α of Shakura & Sunyaev (1973). These fluctuations of α might be invoked by varying magnetic stresses due to magnetohydrodynamic turbulence (Balbus & Hawley 1991). Incoherent, i.e., statistically uncorrelated variations of α at different radii r and, according to (Churazov et al. 2001)

$$\tau_{\text{visc}} \sim \left(\alpha \left(\frac{H}{r} \right)^2 \Omega_K \right)^{-1} \quad (2.14)$$

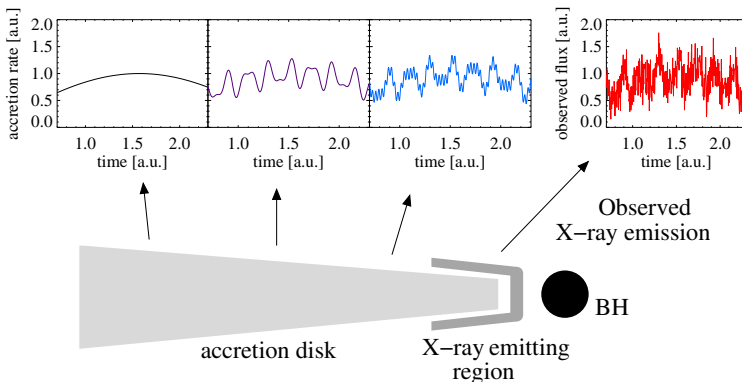


Figure 2.3: The propagation model assumes that the mass accretion rate, \dot{m} , is modulated at different time scales depending on the radius from the BH. As the main X-ray emission stems from the innermost disk regions, the observed X-ray flux is a superposition of all variations of \dot{m} that propagated from the outer disk to the inner region. (Diagram based on a figure by Uttley et al. (2003).)

at corresponding different local viscous time scales τ_{visc} result in varying accretion rates at these radii. As these variations of \dot{m} propagate down to the inner zone of the disk, the variations introduced at large radii, i.e., at long time scales, modulate all variations at small radii, i.e., at short time scales. Finally, near the inner radius of the disk where most of the X-ray radiation is set free, the released luminosity is a representation of a sum of independent variations produced at different radii, and correspondingly different time scales. The observed X-ray flux from the inner zone of the AD is of the flicker noise type, provided the time scale of the α perturbations is comparable to or shorter than the time scale of propagation from the outer to the inner disk region.

The observed time lags of hard photons with respect to soft photons (Pottschmidt et al. 2000) and even the logarithmic energy dependence of the lags (Miyamoto & Kitamoto 1989; Nowak et al. 1999) can be explained by this fluctuation model (Kotov et al. 2001).

However in geometrically thin disks the chance of accretion rate fluctuations to propagate down to the X-ray releasing inner AD region is small due to the diffusive nature of such disks (Churazov et al. 2001). Much better conditions for the propagation of accretion rate fluctuations on all time scales are present in geometrically thick disks, like AD coronae or ADAFs.

2.3.6 The rms-Flux Relation

Uttley & McHardy (2001) found a remarkable linear relationship between the rms amplitude of broadband noise variability and flux in the X-ray lightcurves of neutron star and BH X-ray binaries, and AGN. This linear relation between flux and rms variability has an offset on the flux axis, leading to the suggestion that the light curves of X-ray binaries are made from at least two components: one component with a linear dependence of rms variability on flux, and one component which contributes a constant rms to the lightcurve or does not vary at all. The fact that the same rms-flux relation was found in the lightcurves of active galactic nuclei suggests that this behavior is intrinsic to compact accreting systems.

In the case of X-ray binaries, the rms-flux relation has until now only been investigated for single observations of SAX J1808.4–3658 and for a few hard state observations of Cyg X-1. It is important to discover whether this relation applies generally for many observations of a given object and across a range of states. Therefore in the next chapter the evolution and behavior of the rms-flux relation in Cyg X-1 using the *RXTE* monitoring data is investigated.

The rms-Flux Relation in Cygnus X-1

In this chapter the linear relationship between the rms variability and the flux, the so-called rms-flux relation, is analyzed. Since the following sections are based on a paper (Gleissner et al. 2004c), they retain the characteristic publication style.

3.1 Observations and Data Analysis

3.1.1 Data Extraction

The data analyzed here span the time from 1996 until early 2003, covering our *RXTE* monitoring programs since *RXTE* Announcement of Opportunity 3 (AO3, 1998) through *RXTE*'s AO6 (2002/2003). Additionally, other public *RXTE* data from *RXTE* AO1 and AO7 were used. The high temporal resolution data from the *PCA* in 5 different energy bands, as described in section 1.6.2, were extracted, using the analysis software, *HEASOFT*, Version 5.0. Due to integer overflows in the binned data modes, high soft X-ray count rates can lead to a distortion of the rms-flux relation for the lowest energy band (see section 3.1.4 for further discussion). We therefore use only data from energy bands 2–5 which are not affected. As the total number of operational proportional counter units (*PCUs*) was often not constant during an observation, separate lightcurves were generated for each of the different *PCU* combinations. These lightcurves were analyzed separately. To facilitate comparisons, unless noted otherwise we normalize all data to one *PCU*.

Table 1.2 shows that the energy limits of the high-resolution lightcurves, which were used for the computation of the rms-flux relation, in parts differ significantly. In order to enable comparisons, we normalize all observations to the energy limits of epoch 4 (P40099-06/28, P50110, P60090, P70414). We calculate a flux correction factor to the epoch 3 observations by integrating the count rates of the corresponding spectrum channels of each observation. This factor has to be applied also to all values that are dependent on flux, e.g. C , σ , etc.

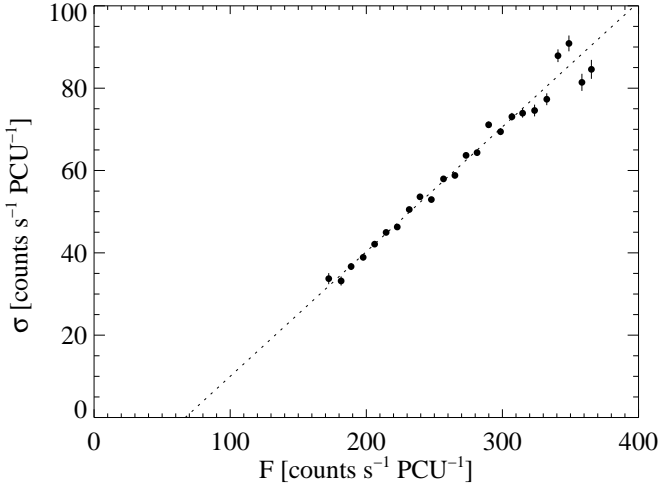


Figure 3.1: Relation between the *PCA* count rate, F , and the rms variability, σ , for the observation of 1998 July 02, showing the typical hard state characteristics. The data are extracted from energy band 2 (4.1–6.2 keV). The dotted line is the best-fitting linear model to the data (see text), the error bars are at the 1σ level.

3.1.2 Computation of the rms Variability

To determine the rms variability as a function of source flux, we first cut the observed lightcurve into segments of 1 s duration for which the source count rate is determined. These segments are then assigned to their respective flux bins. In general, 40 linearly spaced flux bins were chosen. In the final computation, only flux bins containing at least 20 segments were retained. We note that short time segments of 1 s duration are necessary to study the characteristic variability of the source which is dominated by frequencies above 10^{-1} Hz. Thus using a 1 s segment size allows us to measure rms-flux relations which sample a broad range of fluxes, while also measuring rms with high signal-to-noise, since the minimum frequency of variability sampled within each segment is well below the frequency where photon counting noise dominates.

Next for each of the lightcurve segments in each of the flux bins, the rms variability is determined for the Fourier frequency interval of interest. We first compute the PSDs of the individual lightcurve segments (Nowak et al. 1999; Nowak 2000), using the PSD normalization where the integrated PSD equals the squared fractional rms variability (i.e., the fractional variance) of the lightcurve (Belloni & Hasinger 1990;

Miyamoto et al. 1992). We then average all the PSDs obtained for segments in the same flux bin, and bin the averaged PSD over the frequency range from 1 Hz to 32 Hz to yield the average power density in that frequency range, $\langle P \rangle$. Then, the absolute rms variability of the source in the frequency band of interest, σ , is obtained according to

$$\sigma = [(\langle P \rangle - c_{\text{Poisson}}) \cdot \Delta f]^{1/2} F \quad (3.1)$$

where c_{Poisson} is the Poisson noise level due to photon counting statistics, Δf is the width of the frequency band of interest, and where F is the source count rate of the flux bin (normalized to one PCU). Note that in the comparatively low frequency range considered here, the detector dead time does not need to be taken into account when determining the Poisson noise level. The statistical uncertainty of the average PSD value, $\Delta \langle P \rangle$, is determined from the periodogram statistics (van der Klis 1989)

$$\Delta \langle P \rangle = \frac{\langle P \rangle}{\sqrt{MW}} \quad (3.2)$$

where M is the number of segments used in determining the average rms-value and W is the number of Fourier frequencies in the frequency range of interest. The uncertainty of σ , $\Delta(\sigma)$, is then computed using the standard error propagation formulae. Note that, since we measure σ from the average PSD in each flux bin, our method differs from that of Uttley & McHardy (2001), who first calculated a Poisson noise-subtracted rms for each individual segment before binning up to obtain σ in each flux bin. Uttley & McHardy (2001) computed the uncertainty of σ by calculating standard uncertainties from the scatter of the rms values in each flux bin. This method has the disadvantage that, when the variance due to the source is small compared to the variance due to Poisson noise, subtracting the expected Poisson noise level can sometimes lead to negative variances due to the intrinsic variations in the realized noise level. Our revised method avoids this problem by averaging the segment PSDs before noise is subtracted, thus reducing the intrinsic variations in the noise level.

3.1.3 rms versus Flux

Fig. 3.1 shows the rms versus flux relationship for a typical hard state observation, taken on 1998 July 02, in energy band 2 (4.1–6.2 keV). To describe this linear relationship, we model it with a function of the form (Uttley & McHardy 2001)

$$\sigma = k(F - C) \quad (3.3)$$

where the slope, k , and intercept, C , are the fit parameters. This linear model fits the general shape of the rms-flux relation of the example reasonably well, although the large χ^2 value of 102.1 for 22 degrees of freedom implies that there is some weak

intrinsic scatter. The best-fitting model parameters for the example of Fig. 3.1 are $k = 0.30 \pm 0.01$ and $C = 67 \pm 5 \text{ counts s}^{-1} \text{ PCU}^{-1}$ (unless otherwise noted, uncertainties are at the 90% confidence level for two interesting parameters).

In order to interpret the parameters of eq. (3.3) it is useful to use a toy model in which the observed source flux, $F_{\text{obs}}(t)$, is written as the sum of two components,

$$F_{\text{obs}}(t) = F_{\text{const}} + F_{\text{var}}(t) \quad (3.4)$$

where F_{const} is a component of the lightcurve which is assumed to be non-varying on the time scales considered here, and where $F_{\text{var}}(t)$ is a component which is variable and thus responsible for the observed rms variability. In the toy model of eq. (3.4) the interpretation of the slope k of the rms-flux relationship is straightforward: it is the fractional rms of $F_{\text{var}}(t)$. Furthermore, the intercept of the rms-flux relation on the flux axis, C , is the count rate of F_{const} . It is obtained by extrapolating $F_{\text{var}} \rightarrow 0$ in eq. (3.4).

While the decomposition of eq. (3.4) is the most straightforward, it is not fully unique. As we will show later, for the majority of our observations $C > 0$, however, there are several observations in which $C < 0$. In these cases the above interpretation clearly breaks down (there are no negative fluxes) and it makes more sense to write eq. (3.3) as

$$\sigma = kF + \sigma_0 \quad (3.5)$$

In this formulation of the rms-flux relationship we have introduced σ_0 , an excess rms present in the lightcurve, which is positive whenever $C < 0$. Note that for $\sigma_0 > 0$ eq. (3.5) predicts $\sigma \rightarrow \sigma_0$ for $F \rightarrow 0$, i.e., the extrapolation of the rms-flux relationship to flux zero predicts that there is still variability present, which is clearly unphysical. We do not consider this behavior a problem, however, as the rms-flux relationship is measured only for $F \gg 0$. We deem it reasonable to assume that for $F \approx 0$ other variability processes which do not obey the linear rms-flux relationship will become important and force $\sigma \rightarrow 0$ for $F \rightarrow 0$. Finally, we note that for $\sigma_0 < 0$ the observed rms is reduced with respect to a linear rms-flux relationship with $\sigma_0 = 0$. This is possible, e.g., if a constant flux component, F_{const} , is present in the lightcurve (the majority of our fits imply reductions of about 25% in rms with respect to $\sigma_0 = 0$).

Observationally, degeneracies in the fit prevent us from distinguishing between the two interpretations of the rms-flux relationship. Since most of the observations of Cyg X-1 presented in the following have $C > 0$, and to enable the comparison with other analyses, we have chosen to use eq. (3.3) as our fit function. We ask the reader, however, to keep the second interpretation of the rms-flux relationship in mind.

The best test of linearity is a χ^2 test of whether a straight line fits the data. On the other hand, it is usually very difficult to fit a simple model to variability properties because of the scatter in the data points. It may be misleading to discard an observation

as being ‘non-linear’ just because a straight line does not supply a good χ^2 fit. We found that Kendall’s rank correlation coefficient, which tests whether a correlation is monotonic, serves as a good indicator of linearity in the sense that the bulk of points follows a straight trend, while allowing for some points, predominantly at high fluxes (cf. Fig. 3.1), to diverge.

Therefore we choose to characterize the goodness of the linear correlation between N data points of σ and F using Kendall’s rank correlation coefficient, τ , defined by

$$\tau = \frac{S}{N(N-1)/2} \quad (3.6)$$

Here S is the sum of scores which are determined if to each of the $N(N-1)/2$ possible pairs $[(\sigma_i/F_i), (\sigma_j/F_j)]$ of the sample $(\sigma_1/F_1), \dots, (\sigma_N/F_N)$ a score of $+1$ or -1 is assigned, depending on whether their ranks are in the same order or in the opposite order on the σ and F axes, respectively (Keeping 1962).

The correlation in Fig. 3.1, e.g., has $\tau = 0.95$ (the range of the correlation coefficient is $-1 \leq \tau \leq 1$, with a perfect correlation being indicated by $\tau = 1$). For the remainder of this chapter we set a minimum threshold of $\tau_{\min} = 0.9$ below which we do not accept the hypothesis of a linear rms-flux relationship. Given this criterion, the fit with this simple linear function works for the majority of all observations (201 out of 220). With a few exceptions, the rejected observations with $\tau < \tau_{\min}$ generally have short exposure times and therefore bad counting statistics, resulting in a scattered rms-flux relation. In the following discussions of the behavior of k and C we will not include these observations (but see section 3.2.2).

Even though the χ^2 fits for linearity are not always so good, the maximum deviations from the best fit straight line are generally less than 15%. We therefore think that it is acceptable to test linearity by τ and use the fit parameters k and C for correlations with other variables, although these correlations may contain some approximate only data points due to fitting a model which does not exactly describe the data.

3.1.4 Buffer Overflows in RXTE Binned Data Modes

Due to integer overflows in the binned data modes, high soft X-ray count rates can lead to a distortion of the rms-flux relation for the lowest energy band. During phases of high soft X-ray flux, the rms-flux relation for energy band 1 (~ 2 – 4.6 keV) shows a clear deviation from its typical linear behavior. These phases are characterized by a smaller rms than what would be expected when extrapolating the rms-flux relation measured for smaller fluxes (Fig. 3.4). We initially associated this breakdown of the relationship with changes in the Comptonizing corona during phases of high luminosity (Gleissner et al. 2003), however, this interpretation was wrong.

Instead, the ‘‘arches’’ are caused by buffer overflows in the PCA hardware (see also Gierliński & Zdziarski 2003; van Straaten et al. 2003). For the binned data mode

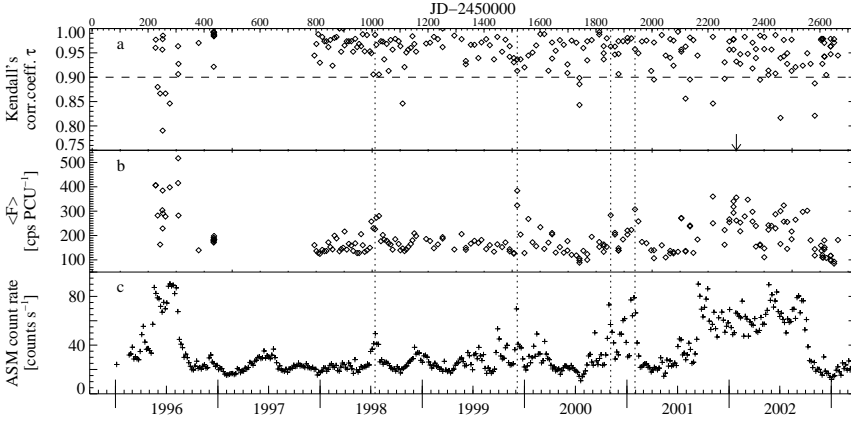


Figure 3.2: **a)** Kendall's τ , the long-dashed line indicates τ_{\min} , observations with $\tau < \tau_{\min}$ were not included in the further analysis. **b)** Mean *RXTE* PCA count rate for energy band 2 ($\sim 4\text{--}6$ keV). **c)** Mean *RXTE* ASM count rate, rebinned to a resolution of 5.6 days, the orbital period of Cyg X-1 (Brocksopp et al. 1999a). The four most prominent intermediate states are indicated by vertical dotted lines.

B_2ms_8B_0_35_Q, with which most of our low energy data are taken, 4 bit wide counters are used to form the binned spectrum during each 2 msec binning interval. During phases of very high flux, which are especially likely during short outbursts possible during the failed state transitions, these buffers will overflow. Due to the softness of the X-ray spectrum during the failed state transitions, the likelihood for such overflows is highest in the lowest energy band. The buffer overflows become apparent when comparing the lightcurve of the binned data mode with the lightcurve as determined, e.g., from the GoodXenon data, which does not suffer from these problems. Except for phases of high flux, these lightcurves agree. During phases of high flux, however, multiples of 16 events are missing in the lightcurve from the binned data. Since the buffer overflows only occur for a few bins of the high resolution lightcurve, the flux determination is barely affected, however, the rms is reduced and “arches” such as that shown in Fig. 3.4 are observed. For the computation of the rms-flux relationship, we therefore resorted to using energy band 2, where the overall photon flux is lower and buffer overflows do not occur.

Note that GoodXenon data are not available for all observations considered here, furthermore, the energy resolution of the GoodXenon data is not good enough to allow the study of other timing parameters. We note that the rms-flux relationship is especially sensitive to buffer overflows as the data are sorted according to flux. For the determination, e.g., of power spectra, longer lightcurves are chosen, and the buffer

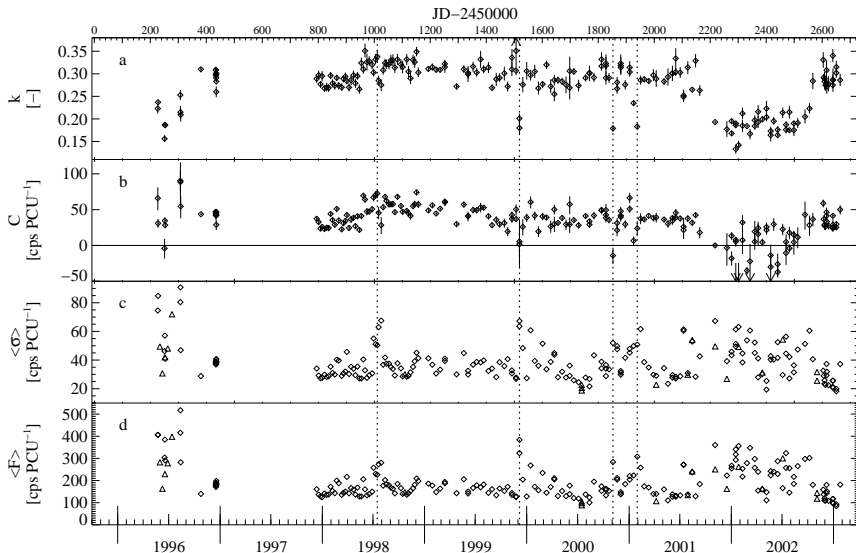


Figure 3.3: Fit parameters and Cyg X-1 system properties for energy band 2 ($\sim 4\text{--}6$ keV). **a)** Slope, and **b)** x -axis intercept of the rms-flux-relationship, **c)** mean rms value, $\langle\sigma\rangle$, **d)** mean *RXTE* PCA count rate for energy band 2. Error bars given for slope and intercept are uncertainties at the 90% confidence level for two interesting parameters. Triangles indicate observations which cannot be described by a linear rms-flux relation (i.e., $\tau < \tau_{\min}$).

overflows are only apparent in a slight change of the rms level of the power spectrum. Therefore, buffer overflows at the level seen in the data here only very slightly affect the normalization of the PSDs such as those used in Pottschmidt et al. (2003) and do not have any influence on our earlier results.

3.2 Results

3.2.1 Evolution of Slope and Intercept

Figs. 3.2a–c show Kendall’s τ , the mean *RXTE* PCA count rate, $\langle F \rangle$, for energy band 2 ($\sim 4\text{--}6$ keV), and the *RXTE* All Sky Monitor (ASM; Levine et al. 1996) count rate for the time from 1996 to 2003. In Figs. 3.2b and c the soft state that took place 1996 March–September and the “soft state” of 2001 October–2002 October are reflected by increased count rates. The fact that the failed transitions and the soft state behavior of 2001/2002 look similar in C together with the observation that the radio emission is not always quenched in the 2001/2002 soft state (G.G. Pooley,

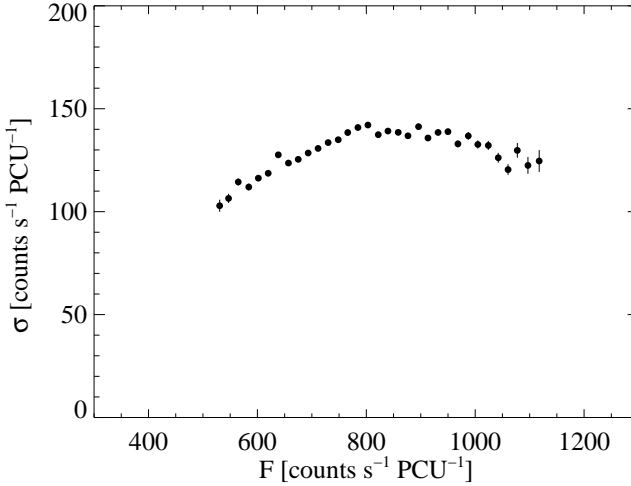


Figure 3.4: In energy band 1 the rms-flux relation for observation 2000 Nov 03, just as several other high flux observations during intermediate and soft states, displays an “arch-like” form. The given error bars are at the 1σ level.

private communication), allows one to speculate that the 2001/2002 soft state shows intermediate state phases (see, e.g., Zdziarski et al. 2002). Given the uncertain nature of the 2001/2002 soft state we must be careful not to assume that it is a canonical soft state or equal to the 1996 soft state without further proof (Wilms et al. 2004, in prep.). Between the 1996 soft state and the 2001/2002 interval, Cyg X-1 was usually found in the hard state, infrequently interrupted by the “failed state transitions” described in Pottschmidt et al. (2003) and section 3.2.2.

Figs. 3.3a–d show the fit parameters k , C , mean absolute rms variability, $\langle\sigma\rangle$, and mean *RXTE* PCA count rate, $\langle F\rangle$. The most apparent correlation is between $\langle\sigma\rangle$ and $\langle F\rangle$. To examine this correlation, we display the rms-flux relation of the long term variations in σ in Fig. 3.5. A tight linear correlation between $\langle\sigma\rangle$ and $\langle F\rangle$ can be seen in the hard state and, with a slightly lower slope, in the soft state data. It seems that the linear rms-flux relation observed on short time scales also applies on much longer time scales. A least χ^2 fit ($\chi^2 = 15\,589$ for 161 dof) of a linear model to the hard state provides $k = 0.2230 \pm 0.0003$ and an intercept of $C = 6.8 \pm 0.2 \text{ counts s}^{-1} \text{ PCU}^{-1}$. These values of k and C are lower than the values typically observed in the short term rms-flux relation. The corresponding fit for the soft state data ($\chi^2 = 30\,660$ for

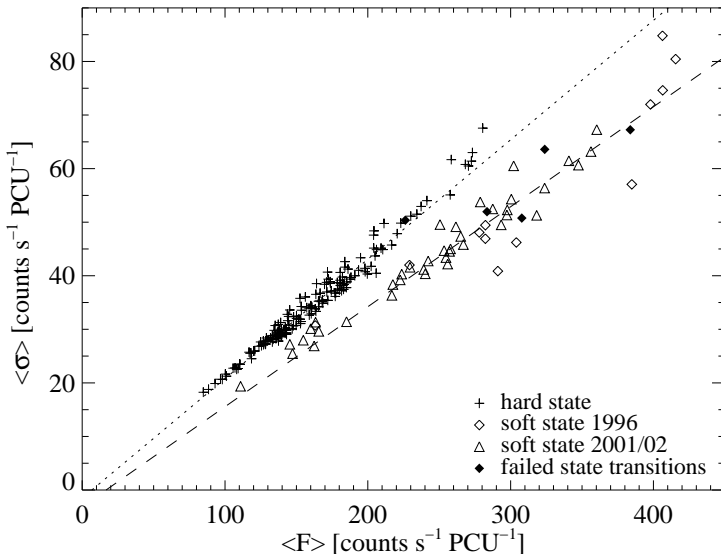


Figure 3.5: Mean rms variability, $\langle\sigma\rangle$, as a function of mean PCA count rate, $\langle F\rangle$. The hard state observations line up to follow a linear rms-flux relationship. There is also a linear rms-flux relationship for the soft state observations, but with a slightly smaller slope.

50 dof) provides a slope of $k = 0.1867 \pm 0.0004$ and an intercept at the flux axis of $C = 16.8 \pm 0.6 \text{ counts s}^{-1} \text{ PCU}^{-1}$. The values for the failed state transitions are associated with either the hard state or the soft state data.

We next consider the long term behavior of k (Fig. 3.3a). During the soft states of 1996 and 2001/2002, k takes a significantly lower value than during the hard state. During the last three “failed state transitions” before the 2001/2002 soft state k decreases to the soft state level. The values of the intercept show different levels, too: while in the 1996 soft state C is larger than or equal to the hard state, C in the 2001/2002 “soft state” is smaller than in the hard state. This may be connected to the special soft state character of the 2001/2002 interval. The detailed characteristics of the rms-flux relation in the different states will be discussed in the following sections.

One of the main results of a previous work on Cyg X-1 was that in 1998 May a change of the general long term behavior of Cyg X-1 from a “quiet hard state” to a “flaring hard state” took place that coincided with a change in the PSD shape, resulting in a *decrease* of the relative rms amplitude from an average of $36 \pm 1\%$ to $29 \pm 1\%$, for the total 2–13.1 keV power spectrum (Pottschmidt et al. 2003, Fig. 3d).

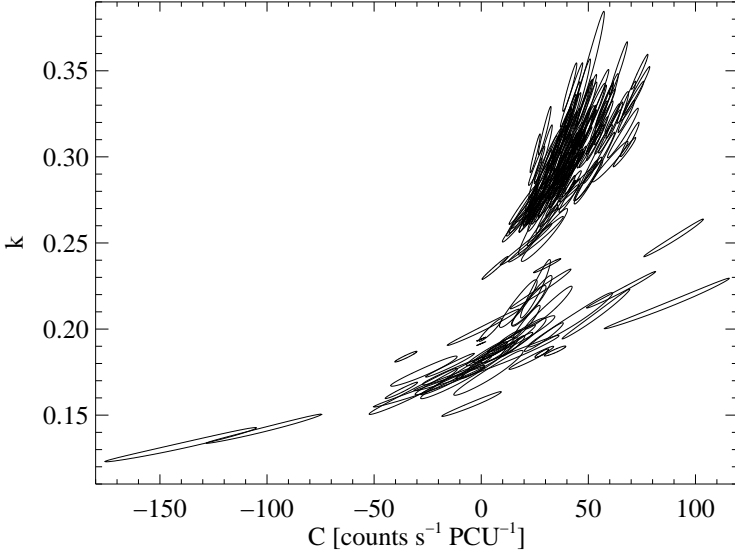


Figure 3.6: Contour plot at the 90% confidence level showing the two fit parameters slope and intercept at the flux axis.

This change is seen in Fig. 3.3 as a rise of k and C , while the mean rms value, $\langle\sigma\rangle$, stays on a constant level. This apparent discrepancy can be explained by taking into account that the total rms is measured from $\sim 2 \times 10^{-3}$ Hz to 32 Hz in Pottschmidt et al. (2003), i.e., over a much broader frequency range than here. As we show below (section 3.3.2), the drop in the global rms in 1998 May is due to a change of the PSD outside of the frequency range covered by our measurements of the rms-flux relationship.

To illustrate the correlation between k and C , Fig. 3.6 shows the 90% confidence contours for these parameters. The points in the k - C -plane fall into two separate regions corresponding to hard and soft states. A possible correlation between k and C can be seen within the soft state, but a much stronger correlation between k and C is present within the hard state. Interestingly, the k - C values in the hard state fall into a distinctive, fan-like shape, which suggests that a more fundamental relation may underly the k - C correlation in that state. The “fan” appears to converge at the values of k and C measured for the long term rms-flux relation of the hard state (Fig. 3.5), suggesting that the pattern of k and C observed in the hard state may be related to the long term rms behavior.

In fact it is easy to see how a linear long term rms-flux relation can produce the

observed fan-like shape of the k - C correlation in the low state. First, consider that the mean σ of the i th observation, $\langle\sigma_i\rangle$, is related to the mean flux, $\langle F_i\rangle$, by

$$\langle\sigma_i\rangle = k_i(\langle F_i\rangle - C_i) \quad (3.7)$$

where k_i and C_i are the k and C values determined from the rms-flux relation of that observation. According to Fig. 3.5, $\langle\sigma_i\rangle$ is also given by

$$\langle\sigma_i\rangle = k_{\text{long}}(\langle F_i\rangle - C_{\text{long}}) \quad (3.8)$$

where k_{long} and C_{long} are the k and C values of the long term rms-flux relation ($k_{\text{long}} = 0.2230$, $C_{\text{long}} = 6.8$). From eqs. (3.7) and (3.8) it is easy to see that

$$k_i = \frac{k_{\text{long}}(\langle F_i\rangle - C_{\text{long}})}{\langle F_i\rangle - C_i} \quad (3.9)$$

and

$$C_i = \frac{k_i\langle F_i\rangle - k_{\text{long}}(\langle F_i\rangle - C_{\text{long}})}{k_i} \quad (3.10)$$

The distribution of the k_i , C_i values is thus caused by the requirement to maintain the rms-flux correlation on all time scales. The “fan like” distribution of the individual values is the result of the requirement that for $k_i \rightarrow k_{\text{long}}$, $C_i \rightarrow C_{\text{long}}$. Confirming earlier results, we find that k_i is not correlated with flux. In order to maintain the long term rms-flux correlation, this results in a corresponding scatter of the values of C_i , forming the “fan”. We can test this directly by plotting k_i versus $(\langle F_i\rangle - C_{\text{long}})/(\langle F_i\rangle - C_i)$ (Fig. 3.7), which gives a linear relation ($\chi^2 = 308$ for 153 dof) with slope 0.2312 ± 0.0004 ($\approx k_{\text{long}}$), as expected from eq. (3.9). We conclude that the various values of k , C and mean flux $\langle F\rangle$ map out a “fundamental plane” in the low state, governed by the requirement that the long term linear rms-flux relation is maintained. We will examine the consequences of this fact in detail in section 3.3.

Now that we have described the general evolution of the parameters of the rms-flux relationship, we turn to describing the individual relations in greater detail.

3.2.2 The rms-Flux Relation in the Hard and Soft State and During “Failed State Transitions”

The high values of Kendall’s τ in Fig. 3.2a prove that a linear rms-flux relation is valid throughout all states, the hard state *and* the soft state *and* the “failed state transitions”, with relatively few outliers. Note, however, that a number of soft state observations, predominantly during the atypical 2001/2002 “soft state”, have rms-flux

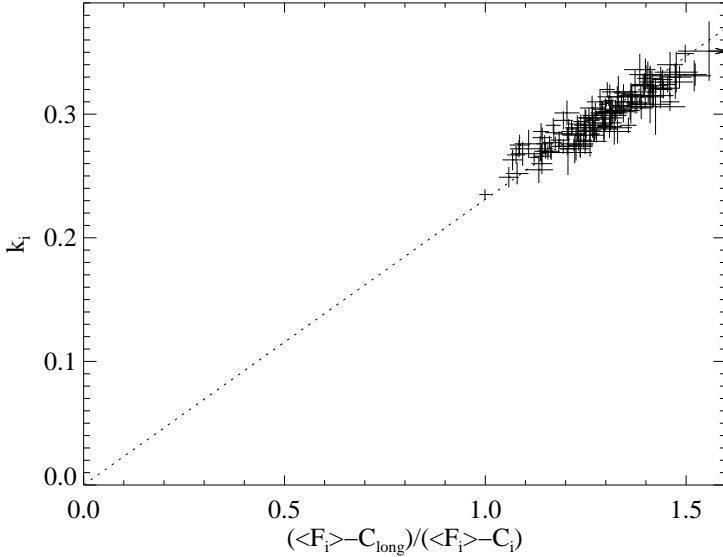


Figure 3.7: For hard state observations, k_i versus $(\langle F_i \rangle - C_{\text{long}}) / (\langle F_i \rangle - C_i)$ gives a linear relation $y = bx$ with slope $b = 0.2312$. The error bars on k are the formal 1σ error, the horizontal error bars are calculated from propagating formal 1σ errors of F_i and C_i .

relations with a negative flux offset C (see Fig. 3.3b). This negative offset cannot be explained if, for these cases, C simply represents a constant component to the lightcurve, but can easily be explained if C represents a component with *constant rms*. In Fig. 3.8a–c we give examples for the overall rms-flux linearity.

There are a small number of observations which cannot be described with a linear model. These deviations from a linear relation have two principal reasons: (1) As discussed in section 3.1.3, many observations with $\tau < \tau_{\text{min}}$ simply have a short observation time, so that the number of segments per bin is relatively low which produces the strong scatter, resulting in a poor correlation. (2) In contrast, the “wavy” rms-flux relation shown in Fig. 3.9b results from short term variations in the parameters C and/or k of a linear rms-flux relation. If a single observation (on time scales of a few 100 s) consists of several parts, each with different average flux (see Fig. 3.9a), then the superposition of the linear rms-flux relations of all parts will result in a “wavy” rms-flux relation, as each part displays a slightly different C and/or k value.

To describe the flaring events when Cyg X-1 attempts the change from the common hard state into the soft state, without reaching the soft state, we coined the term “failed state transitions” (Pottschmidt et al. 2000, 2003). Depending on how far its state

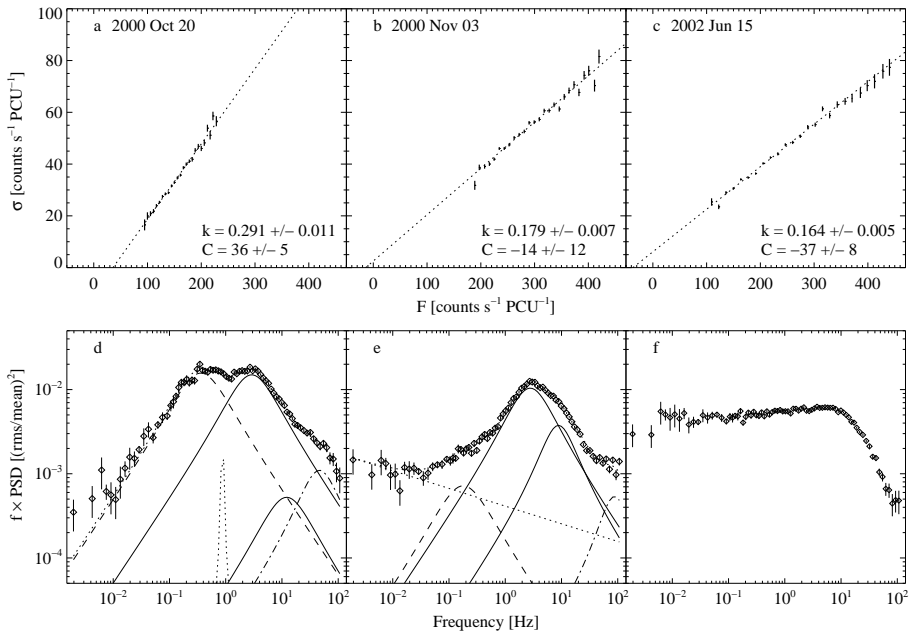


Figure 3.8: Linear rms-flux relations during exemplary **a**) hard state, **b**) “failed state transition”, and **c**) soft state observations. **d**)–**f**) give the corresponding PSDs. Error bars of the rms variability are at the 1σ level. See Pottschmidt et al. (2003) for a description of the PSD decomposition into single Lorentzians (does not work for soft state observation **f**)).

evolves, during these failed transitions Cyg X-1 can reach the intermediate state as defined by Belloni et al. (1996), or its behavior can remain hard state-like during these flares.

We examined four “failed state transitions” that were covered by *RXTE* observations in detail: 1998 July 15, 1999 December 05 (extracted as two separate lightcurve parts), 2000 November 03, and 2001 January 29 (probably a short soft state, see Cui et al. 2002). The values of k and C of the first failed state transition on 1998 July 15 are not different from the surrounding hard state observations. During the latter three failed state transitions, however, the values of k and C change to the soft state level. For one exemplary observation on 2000 November 03, this behavior is displayed in Fig. 3.8b. Comparing the failed state transition with the hard state observation immediately before (Fig. 3.8a), the rms-flux relation of 2000 November 03 changes to a lower slope and a small, *negative* intercept C during the “failed state transition” itself. The PSD of this observation shows that this change in the rms-flux relation is

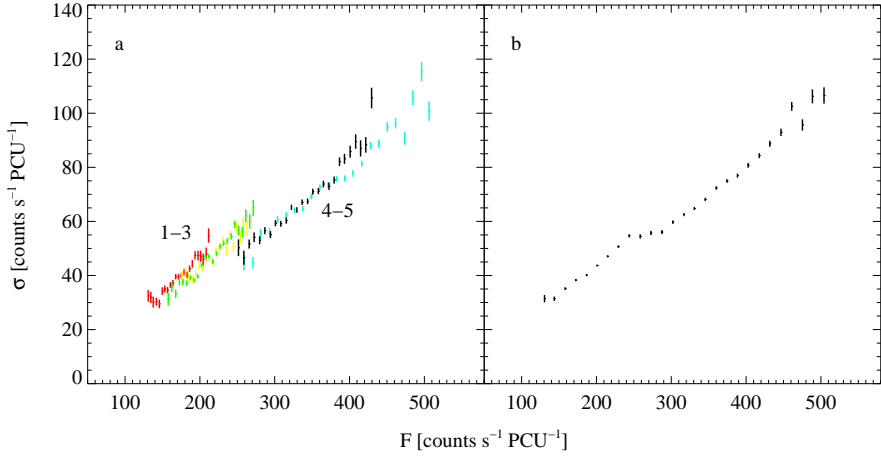


Figure 3.9: The observation of 2002 Feb 25 consists of five short segments 1–5. **a)** Segments 1–3 are at lower flux, while 4 and 5 are at higher flux, so that the rms-flux relations for each part are shifted with respect to each other. **b)** The superposition of all parts results in a “wavy” rms-flux relation. Error bars are at the 1σ level.

accompanied by a decreasing Lorentzian component L_1 and an increasing Lorentzian component L_3 (Fig. 3.8d–e).

3.2.3 Spectral Dependence of the rms-Flux Relation

We confirm a correlation between the photon spectral index, Γ , i.e., the hardness of the spectrum, and the mean rms, $\langle\sigma\rangle$, of the examined observations. In the hard state, the photon spectrum of each observation can roughly be described as the sum of a power-law spectrum $E^{-\Gamma}$ with photon index Γ and a multi-temperature disk black body (Mitsuda et al. 1984). The correlation of Fig. 3.10a takes into account only hard state and “failed state transition” observations and shows that $\langle\sigma\rangle$ increases as the spectrum grows softer. As rms variability and flux are linearly correlated in the hard state, this correlation between Γ and $\langle\sigma\rangle$ is equivalent to a correlation between Γ and flux. A similar result with *RXTE* ASM data of Cyg X-1 has been recently shown by Zdziarski et al. (2002), who found a very strong hardness-flux anticorrelation in the hard state.

We note that we adopt the definition of Pottschmidt et al. (2003), using the term “failed state transitions” for those observations which exhibit a significantly increased time lag compared to its typical value, since the X-ray time lag seems to be a more sensitive indicator for state changes than the X-ray spectrum. As has been already

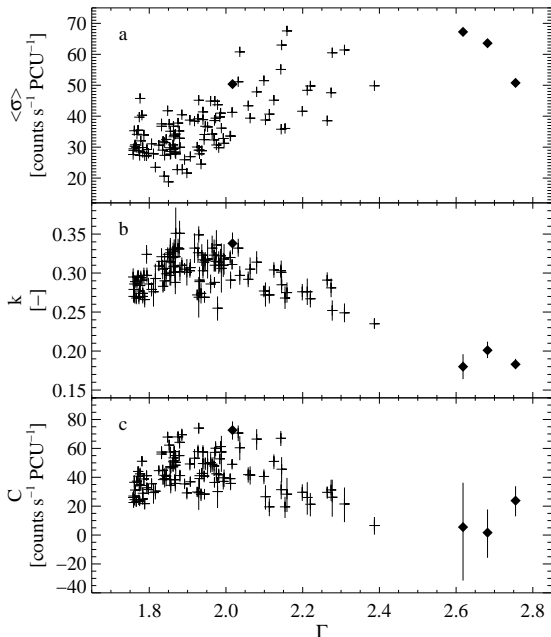


Figure 3.10: **a)** Mean rms variability, $\langle\sigma\rangle$, **b)** slope, k , and **c)** flux intercept, C , as a function of photon spectral index, Γ , for failed state transitions and the hard state observations. Diamonds designate “failed state transitions”, crosses are for hard state observations. Error bars for k and C are given at the 90% confidence level for two interesting parameters.

been noted in section 3.2.2 there are only four corresponding observations.

The filled diamond at $\Gamma \sim 2$ in Fig. 3.10 belongs to the “failed state transition” of 1998 July 15. The fact that this data point is situated within the value range of hard state observations in Figs. 3.5 and 3.10 confirms that this “failed state transition” has to be treated separately and classified as being close to the hard state, as already mentioned in section 3.2.2. Allowing for the split in values of k and C , respectively, between the hard state and failed state transition data, any correlation between the photon index and k , or C , cannot easily be detected.

So far we concentrated on the rms-flux relation in the second lowest energy band, i.e., energy band 2 in the range $\sim 4\text{--}6\text{ keV}$. This approach is justified as the linear rms-flux relation is found to be valid for all energy bands considered here (see, e.g., Fig. 3.11), such that the general behavior described for energy band 2 is also seen in the other bands. Even the rms-flux relation in energy band 3 which contains the iron

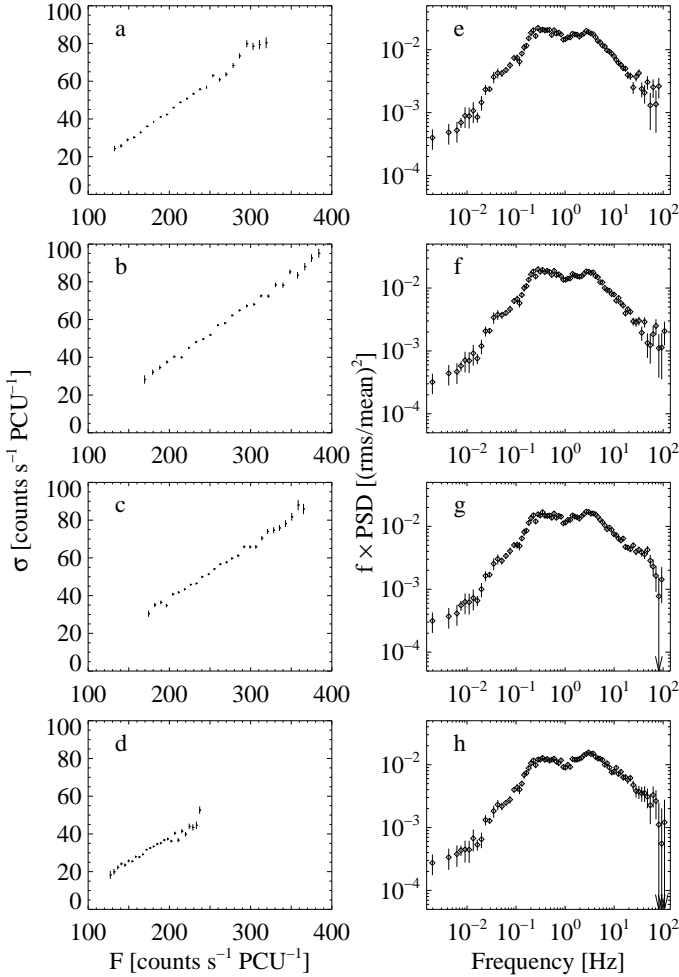


Figure 3.11: Shape of **a**)-**d**) the rms-flux relation and **e**)-**h**) the corresponding PSD for the observation of 1999 May 21 for energy bands 2–5, respectively.

K line does not show a different behavior, in agreement with the results of Maccarone & Coppi (2002b) that the iron line tracks the continuum at least in the soft and transition states. Nevertheless, there are subtle differences in the shape of the rms-flux correlation.

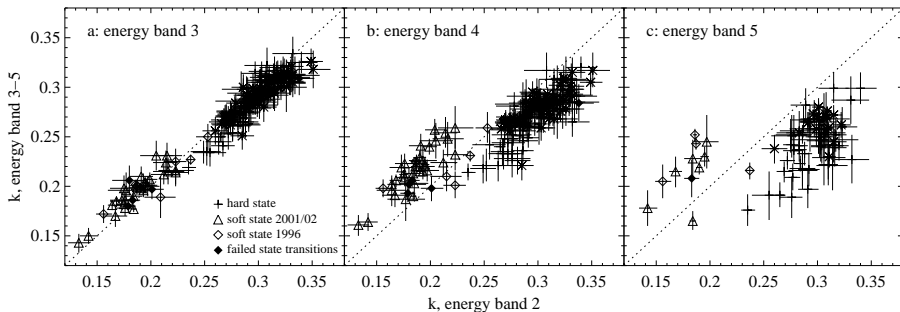


Figure 3.12: Slope of energy bands 3–5 plotted against the slope of energy band 2. The dotted line indicates $k_i = k_2$ where $i = \text{band 3 through 5}$. Error bars are at the 90% confidence level for two interesting parameters.

Comparing the values of k and C for the different energy bands, our energy resolved results for the rms-flux correlation show that k , which represents the fractional rms variability of the time variable component of the emission in the 1–32 Hz band, generally decreases with energy when the source is in the hard state (Fig. 3.12), in agreement with earlier results (e.g., Nowak et al. 1998). The same is true for C (see Fig. 3.13). For the highest energy band 5, our analysis reveals that k and C only slightly correlate with energy band 2 (Figs. 3.12c and 3.13c). This result confirms earlier work claiming only a ‘loose coupling’ between the source variability at low and at high energies (Życki 2003; Churazov et al. 2001; Maccarone et al. 2000; Gilfanov et al. 1999). In terms of Compton corona models, the fraction of photons from the accretion disk significantly decreases when proceeding from energy band 2 to energy band 5. Therefore we take our result to confirm earlier claims that the variability properties of Cyg X-1 are driven by coronal fluctuations and not by changes in the soft photon input to the putative Compton corona (Maccarone et al. 2000; Churazov et al. 2001, and references therein).

To examine the overall spectral shapes of the two variability components characterized by C and k , respectively, we plotted these values for the energy bands 2–5, normalizing C by $\langle F \rangle$ to account for the instrument response. Fig. 3.14 shows two examples with different photon spectral index, Γ . For most observations with Γ lower than ~ 2.0 , which means for the majority of hard state observations, the spectral shapes of C and of k are similar, but the spectral shape of C tends to be somewhat flatter: both C and k show a soft energy spectrum, i.e., higher values at low energies and lower values at higher energies (Figs. 3.14a–b). When we proceed to higher Γ , observations begin to display a flat or even tilted spectrum, i.e. lower values at low energies and higher values at higher energies, more pronounced for C than for

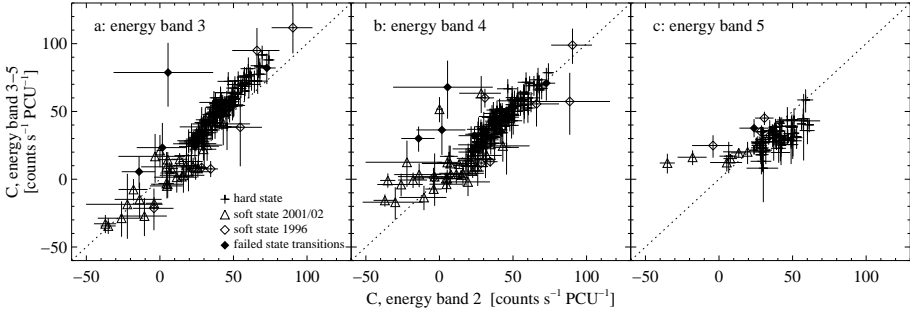


Figure 3.13: Behavior of C for energy bands 3 through 5, as a function of C measured for energy band 2. The dotted line indicates $C_i = C_2$ where $i = \text{band 3 through 5}$. Error bars are at the 90% confidence level for two interesting parameters.

k (Figs. 3.14c–d). The change in the shape of the normalized C (cf. Figs. 3.14a and c) is caused by the combination of an intrinsic change in the spectral shape of the unnormalized C and a change in the spectral shape of $\langle F \rangle$. Suggestions that the two variability components C and k , representing a constant and a variable rms component, will have basically different energy shapes cannot be confirmed, but to a certain degree in the low state the spectral shape of C is flatter and harder than the spectral shape of k .

3.2.4 The rms-Flux Relation on Short Time Scales

The fact that σ tracks the flux implies that the “lightcurve” of the rms values is similar to the flux lightcurve. This fact can be used to probe how the rms responds to flux changes on short time scales. For example, if the rms does indeed track variations on all time scales, the PSD of the “rms lightcurve” should look similar to the PSD of the conventional “flux lightcurve”. In contrast, if the rms only tracks variations on time scales longer than, say, 10 s, the PSD of the rms lightcurve should be sharply cut off at 0.1 Hz. In order to test this issue we created 0.25 s lightcurve segments and calculated F and σ for each of these segments to make flux and rms lightcurves. From these lightcurves, we calculated the PSDs (shown for an arbitrarily chosen observation in Fig. 3.15). In this case, we do not correct the rms lightcurve for Poisson noise, since the stochastic nature of the noise process means that such a correction is only possible when averaging over comparably long time intervals. Note, however, that the effect of the Poisson noise and intrinsic noise contributions to the rms lightcurve is to add power to the rms PSD at high frequencies, not to cause spurious high-frequency cutoffs or breaks.

Over the frequency range $\sim 0.01\text{--}0.2$ Hz the rebinned PSDs show the same features,

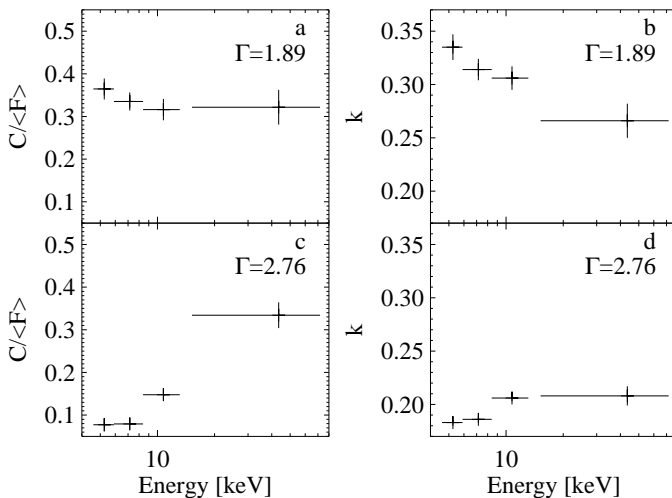


Figure 3.14: Spectral shapes of the two variability components characterized by C and k , respectively. C has been normalized by $\langle F \rangle$. **a-b)** show a typical hard state observation (2001 April 7) with $\Gamma = 1.89$, whereas **c-d)** give an example of the tilted spectral shapes which can be found for higher Γ (“failed state transition” observation of 2001 Jan 29 with $\Gamma = 2.76$).

as indicated by the flat ratio in Fig. 3.15c. Therefore it is likely that the rms-flux relation is fulfilled on time scales from 5 s to 100 s. Above 0.2 Hz, however, Poisson noise starts to dominate the rms PSD such that the shape of the rms and flux PSDs cannot be compared.

Similar tests dealing with the variability on different time scales have been discussed by Mineshige et al. (1994b) and Maccarone & Coppi (2002a).

3.3 Discussion

3.3.1 The Origin of the rms-Flux Relation

Uttley & McHardy (2001) have interpreted the rms-flux relation in terms of the disk fluctuation model of Lyubarskii (1997), where variations in the accretion rate occur at various radii and propagate inwards to modulate the X-ray emission. The fact that variations at larger radii should have longer characteristic time scales naturally explains the fact that the short term rms variations are modulated by longer time scale flux changes. As the slower variations in the accretion flow propagate inwards they are able to modulate the variations on shorter time scales. Kotov et al. (2001)

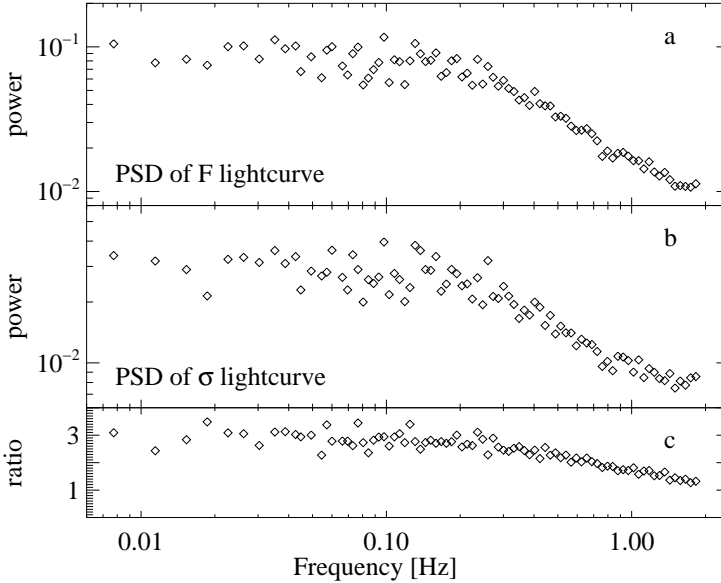


Figure 3.15: PSDs of **a)** F lightcurve and **b)** σ lightcurve for the hard state observation on 1999 July 05. The original flux lightcurve with time resolution of $\Delta t = 2^{-8}$ s has been divided into 0.25 s segments, and the frequency range $\nu = 4\text{--}128$ Hz was chosen for calculation of the rms variability of each segment. To compute PSDs from the flux and the rms lightcurves – consequently both with the time resolution of the segment length $\Delta t = 0.25$ s – segments of 1024 time elements ($= 1024 \times 0.25$ s $= 256$ s) were used, thus resulting in a frequency range from $\nu_{\min} = 0.004$ Hz to $\nu_{\max} = 2$ Hz. We rebinned this range to 84 logarithmically spaced bins. **c)** Ratio of the F lightcurve PSD to the σ lightcurve PSD in order to quantify the similarity of the two PSDs.

have extended this model by introducing an extended X-ray emitting region with a temperature gradient, to explain the frequency dependent time lags between hard and soft bands observed in Cyg X-1 (Pottschmidt et al. 2000).

Churazov et al. (2001) have pointed out that in a standard thin disk, viscous damping will smooth accretion rate fluctuations on a viscous time scale, i.e., before they reach the inner disk, implying that for the Lyubarskii (1997) model to work, the fluctuations in accretion rate must happen in an optically thin or geometrically thick flow, such as an advection dominated accretion flow (ADAF) or another type of thick disk. We have shown that the linear rms-flux relation is seen in both high and low flux states, so that it very well might be associated with some component of the system that is common to both states. Since the X-ray variability during the soft state appears

to be associated with the power-law emission rather than thermal emission from the disk (which may be constant, Churazov et al. 2001), it seems likely that the rms-flux relation is associated directly with a corona which is present in both hard and soft states. We therefore speculate that the rms-flux relation in Cyg X-1 (and probably also other objects showing linear rms-flux relations) may present evidence for accretion rate variations in a *fluctuating coronal accretion flow* (see, e.g., Smith et al. 2002; van der Klis 2001, and references therein). The suggestion that the corona itself accretes has been used to explain a number of observational features of both AGN and galactic BH systems (Witt et al. 1997), and since an optically thin coronal accretion flow is similar to an ADAF, such a model would not encounter the problems faced by a thin disk origin for the accretion variations (Churazov et al. 2001).

3.3.2 The Long Term rms-Flux Relation

In the previous sections we have shown that the linear rms-flux relation seems to apply on very long time scales, since the average 1–32 Hz rms of an observation scales linearly with the average flux of the observation. The hard and soft state data form two separate long term rms-flux relations, with different slopes k_{long} (somewhat lower in the soft state, $k_{\text{long}} = 0.19$ versus $k_{\text{long}} = 0.22$ in the hard state). Intriguingly, the flux-offsets C_{long} in the long term rms-flux relations of both hard and soft states are very close to zero, and certainly of much smaller amplitude than the typical offsets observed in the short term rms-flux relations of either state. The scatter in the hard state long term rms-flux relation is particularly small.

Combined with the almost-zero offset of the long term relation, this tight correlation implies that the fractional rms of the 1–32 Hz variability in the hard state is remarkably constant (similar to k_{long} , i.e., $\sim 22\%$). This result is rather surprising because the hard state PSD is clearly not stationary, i.e., the Lorentzians which successfully describe the PSD change significantly in both peak frequency and fractional rms (Pottschmidt et al. 2003). The most obvious example of such a change in the PSD can be seen in 1998 May (see Pottschmidt et al. 2003, Fig. 3) when the peak frequencies of the Lorentzians simultaneously increase, and the fractional rms of the L_3 Lorentzian (which lies between 3–10 Hz) and the fractional rms of the total PSD both decrease significantly. However, despite such a marked change in the PSD, the data before and after 1998 May lie along the same long term hard state rms-flux relation. The fact that the fractional rms in the 1–32 Hz band seems undisturbed by significant changes in the PSD suggests some sort of conservation of fractional rms at high frequencies, even though the low-frequency (and hence the total) fractional rms changes significantly. Although the specific 1–32 Hz band chosen to measure the rms-flux relation is somewhat arbitrary, we point out that the bulk of the power in this band is associated with the L_2 and L_3 Lorentzians, and the band fully encompasses the range of frequencies between 3–10 Hz in which a strong and well-defined anti-correlation between

Lorentzian peak frequency and fractional rms is clearly seen (see Pottschmidt et al. 2003, Fig. 6). We suggest, therefore, that some process which conserves fractional rms above a few Hz may be at work, with fractional rms in the L_3 Lorentzian decreasing as the L_2 Lorentzian moves further into the 1–32 Hz band, resulting in a constant fractional rms in that band. We now examine how such a phenomenological model relates to the observed fundamental plane of short term rms-flux relation parameters k , C , and flux.

3.3.3 The hard state k - C - $\langle F \rangle$ fundamental plane

We have shown that the “fan shape” of the correlation between the rms-flux relation slope and its flux-offset in the hard state can be directly related to the long term rms-flux relation. The fact that k and C vary but the average 1–32 Hz rms *must* track the average flux explains the degeneracy in the correlation, which is the result of the various fluxes observed for a given pair of k and C values. Thus k , C , and $\langle F \rangle$ track out a fundamental plane which describes the forms the rms-flux relation can take in the hard state.

As noted by Uttley & McHardy (2001), C can be interpreted either simply as a constant-flux component to the lightcurve, or as a constant rms component. We concentrate on these two interpretations since they are the simplest possibilities, but it should be emphasized that there are numerous other forms the variability could take, e.g., a component of constant fractional rms.

We have shown that, in the soft state at least, C can be negative, which is only possible if the offset in this state represents a constant rms component. We argue that the existence of the k - C - $\langle F \rangle$ fundamental plane also suggests that C represents a constant rms component in the hard state. For example, consider an increase in the slope k between two observations, while keeping the average flux of the observations constant. The increase in k corresponds to an increase in the fractional rms of the linear rms-flux component of the lightcurve. In order to maintain the constant total fractional rms as given by the observed long term rms-flux relation, C must also increase. Therefore we suggest that both a constant rms component and a linear rms-flux component exist in the lightcurve and that the relative contribution of each varies in such a way that the sum of both components, the total fractional rms, is constant.

As a constraint to possible models it should be mentioned, as already noted in section 3.2.3, that the spectral shapes of k and C are generally similar, with C tending to a flatter/harder spectrum, and there is no obvious correlation between spectral index Γ and C , C_{long} , and k , respectively.

Part II

Radio–X-ray Relations

CHAPTER 4

Radio Emission of BH XRBs

“... a curious straight ray ... apparently connected with the nucleus by a thin line of matter.”

Heber D. Curtis (1872–1942), on the jet of M 87

4.1 Radio Emission

In astrophysics two basically different classes of emission are distinguished: thermal radiation and non-thermal radiation. A prominent type of thermal radiation is blackbody radiation, emitted by a perfect absorber entirely at temperature T . The main share of non-thermal radiation is released by highly energetic, usually relativistic particles. Synchrotron radiation, the relativistic analogon to cyclotron radiation, is the most efficient known mechanism for the production of intense radio emission. Highly relativistic electrons, usually with a power-law energy distribution, interact with magnetic fields, producing non-thermal radio emission which tends to be linearly polarized. In the following sections some basic radio relations are summarized, and thermal and non-thermal radiation, especially Synchrotron radiation, will be discussed from the radio aspect. The text generally follows the description as given by Rybicki & Lightman (1979) and Kraus (1986).

4.1.1 Basic Issues of Radio Observations

To facilitate the reading of this chapter, it may be useful to the X-ray astronomer to recapitulate some basics relevant to the radio band.

The Planck function gives the spectral energy distribution of a blackbody

$$B_{\nu}(T) = \frac{2h\nu^3/c^2}{\exp(h\nu/kT) - 1} \quad (4.1)$$

Although stars do not perfectly satisfy the conditions to be blackbody radiators, their spectra can be sufficiently well approximated by the Planck function. At low frequen-

cies, i.e., in the radio regime where the relation $h\nu \ll kT$ is valid, the Planck function can be approximated by the Rayleigh-Jeans law

$$I_\nu^{RJ}(T) = \frac{2\nu^2}{c^2}kT \quad (4.2)$$

To describe the brightness (specific intensity) of an extensive source, the brightness temperature T_b at a certain frequency is given by determining the temperature of a blackbody which has the same intensity I_ν . By using eq. (4.2), T_b is given by

$$I_\nu = \frac{2\nu^2}{c^2}kT_b \quad (4.3)$$

The concept of the brightness temperature has the great advantage to reduce specific intensity to the simple unit of Kelvin and to connect the observed emission with a fundamental property of the emitting medium. Thermal emitters in the radio regime have typical temperatures $T_b \lesssim 10^4$ K, whereas powerful non-thermal radio sources may exceed brightness temperatures of 10^{12} K (Bastian & Bridle 1995).

The unit of flux density, F_ν , is

$$1 \text{ Jansky (Jy)} = 10^{-26} \text{ W m}^{-2} \text{ Hz}^{-1} \quad (4.4)$$

In radio astronomy the spectral index is usually indicated by the symbol α . Here the definition

$$F_\nu \propto \nu^{-\alpha} \quad (4.5)$$

is used, resulting in a positive spectral index for non-thermal sources, which constitute the majority of all radio sources.

The beam width, ϕ_{radio} , is a measure of the angular resolution power of a radio telescope with mirror diameter D , and is usually given on the contour maps of the radio emission as the half power contour of the beam. It denotes the angle where the energy sensitivity has decreased to the half maximum, and is defined as

$$\phi_{\text{radio}} = 1.03 \frac{\lambda}{D_{\text{eff}}} \quad (4.6)$$

where ϕ is given in arc angle, λ is the radio wavelength, and $D_{\text{eff}} < D$ is the effective diameter of the mirror. Note that this definition of resolution power, as used in radio astronomy, slightly deviates from the definition of resolution power of an optical telescope, given as $\phi_{\text{optical}} = 1.22\lambda/D$.

When observing with several antennas, in order to derive the best estimate of the flux density from a known position, the various baselines need to be adjusted to get the correct phase differences, i.e., to establish the precise path difference for the signal

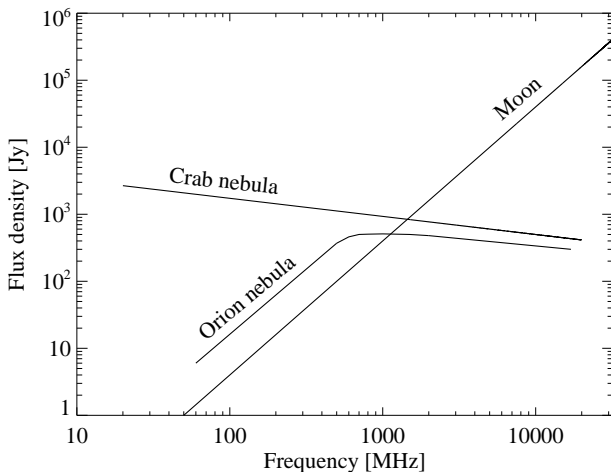


Figure 4.1: Spectra of typical radio sources. Moon: $\alpha = -2$, thermal solid body with a mean temperature of ~ 200 K. Orion nebula: $\alpha = -2$ to $\alpha \approx 0$, thermal ionized gas cloud. Crab nebula: $\alpha = 0.27$, non-thermal gas cloud, supernova remnant (after Kraus 1986, Fig. 8-9).

routes via the different antennas. This can be done by observing a calibrator source close in the sky at regular intervals, and deriving the best corrections. This usually takes a few minutes, and needs to be done at intervals of the order of 30 min. The precise interval is a matter of judgement and depends on conditions like weather (G.G. Pooley, private communication).

4.1.2 Thermal Radiation

Thermal radiation is emitted by a body as a result of its temperature T , i.e., the thermal motion of its electrons. In the case of thermally radiating electrons, their velocity obeys a Maxwellian distribution governed by the temperature T_e (eq. (1.15)). Prominent thermal contributions at radio wavelengths are the 21-cm line emission from H I regions, and the free-free radiation continuum from H II regions.

The optical depth, τ_ν , of a layer with geometrical thickness s is defined as the path integral of the absorption coefficient α_ν

$$\tau_\nu = \int_0^s \alpha_\nu ds \quad (4.7)$$

If the particles of a gas cloud with optical depth $\tau_\nu \gg 1$ have a thermal velocity distribution, the simplest form of thermal radiation, blackbody radiation $B_\nu(T)$, is set free.

Many thermal sources, e.g., stars like our Sun or the Moon, display a spectral index $\alpha = -2$ (Fig. 4.1) which is characteristic of the thermal radiation from a blackbody (cf. eq. (4.2)).

In the case of an ionized H II region, the absorption coefficient α_ν is proportional to n^2/ν^2 , where n is the free electron density. Thus a small optical depth τ_ν means high frequencies, and vice versa. For $\tau_\nu \ll 1$, it can be shown that the spectral index α of the radiating gas cloud will become 0, so that the spectrum becomes flat. Therefore, the overall spectrum of a thermal ionized source will be at $\alpha = -2$ for low frequencies, and then flattens to $\alpha = 0$ for high frequencies (cf. Orion Nebula in Fig. 4.1).

Neither of these thermal processes can produce the extremely bright radio emission seen in XRBs, as the brightness is limited by the maximum temperature of the plasma. The spectral index for most non-thermal sources lies between about +0.3 and +1.3, with an average value near +0.8 (Fig. 4.1). The synchrotron process is assumed to be the dominant emission mechanism in non-thermal sources.

4.1.3 Synchrotron Radiation

Synchrotron radiation (SR), first discovered in 1947 in a General Electric synchrotron, is released when highly relativistic charged particles are accelerated by a magnetic field. SR is assumed to be the responsible mechanism for the emission of most of the non-thermal radio sources. Descriptions of the properties of SR can be found, e.g., in Ginzburg & Syrovatskii (1965) and Blumenthal & Gould (1970).

The concept of SR can be summarized as follows: In a homogeneous magnetic field with flux density B , an electron e with rest mass m_e and velocity $v \approx c$ perpendicular to the magnetic field lines is subjected to radial acceleration by the Lorentz force and moves on a circular orbit with the gyro frequency

$$\omega_{\text{gyro}} = \frac{eB}{\gamma m_e c} \quad (4.8)$$

where the Lorentz factor

$$\gamma = (1 - \beta^2)^{-1/2} \quad (4.9)$$

with $\beta \equiv v/c$ is used. Because of beaming effects the emitted radiation is concentrated in a cone of emission of angular width $\sim 1/\gamma$ around the direction of the movement. Like the beacon from a lighthouse, this floodlight of duration Δt hits the observer with the frequency ω_{gyro} . The Fourier analysis of the series of flashes results in a spectral continuum with maximum at

$$\omega_{\text{max}} \approx \frac{1}{\Delta t} \propto \gamma^3 \omega_{\text{gyro}} \quad (4.10)$$

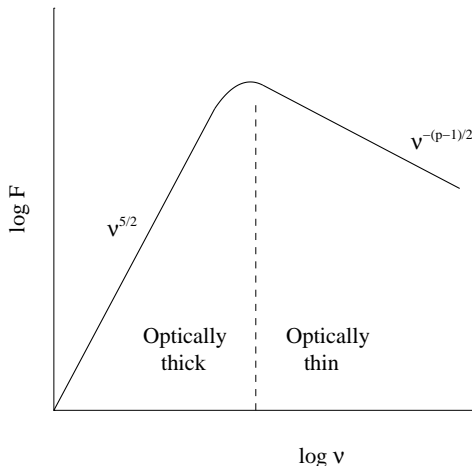


Figure 4.2: Synchrotron spectrum from a power-law distribution of electrons (after Rybicki & Lightman 1979, Fig. 6.12).

A characteristic feature of SR is its high degree of polarization. If the velocity component parallel to the magnetic field is not zero, the electron executes a helical motion around the field lines.

For an isotropic distribution of velocities the total emitted radiation power is

$$P_{\text{sync}} = \frac{4}{3} \frac{B^2}{8\pi} \sigma_T c \beta^2 \gamma^2 \quad (4.11)$$

where $\sigma_T = 8\pi r_0^2/3$ is the Thomson scattering cross section with the classical electron radius $r_0 = e^2/m_e c^2$. The inversely quadratic dependence on the mass of the radiating particle explains why only light particles like e^- and e^+ are of practical relevance for SR.

If synchrotron self-absorption, i.e., the re-absorption of the radiated SR by the electrons which become optically thick for the SR below a cutoff frequency, is included in the treatment, it can be shown that in the case of a non-thermal power-law distribution of electrons with particle distribution index p

$$N(E)dE \propto E^{-p}dE \quad (4.12)$$

where $N(E)dE$ is the number of electrons with energies between E and $E + dE$, the resulting spectrum can be divided into two regions depending on the optical depth

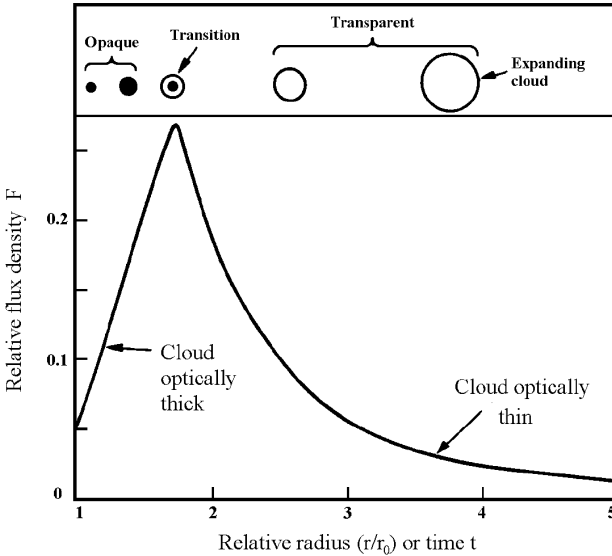


Figure 4.3: A uniformly expanding spherical electron cloud radiates at a fixed frequency in a characteristic manner depending on the radius, and optical depth, of the sphere (after Kraus 1986, Fig. 10-12).

$$\tau_\nu \propto \nu^{-(p+4)/2}$$

$$F_\nu = \begin{cases} j_\nu = \nu^{-(p-1)/2} & : \tau_\nu < 1 \\ S_\nu = \nu^{5/2} & : \tau_\nu > 1 \end{cases} \quad (4.13)$$

where j_ν is the emission coefficient, and S_ν is the source function (Fig. 4.2). The relationship

$$\alpha = \frac{p-1}{2} \quad (4.14)$$

in the optically thin case is of great importance as it allows to determine from the observed spectral index α the underlying distribution index p of the emitting particles. Therefore in the case of SR, a power-law distribution of electrons produces again a power-law distribution of synchrotron photons. Typical values of p lie in the range $1.6 < p < 3.0$ (van der Laan 1962).

The study of expanding nebulae of supernova remnants (e.g., Crab, Cas A) suggests that the magnetic field strength, H , and the energy of the electrons trapped in the cloud, E , will decrease inversely proportional to the square of the nebula radius r

(Shklovskii 1960). Concurrently, the observed SR flux density F_ν will decrease as

$$F_\nu \propto r^{-2(2\alpha+1)} \quad (4.15)$$

where, for constant expansion velocity, r can be substituted by time t . The frequency of maximum flux density also depends on r , as given by

$$\nu_{\max} \propto r^{-(4\alpha+5)/(\alpha+2.5)} \quad (4.16)$$

Assuming an expanding electron cloud with initial radius r_0 , it can be shown using eqs. (4.13), (4.15), and (4.16) that the emitted SR flux density F_ν at a fixed frequency ν_0 will increase until the cloud has become optically thin, and then decrease, as shown in Fig. 4.3.

A further radiative process when dealing with SR is the inverse Compton upscattering of the SR photons by electrons, the so-called synchrotron self-Compton (SSC) mechanism (Jones et al. 1974, and references therein), which is relevant, e.g., for the explanation of gamma-rays from blazars (Maraschi et al. 1992).

4.2 Radio–X-ray Observations of BH XRBs

Sco X-1, containing an accreting neutron star, was the first XRB which was identified as a radio source (Hjellming & Han 1995). With the extensive analysis of SS 433, the understanding of radio emission from XRBs was significantly brought forward (cf. section 1.3.3). The concept of radio emission from jets in MQs is actually borrowed from the theory of extragalactic radio jets (see, e.g., Bridle & Perley 1984), because except for the fact that the masses of AGN and MQs are apart by a factor between 10^6 and 10^9 , these two classes seem to be very similar. Today many XRBs are known to be strong radio emitters (Hjellming & Han 1995; Fender & Hendry 2000), and the non-thermal nature of their spectra and polarization features persuasively point to synchrotron radiation. Although only in a few cases a jet has been resolved¹, basically all models which are discussed today evoke outflows and synchrotron as the underlying mechanism.

In this section the characteristic properties of radio emission and the observational evidence for a relationship between radio and X-ray emission from prominent sources are discussed. A general overview of multifrequency connections in BHCs is given, e.g., in Zhang et al. (1997b).

¹Stirling et al. (2001) give an estimate that only about a dozen of the ~ 250 currently known XRBs possess radio jets.

4.2.1 On Long Time Scales

It has been noticed in many accreting BHCs that there exists a strong correlation between the radio emission and the hard state X-ray luminosity. In this state, radio emission is associated with a steady collimated outflow, i.e., a jet (Fender 2001). Non-thermal spectra, high polarization level, and high brightness temperature of the radio observations is strong evidence for self-absorbed synchrotron radiation as the underlying mechanism. This radio–X-ray coupling exclusively holds for the hard state, because the radio emission is attenuated until below detectability in the soft state. Synchronously with the decline of radio emission, the disappearance of outflow or jet structures is detected. While the radio behavior in the hard and the soft state is relatively clear, radio emission and corresponding outflows seems to be much more differentiated during other states, like intermediate and very high state. It is usually during these transitional states that strong radio flares in connection with single eruptive outflow events are observed.

The hard state being connected to a hot corona (section 1.5), a straight interpretation of the radio–X-ray observations is to assume a strong coupling between the corona region and the jet, most probably the corona acting as the base of the jet (see section 4.4.3). Gallo et al. (2003) proposed a firm correlation between the flux densities of radio, F_{radio} , and of X-ray, F_{X} , during the hard state which holds over three orders of magnitude in luminosity (Fig. 4.4)

$$F_{\text{radio}} \propto F_{\text{X}}^{0.7} \quad (4.17)$$

The major constituents of this correlation are the persistent source GX 339–4 and the transient source V404 Cyg, which display the greatest variability in X-ray luminosity among the set of analyzed BHCs. At high X-ray luminosities close to the Eddington limit L_{Edd} , a sharp turnover of the radio flux density down to an, in most cases, undetectable level occurs. Interpretations of this correlation will be given in section 4.4.

4.2.1.1 Cygnus X-1

Cyg X-1 shows persistent radio emission at 10–20 mJy in the hard state, while radio activity is strongly reduced during the soft state. The mean radio flux density at cm wavelengths is about 14 mJy in the hard state (Pooley et al. 1999), displaying a very flat radio spectrum with spectral index close to zero (see section 4.3.3). The radio flux is regularly seen to be modulated at several periods, one being the orbital period of 5.6 d which is superimposed on another one at ~ 150 d, probably associated to precession of the accretion disk (cf. section 1.6.1). Strong radio flares, disrupting the uniform hard state radio level, are observed only rarely, a very distinctive one recently, where the decay from a pronounced top level at 140 mJy back to the base level of ~ 15 mJy at 15 GHz within 1–2 hours was covered (G.G. Pooley, private communication).

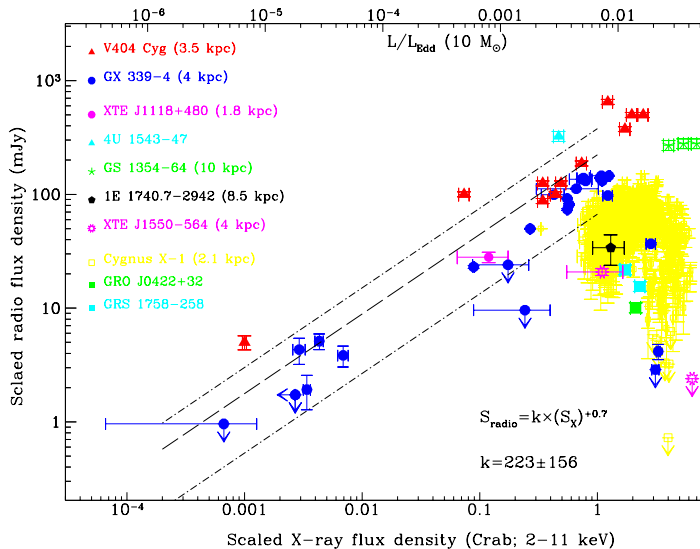


Figure 4.4: Between radio flux and X-ray flux, a strong correlation over a wide range of luminosities seems to exist in the hard state, which turns over at higher luminosities (Gallo et al. 2003, Fig. 2).

There seems to exist a hard state radio–X-ray correlation for Cyg X-1 on long time scales which is best discernable at high X-ray energies (20 keV–1 MeV), and during flaring states (Pooley et al. 1999; Brocksopp et al. 1999a). It has to be admitted, though, that this correlation is not comparable with the much clearer cases of, e.g., GX 339–4 (Hannikainen et al. 1998; Corbel et al. 2000) or V404 Cyg (Gallo et al. 2003). The stellar wind from HDE 226868, constituting a dispersive medium where the velocity of wave propagation is a function of frequency, thus smearing the radiation from Cyg X-1, may be invoked as a possible explanation. New data, testing these earlier results, will be presented in section 5.

4.2.2 On Short Time Scales

4.2.2.1 GRS 1915+105

GRS 1915+105 is known for its singularly complex X-ray behavior which is not observed in any other X-ray source (Belloni et al. 2000; Klein-Wolt et al. 2002). At the same time, this highly unusual and energetic system represents one of the most spectacular radio sources in our Galaxy, showing apparent superluminal motions in a two-sided ejection of synchrotron-emitting components from the source (Mirabel &

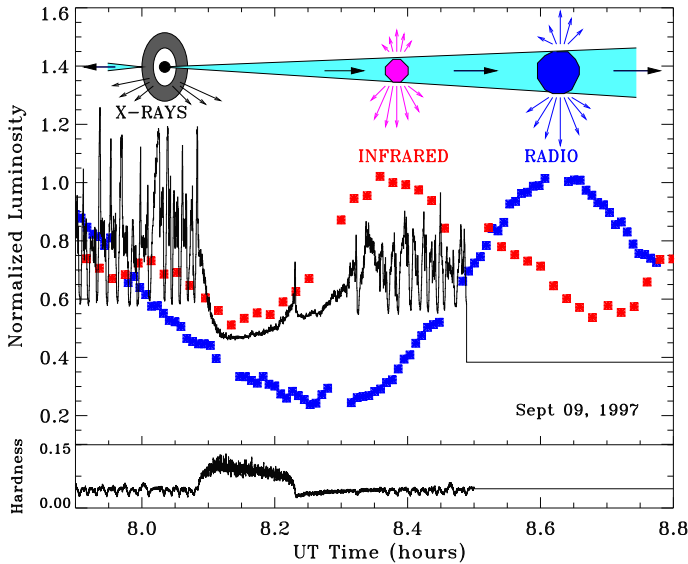


Figure 4.5: GRS 1915+105: within $\sim 1/2$ hour, an X-ray dip, followed by IR and radio peaks is observed (upper panel). Above the lightcurves, an interpretational diagram displays the ejection of a plasma cloud from the central object which becomes successively detectable at longer wavelengths. The bottom panel gives the hardness of the X-ray radiation (Mirabel et al. 1998, Fig. 7).

Rodríguez 1994; Fender et al. 1999).

GRS 1915+105 is a MQ which clearly shows radio–X-ray correlations on time scales of tens of minutes (see, e.g., Pooley & Fender 1997; Fender et al. 1997; Mirabel et al. 1998; Fender & Pooley 2000; Klein-Wolt et al. 2002). One peculiarity of its lightcurves is that they usually exhibit quasi-periodic dips in the X-ray emission which are related to radio oscillations with a typical period $P_{\text{osc}} \sim 20\text{--}45$ min (Pooley & Fender 1997; Mirabel et al. 1998). Fig. 4.5 shows a three-band observation of GRS 1915+105, where after an X-ray dip successively IR and radio peaks are observed. This relationship was interpreted within the framework of jet formation (cf. section 4.4.2) as a rapid disappearance of the inner accretion disk, followed by the ejection of relativistic plasma clouds in the form of synchrotron flares at IR and radio wavelengths (Mirabel et al. 1998). Assuming a one-to-one relation between an X-ray dip and a subsequent oscillation peak in the radio emission, Klein-Wolt et al. (2002), using a database of 101 simultaneous radio–X-ray observations, arrived at an estimated time delay of radio with respect to X-ray of 14–30 min.

4.2.2.2 GX 339–4

GX 339–4 displays similar spectral and timing properties as Cyg X-1 and is therefore assumed to be a black hole. The high brightness temperature of its radio counterpart suggests non-thermal synchrotron radiation from relativistic electrons (Corbel et al. 2000). While radio–X-ray correlations on time scales of weeks to months are clearly present, a similar correlation on time scales of hours as proposed by Corbel et al. (2000) is questionable.

4.3 Jets

Jets are found in various sizes and in a diversity of astrophysical host objects, like, e.g., very young stars, AGN, and also XRBs, as was mentioned in section 1.3.3. These outflows of matter are called jets because they are collimated up to large distances from the ejecting source² and because of their high velocities, sometimes reaching well into the relativistic regime. MQs, i.e., BH XRBs with accretion disk and jet emission, only show mildly relativistic jets (Meier et al. 2001, see, however, Fender et al. (2004) who report a MQ jet with $\Gamma_{\text{jet}} \geq 10$). Astrophysical jets are encountered as twins, reaching out from the central object in opposite directions. In many jets, single mass ejections can be resolved while in other systems the uniform jets seems to be formed by continuous outflow of matter. In all objects which possess jets also an accretion disk is present, establishing the close and vital relationship – ‘symbiosis’ as it was called by Falcke & Biermann (1995) – of jet and disk. The jet axis is generally assumed perpendicular to the disk plane (see, however, Maccarone 2002). Since the non-thermal radio emission detected from the jets is conventionally thought to be synchrotron radiation from relativistic electrons in the jet (Blandford & Königl 1979), magnetic fields have to be present in the ejected matter. In this section, the relativistic effects which are relevant for jet observation are reviewed, then the major jet-generating mechanisms being discussed are mentioned, and finally the main parameters of the jet of Cyg X-1 are given. Comprehensive reviews on jets of XRBs have been presented, e.g., by Mirabel et al. (1998) and Fender (2002).

4.3.1 Relativistic Effects

Describing the dynamics of matter at relativistic speeds $v \gtrsim 0.1c$, the Lorentz factor

$$\Gamma_{\text{jet}} = \left(1 - \frac{v^2}{c^2}\right)^{-1/2} \quad (4.18)$$

²Dealing with extragalactic radio jets, Bridle & Perley (1984) define that a jet must have an opening angle $\lesssim 15^\circ$.

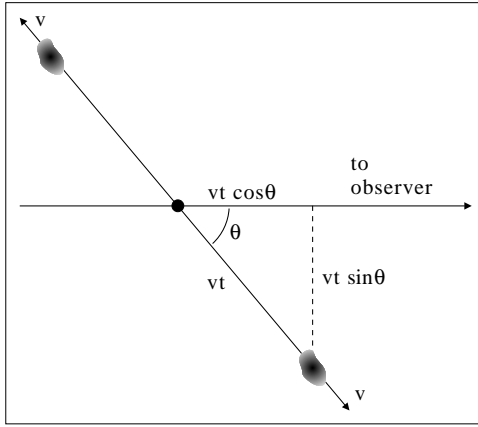


Figure 4.6: Schematic twin ejection of plasma blobs at speed v from a central source (Mirabel & Rodríguez 1999, Fig. 6).

is used. When dealing with jets, the bulk motion Lorentz factor Γ_{jet} gives the speed of the jet front, plowing through the ISM, and is to be distinguished from γ , indicating the velocity of single particles within the jet (cf. eq. (4.9)).

At high velocities β_{jet} , relativistic effects appear which will be discussed in this section. For the purpose of a clear description, a two-sided matter ejection with velocity $v = \beta_{\text{jet}}c$ from a central source is assumed, with $\theta = \theta_{\text{LOS}}$ measuring the angle between the jet direction and the line of sight of the observer (Fig. 4.6).

4.3.1.1 The Relativistic Doppler Effect

In close analogy to the classical Doppler effect, at relativistic speeds an emitted signal at frequency ν_0 will be observed at a different frequency ν . The Doppler factor, i.e., the ratio of ν/ν_0 , is given in the case of the approaching jet by

$$D_{\text{approach}} = \frac{\nu_{\text{approach}}}{\nu_0} = \frac{1}{\Gamma_{\text{jet}} (1 - \beta_{\text{jet}} \cos \theta_{\text{LOS}})} \quad (4.19)$$

and in the case of the receding jet by

$$D_{\text{recede}} = \frac{\nu_{\text{recede}}}{\nu_0} = \frac{1}{\Gamma_{\text{jet}} (1 + \beta_{\text{jet}} \cos \theta_{\text{LOS}})} \quad (4.20)$$

It is worth mentioning that the relativistic Doppler effect is observable even for a transversal direction of motion, i.e., for $\theta_{\text{LOS}} = 90^\circ$.

4.3.1.2 Boosting

Radiation from matter which moves at relativistic speeds $\beta \lesssim 1$ in an optically thin, isotropically emitting jet towards us is intensified to a flux density F_{obs} , compared to the flux density F_0 of a source resting relative to us, such that the ratio of the flux densities is

$$\frac{F_{\text{approach}}}{F_0} = D_{\text{approach}}^{k+\alpha} \quad (4.21)$$

where α is the spectral index of the emission, and k is a geometry parameter ($k = 2$ for a continuous jet, and $k = 3$ for discrete ejections). Correspondingly, receding matter will radiate with a lowered flux density

$$\frac{F_{\text{recede}}}{F_0} = D_{\text{recede}}^{k+\alpha} \quad (4.22)$$

Thus we have for the ratio of F_{approach} to F_{recede}

$$\frac{F_{\text{approach}}}{F_{\text{recede}}} = \left(\frac{1 + \beta_{\text{jet}} \cos \theta_{\text{LOS}}}{1 - \beta_{\text{jet}} \cos \theta_{\text{LOS}}} \right)^{k+\alpha} \quad (4.23)$$

which is plotted in Fig. 4.7 as a function of inclination angle θ_{LOS} for several ejection speeds β .

4.3.2 Production Mechanisms

Penrose & Floyd (1971) proposed that in principle it is possible to extract energy and angular momentum from a rotating BH, an idea which was advanced to explain the generation of electromagnetic fields and even outflows in the vicinity of BHs (Blandford & Znajek 1977; Blandford & Payne 1982). One of the most promising models to explain the production of jets from a magnetized accretion disk is the magneto-hydrodynamic model.

4.3.2.1 The Magneto-Hydrodynamic Model

In the idealized magneto-hydrodynamic (MHD) model as primarily presented by Blandford & Payne (1982) it is assumed that a highly conducting accretion disk is threaded with large scale poloidal magnetic field lines which are “frozen” into the disk matter. As the plasma cannot flow across the field lines, it is forced to move like a bead sliding on a rigid wire. In case the angle between the magnetic field lines and the disk plane is $< 60^\circ$, plasma can be catapulted centrifugally out from the disk. Due

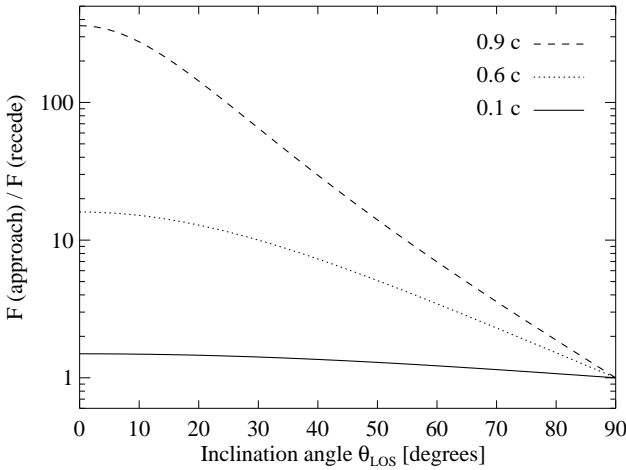


Figure 4.7: The effect of Doppler boosting for two symmetric discrete ejections at velocities $\beta = 0.9, 0.6,$ and 0.1 as a function of inclination angle θ_{LOS} : For $\theta_{\text{LOS}} = 90^\circ$, the ratio of F_{approach} to F_{recede} is always 1, whereas at smaller inclinations the Doppler boosting significantly enhances the ratio, particularly in the highly relativistic regime.

to the differential rotation of the AD, the field lines are wound up around the rotation axis, forming a twisted helical coil (Fig. 4.8). Far from the disk the expelled matter trapped in the field coil gets pinched towards the rotation axis by a magnetic hoop stress which is finally collimating the outflow to a jet (Meier et al. 2001). As angular momentum is lost with the outflow, thus allowing disk material to accrete onto the central compact object, the jet power mechanism is supplied with more released energy and a self-sustaining process is triggered.

The configuration of the resulting jet depends on the launching conditions like form and strength of the initial magnetic field or density and rotation rate of the AD, explaining the wealth of different forms of jet appearance. Generally, the MHD model is applicable to a variety of jet sources, like AGN, MQs, supernovae, and gamma-ray bursts (Meier et al. 2001).

According to Blandford & Znajek (1977) and Livio et al. (1999) the MHD jet power, L_{MHD} , and the scale-height of the disk H (cf. eq. (1.7)) are related as

$$L_{\text{MHD}} \propto H^2 \quad (4.24)$$

From this it is clear that the power of a jet from a thin disk will be significantly smaller than that from a thick disk. This result is impressively mirrored by the radio behavior of MQs. In the soft state, the thin α -disk reaches in until the BH and the radio

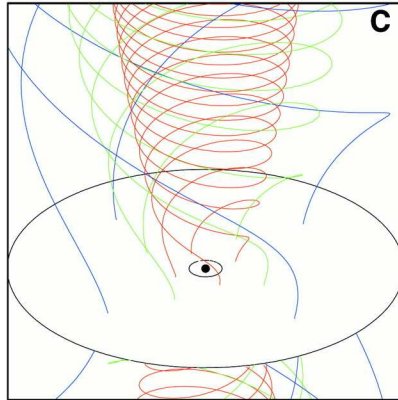


Figure 4.8: Magnetic field lines anchored in the accreted matter orbiting a central BH form a rotating helical coil which drives the trapped plasma outwards (Meier et al. 2001, Fig. 4).

emission is suppressed or even totally quenched, contrary to the hard state, which is associated with a geometrically thick accretion disk corona or a blown-up ADAF region, respectively, displaying significant radio emission.

Another parameter controlling the power and speed of a jet is the spin of the BH, which has been confirmed by simulations (see, e.g., Koide et al. 2000). In the case of a Kerr BH (Table 1.1), additional rotational energy needed for the generation of jets is supplied from the BH spin, resulting in higher jet velocities compared to a Schwarzschild BH (Meier et al. 2001). This conclusion has led to the assumption that all BHs which have a jet are fast rotating BHs, the so-called spin paradigm (Meier et al. 2001; Nowak 2003).

4.3.2.2 The Conical Jet Model

Motivated by the jet structure of SS 433, a conical jet model was developed to explain the synchrotron radio emission from XRBs (Hjellming & Johnston 1988). It assumes a twin jet which is formed by collimated conical sheaths of adiabatically expanding relativistic plasma. Connected to previous results of Shklovskii (1960) and van der Laan (1962) (see section 4.1.3), the concept of conical jets is capable to explain the radio characteristics both of stable quiescent sources like Cyg X-1 and of periodic emitters.

The very flat/inverted spectra of several BH XRBs, amongst them Cygnus X-1 (Fig. 4.11), do not show any turnover at higher frequencies as observed in AGN and as expected within the framework of synchrotron radiation (cf. Fig. 4.2). This was

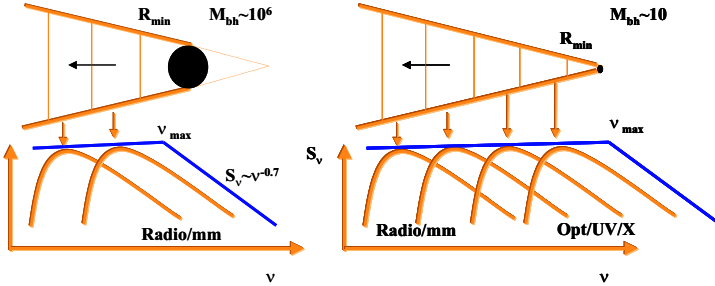


Figure 4.9: The conical jet model explains the flat spectrum with turnover frequency ν_{\max} as a spectral superposition from the different emission sections. The smallest jet scale determines the highest observed frequency. The scaledown of AGN jets to the size of MQs will lead to a corresponding shift of the maximum synchrotron frequencies from the radio/mm regime up to the optical/UV/X-ray bands (Falcke et al. 2002, Fig. 1).

interpreted as a scaling effect (Falcke et al. 2002): The jet is considered the source of flat spectrum synchrotron radiation resulting from the superposition of all contributions from various emission sections within the jet. The theory of the conical jet model predicts that the smallest physical scales within the jet will determine the highest frequency of these contributions: $\text{size} \propto 1/\nu$ (Falcke et al. 2002, and references therein). As in a GBHC the smallest jet scale is a factor of 10^6 – 10^9 smaller than in AGN, the synchrotron radiation observed from their jets should scale up and reach until the X-ray region (Fig. 4.9).

For slowed expansion into a surrounding medium of constant density, and if the jet material is continuously ejected, a power-law energy spectrum of radiating particles with distribution index $p = 3.14$ results in a radio spectrum with $\alpha = 0$, thus explains the flat-spectrum of Cyg X-1, like of many other BH XRBs. Additionally, it provides for flaring events by adding spherically expanding, independently evolving plasmoid “bubbles” in the case the pressure of the relativistic electrons dominates.

4.3.3 The Jet of Cygnus X-1

The rareness of radio flares with Cyg X-1 has forwarded the assumption that this source maintains a continuous jets rather than multiple plasmion ejection. Several observations detected a radio-emitting structure spatially extending ≈ 15 mas from the core of Cyg X-1 (Stirling et al. 1998; Spencer et al. 2001; Stirling et al. 2001). A clear picture of a collimated outflow has actually been resolved by VLBA observations (Fig 4.10) which show that a significant fraction of the 8.4 GHz flux is resolved. The jet emission is relatively smooth and does not show the knots and blobs seen, e.g., in

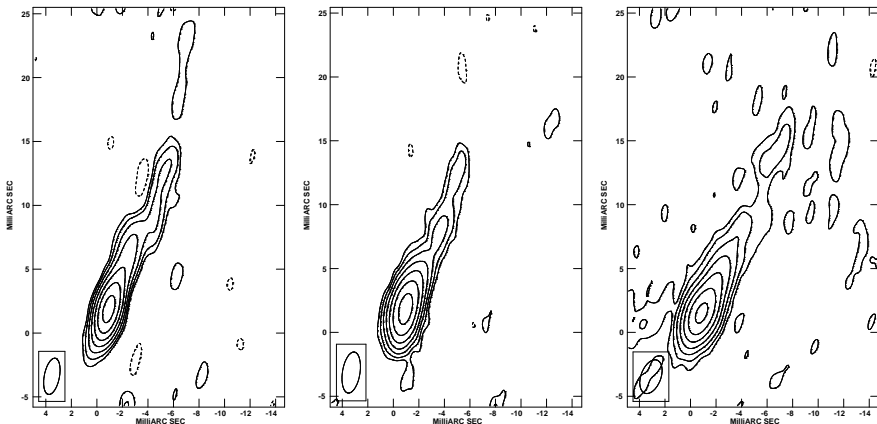


Figure 4.10: VLBA/VLA images of Cyg X-1 at 8.4 GHz, taken on (from left to right) 1998 August 10, 12, and 14, respectively (Stirling et al. 2001, Fig. 2). The contouring represents factors of 2, the lowest contour being at 0.1 mJy. Solid contours are at positive flux densities, dashed contours at -0.1 mJy.

GRS1915+105. The radio emission displays a flat spectrum through the radio–mm regimes (Fig. 4.11) with spectral index close to zero ($|\alpha| < 0.1$ between 2 and 15 GHz; Pooley et al. 1999; Fender et al. 2000), which has been modeled as slowed expansion in a continuous jet (section 4.3.2.2).

The linear scale of the outflow is of the order

$$l_{\text{VLBA}} \approx 15 \text{ mas} \approx 5 \times 10^{14} \text{ cm} \left(\frac{D_{\text{CygX1}}}{2 \text{ kpc}} \right) \quad (4.25)$$

where $D_{\text{CygX1}} \approx 2$ kpc is the distance to Cyg X-1.

The observed lower limit on the jet-to-counterjet brightness ratio δ is (Stirling et al. 2001)

$$\delta \equiv \frac{F_{\text{approach}}}{F_{\text{recede}}} \gtrsim 6 \quad (4.26)$$

where F_{approach} and F_{recede} are the radio flux from the approaching and receding jet, respectively (section 4.3.1, Fig. 4.7). This constrains the jet inclination to be (S. Heinz, private communication)

$$\cos(\theta_{\text{LOS}}) \geq \frac{\delta^{1/(k+\alpha)} - 1}{\delta^{1/(k+\alpha)} + 1} \approx 0.42 \quad (4.27)$$

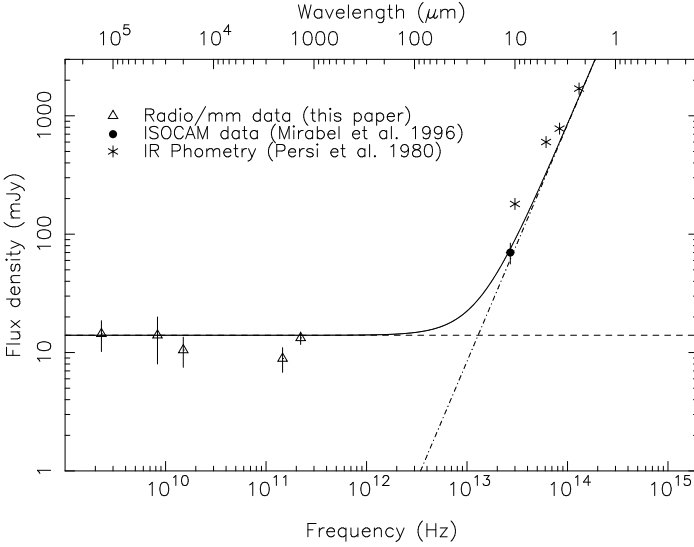


Figure 4.11: Broadband observations of Cyg X-1 show a flat spectrum in the range from radio (3 datapoints below 10^{11} Hz) to mm (2 datapoints between 10^{11} Hz and 10^{12} Hz) wavelengths, with no indication of a cutoff at high frequencies (Fender et al. 2000, Fig. 3).

and, for a given viewing angle θ_{LOS} , it constrains the jet velocity to be

$$\beta_{\text{jet}} = \frac{1}{\cos(\theta_{\text{LOS}})} \frac{\delta^{1/(k+\alpha)} - 1}{\delta^{1/(k+\alpha)} + 1} \geq \frac{\delta^{1/(k+\alpha)} - 1}{\delta^{1/(k+\alpha)} + 1} \quad (4.28)$$

where α is the spectral index and k is a parameter which is related to the geometry of the ejections (see section 4.3.1). Since the jet spectrum is observed to be flat, and since the emission is relatively steady, $\alpha = 0$ and $k = 2$ seem to be fiducial values. Then a lower limit to the jet velocity of $\beta > 0.6$ is derived (Stirling et al. 2001).

4.4 Models of Radio–X-ray Correlations

For radio–X-ray correlations to be produced, radio and X-ray emitting regions have to be excited by a common mechanism, the most natural being variations in the mass accretion rate \dot{m} . As theory suggests, the bulk of X-ray emission takes place in the vicinity of the BH, whereas radiation at radio wavelengths is produced by a process connected to outflow regions at ample distance from the compact object. The idea that the radio emission could stem also from the corona has been disproved (Wilms et al.

1999; Brocksopp et al. 1999a; Fender & Hendry 2000). Under these circumstances a varying \dot{m} will be mirrored in the X-rays first and then, with a time lag depending on the corresponding travel time of matter, in the radio emission from the jet.

4.4.1 The Coronal Outflow Model

Observations show that radio emission from BH XRBs is associated with the hard state. Although it is not clear whether the corona or the ADAF concept is more realistic, the following model favors the first alternative. In this case, a good part of the energy released during the accretion of matter by a BH is observed as hard X-ray emission from the corona. In this picture, a straightforward mechanism to produce radio–X-ray correlations in the hard state is realized when a fraction η of the power released into a magnetic corona is used to energize a jet.

Merloni & Fabian (2002) define the power release from the corona, the corona luminosity L_c , as a fraction f of the total power release of the accretion disk–corona system, L_{tot} ,

$$L_c = fL_{\text{tot}} = f\dot{m}L_{\text{Edd}} \quad (4.29)$$

where \dot{m} is the mass accretion rate in units of the Eddington one for a non-rotating black hole, $\dot{m} = 0.08\dot{M}c^2/L_{\text{Edd}}$ (Merloni & Fabian 2001), and L_{Edd} is the Eddington limit (cf. eq. (1.10)). Advocating a corona as an “ideal launching platform for powerful jets” (Merloni & Fabian 2002) either by MHD or thermally driven processes, they show that in the jet power, $L_{\text{jet}} = \eta L_c$, a substantial fraction of the total luminosity is contained. Farther from its launching site, the jet will produce radio emission, thus giving rise to a correlation with the coronal X-rays.

4.4.2 The Depletion Model

As mentioned in section 4.2.2.1, GRS 1915+105 in the spectrally hard, power-law dominated C state can enter X-ray variability classes where radio oscillations occur with a period of about 12 to 60 min (see, however, Nayakshin et al. 2000). This unsteady behavior has been explained as cyclic outflow of single blobs, i.e., transient jets. Each jet is formed by the depletion of the inner AD, then goes off and sets in again when the disk has been refilled with plasma (Mirabel & Rodríguez 1999). The amount of depletion in the inner disk, observable as X-ray dips, is connected to the rate of ejection of radio-emitting clouds (Mirabel et al. 1998).

The similarities of the outburst pattern with dwarf novae were the starting point of interpreting the sudden transitions between high and low luminosity in X-rays as a cycle of depleting and refilling the AD (Belloni et al. 1997a,b). Triggered by a viscous-thermal instability, a heating wave causes inner parts of the disk to fall to the central object, causing a decrease of X-ray luminosity as this hot plasma gets lost. The refill of the depleted regions takes place during a quiescent state. When the accreted

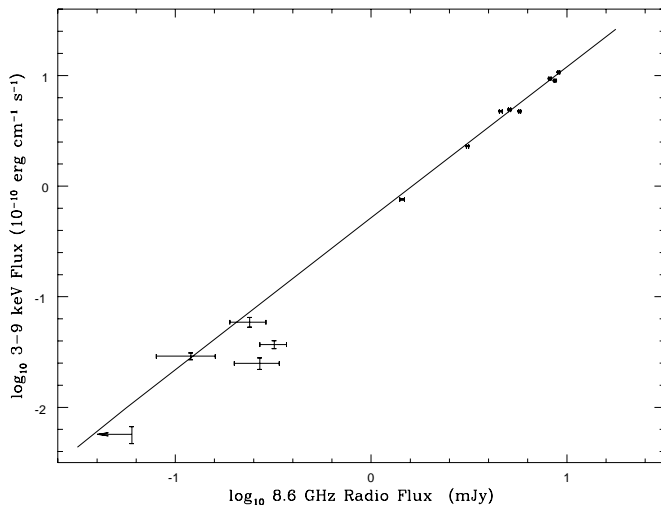


Figure 4.12: The jet model is capable to fit the observed radio–X-ray correlation of GX 339–4 only by changing the input power into the jet (Markoff et al. 2003, Fig. 6).

matter to some extent is redirected and expelled as an outflow, contributing to radio emission via synchrotron radiation, this model can account for correlations between X-rays and radio luminosity on time scales of minutes to hours, depending on the travel time of plasma from the inner accretion disk to the radio emitting regions in the outer jet.

4.4.3 The Unifying Jet Model

Radio–X-ray correlations are a natural outcome of the jet model (Falcke & Markoff 2000; Markoff et al. 2001, and references therein; cf. section 1.5.3), as both X-ray and radio emission are assumed to be produced by synchrotron processes (synchrotron radiation, synchrotron self-Compton) in the same medium, namely the jet (cf. Blazar jets).

As mentioned in section 4.2.1, GX 339–4, among other BH XRBs, shows radio–X-ray correlations over a wide flux range. The relation between radio and X-ray, $F_{\text{radio}} \propto F_{\text{X}}^{0.7}$, as advocated by Gallo et al. (2003) (section 4.2.1) can be reproduced from analytical predictions of the jet model by the variation of only one main parameter, the power input Q_{jet} (section 1.5.3) into the jet which is assumed to be proportional to the accretion rate (Markoff et al. 2003) (Fig. 4.12). Thus the model assumption that

changes of the mass accretion rate modulate the input of power into the jet and consequently the X-ray and radio emission from there seems plausible.

In combination with the assumed ADAF, the jet model has been developed as a radiatively inefficient jet dominated accretion flow (JDFAF) (Falcke et al. 2004). Its major merit is the merging of X-ray and radio/IR properties into a single model by unifying the concepts of jet and corona (see, however, Zdziarski et al. 2003; Poutanen & Zdziarski 2003).

Radio–X-ray Correlations of Cygnus X-1

As this chapter is based on two publications (Gleissner et al. 2004a,b), it adopts the characteristic publication style. Section 5.4 and parts of section 5.5 were extracted from a previous version of Gleissner et al. (2004b) and contain results that were kindly contributed by S. Markoff and S. Heinz at MIT, Center for Space Research.

5.1 Observations and Data Analysis

For the studies presented here, we used X-ray data from the Rossi X-ray Timing Explorer (*RXTE*) and radio data from the Ryle Telescope. In Fig. 5.1a the radio flux of Cyg X-1 is displayed, binned to a resolution of 5.6 days, the orbital period of Cyg X-1 (Brocksopp et al. 1999a). All flux points are assigned to symbols according to their state, following a state definition which is based on the spectral photon index and the time lag between soft and hard photons (Benlloch 2003; Benlloch et al. 2004), amended by the criterion that a soft state must have a radio flux ≤ 3 mJy. This definition distinguishes three states: The canonical hard and soft states, as well as the failed state transitions (FST) (Pottschmidt et al. 2000), which comprise all observations which do not fall into either of the other two states.

The analyzed data span the time from 1999 until the beginning of 2003, covering our *RXTE* monitoring programs P40099 (1999), P50110 (2000–2002), and P60090 (2002–2003) (Fig. 5.1c and d). The analyses of radio–X-ray correlations were performed using the *Standard2f* lightcurves with a resolution of 16 s from the *PCA* data using the data analysis software *HEASOFT*, Version 5.2. Also high energy data from the *HEXTE* with a time resolution of 1 s were extracted.

In our scheduling of the monitoring of Cyg X-1 in radio and X-ray bands, we strived for strictly simultaneous observation times. The observations which are analyzed here are marked with the dots in Fig. 5.1b. Due to the *RXTE* orbit, the X-ray data of each observation are composed of several short lightcurve segments of a typical duration of ~ 0.5 h, while the radio data generally consist of a longer continuous lightcurve of several hours. Fig. 5.2 shows simultaneous lightcurves of X-ray and

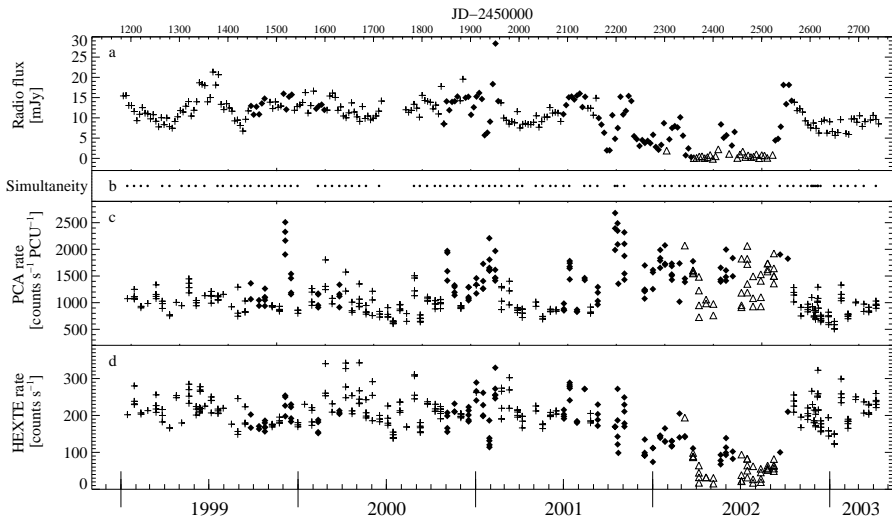


Figure 5.1: Cyg X-1: **a)** Mean Ryle Telescope radio flux, rebinned to a resolution of 5.6 days, the orbital period of Cyg X-1. **b)** Times of simultaneous radio–X-ray observations with Ryle Telescope and *RXTE*. **c)** Mean *RXTE* PCA count rate. **d)** Mean *RXTE* HEXTE count rate. Hard states are indicated by crosses, soft states by triangles, and failed state transitions (FST) by filled diamonds (see text for state definition).

radio of the exemplary observation on 1999 February 25.

For the analysis, the radio and X-ray lightcurves of all simultaneous observations were rebinned to a time resolution of 32 s. Only lightcurves with a length of at least 15 min were considered. We then applied the Savitzky & Golay (1964) smoothing filter, i.e., a least squares polynomial fit which can be used to smooth a noisy signal (Press et al. 1992). After this smoothing, every single continuous X-ray lightcurve segment and radio lightcurve within a time lag of ± 10 h to each other was cross-correlated. The cross-correlation coefficient is calculated only when the overlap of the radio and X-ray lightcurves is more than 15 minutes. Thus we find the maximum cross-correlation coefficient, MCC, and the corresponding time lag for each radio and X-ray lightcurve pair. Depending on the data sampling and the length of the lightcurves, the maximum possible relative shift between the radio and X-ray lightcurves is about ± 10 h, in most cases, however, the maximum shift is much less. Fig. 5.3 gives the distribution of the relative shifts between the radio and PCA X-ray lightcurves which are covered by our calculations for Cygnus X-1. A negative shift means that the X-rays precede the radio. As the bulk of observations covers only a relative shift of ~ 5 h, our analysis is significant on time scales from minutes to ~ 5 h.

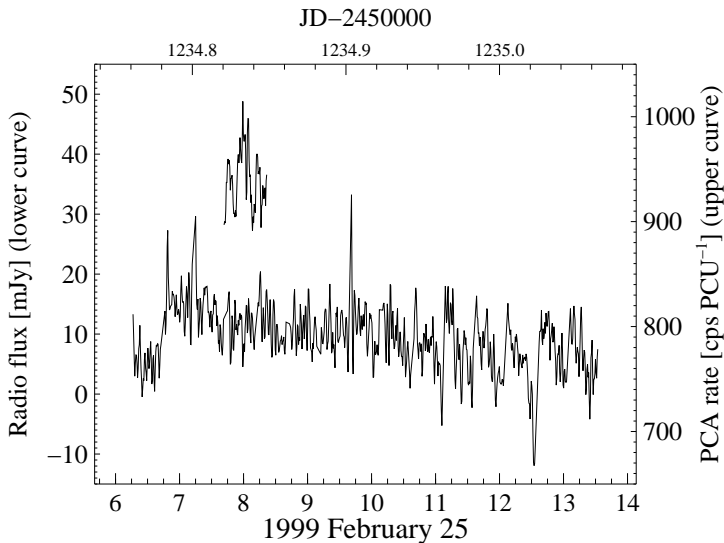


Figure 5.2: Cyg X-1: Observation on 1999 February 25 with *PCA* X-ray and radio data re-binned to a time resolution of 32 s and smoothed, showing uninterrupted segments of X-ray (upper curve) and radio (lower curve) lightcurves.

Due to the *PCA* dead time after processing an event, the detected X-ray count rate is diminished with respect to the actual count rate. To test whether a correction for this dead time effect was necessary we followed the description given by the *RXTE* Guest Observer Facility (GOF), using the Very Large Event (VLE) dead times as given by Jernigan et al. (2000). We verified that the influence of dead time correction of the *PCA* lightcurves on the resulting MCC and time lag is small: when calculating the cross-correlation with and without dead time correction, the results of only 8 observations out of 87 had significantly changed. As due to the failure of the propane layer since 2000 May 12 it is not possible to compute a reliable dead time correction (section 1.6.2), we have chosen not to apply the dead time correction in our X-ray lightcurves.

5.2 Sensitivity of the Procedure: Application to *GRS 1915+105*

If a radio and an X-ray lightcurve are truly correlated, the corresponding MCC will have an absolute value close to 1. Due to statistical reasons, however, there is a finite probability of finding a large absolute value of MCC even for two random lightcurves,

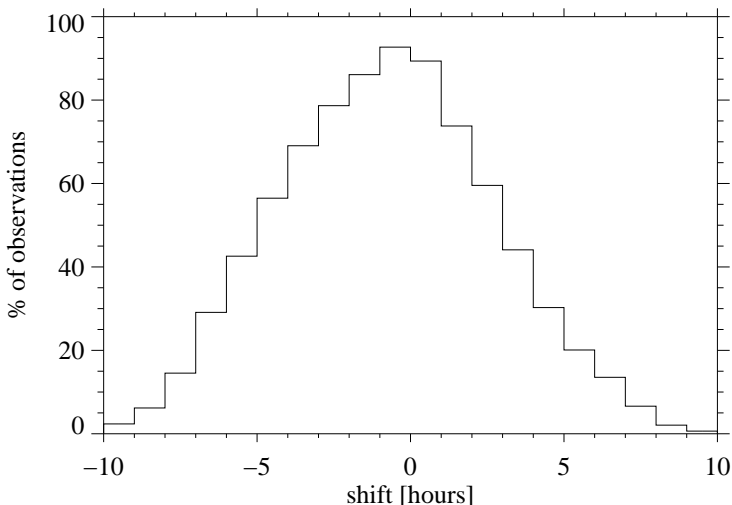


Figure 5.3: Cyg X-1: Histogram of the relative shift between the radio and X-ray lightcurves that is covered by the used cross-correlation calculations for the 301 *PCA* lightcurve segments. Only in few cases the maximum relative shift extends up to 10 h, limiting the significance of our analysis to time scales of less than ~ 5 h.

e.g., white noise lightcurves. For a large sample of simultaneous radio and X-ray lightcurve pairs, however, the distribution functions of MCCs computed for pairs with random correlations and computed for pairs with a real correlation will be different. By comparing the MCC distributions computed from white noise lightcurves with those from the real data, it is thus possible to test for the presence of a correlation between the radio and the X-rays in a statistical sense. In this section we show how such comparisons are performed. Before working with the data from Cyg X-1, we first test the method outlined above with data from a source where a multitude of observations indicate the presence of a radio–X-ray correlation.

The actual radio–X-ray correlations of GRS 1915+105 turn it into an appropriate source to serve as a benchmark for the cross-correlation procedure used here (see section 4.2.2). For this benchmark, we used a set of 120 simultaneous radio–X-ray lightcurve segments of GRS 1915+105, taken from the data base of Klein-Wolt et al. (2002), and applied the same cross-correlation procedure as described in section 5.1. The data of GRS 1915+105 were taken with *RXTE PCA* and the Ryle Telescope.

The one-to-one relation between an X-ray dip and a subsequent oscillation peak in the radio emission of GRS 1915+105, that was mentioned in section 4.2.2, is equiv-

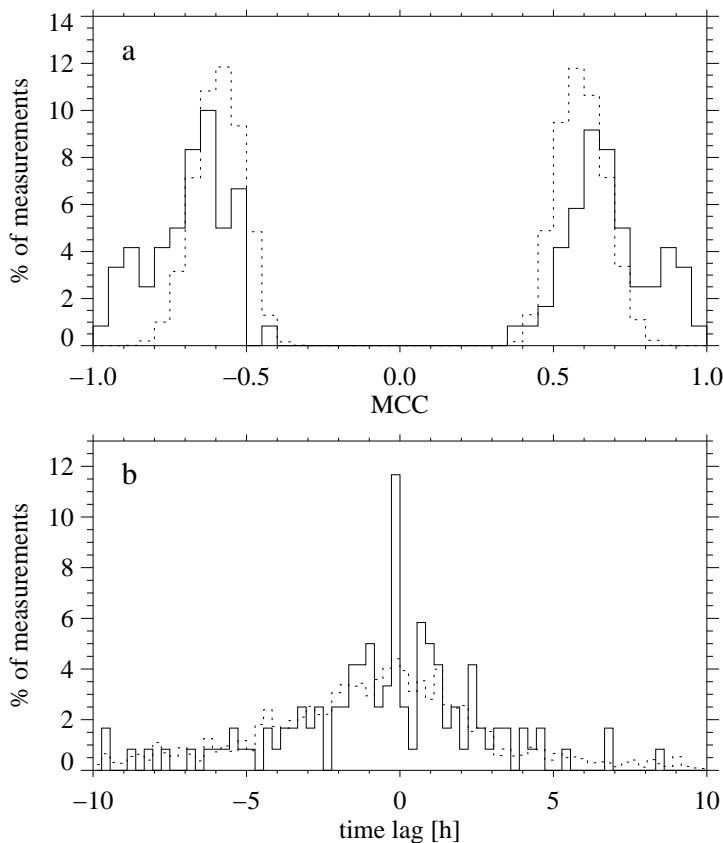


Figure 5.4: GRS 1915+105: Histograms of **a**) the distribution of MCC and **b**) the distribution of time lags for observed data (solid line) and simulated white noise data (dotted line). The histograms takes into account 120 separate lightcurve pairs. The MCC have been binned to 40 bins with bin widths of 0.05 from -1 to $+1$, the time lags have been binned to 72 bins with bin widths of 1000 s from -10 h to $+10$ h. Original lightcurves have been binned to 32 s and have been smoothed by the Savitzky-Golay filter.

alent to an anti-correlation with negative MCC close to -1 . When the shift of the X-ray lightcurve relative to the radio lightcurve is continued for $P_{\text{osc}}/2$, i.e., until the X-ray dip coincides with the subsequent oscillation valley of the radio emission, we obtain a positive MCC close to $+1$. As in the used cross-correlation procedure the absolute maximum value of the cross-correlation coefficient is determined, due to the

Table 5.1: Characteristics of the Kolmogorov-Smirnov test for two samples: test statistic D_{obs} for observed and standard white noise distribution, and Probability P for $D_{\text{test}} \geq D_{\text{obs}}$.

	a) GRS 1915+105		b) Cygnus X-1	
	MCC	time lag	MCC	time lag
D_{obs}	0.168	0.097	0.058	0.056
$P[\%]$	0.1	1.7	13.6	14.4

noise in MCC in about half of all cases this happens to be the anti-correlation of the one-to-one relation, in the remaining half it is the positive correlation when the shift has been continued for $P_{\text{osc}}/2$. Thus, both negative and positive MCCs close to ± 1 indicate the same features, i.e., the searched radio–X-ray correlations of Klein-Wolt et al. (2002). We did not correct for this periodical effect in the histograms of MCC, but accounted for it when determining the corresponding time lag.

Fig. 5.4a compares the histogram $h_{\text{obs}}(\text{MCC})$ of the MCC for the available data set, i.e., 120 simultaneous radio and X-ray observations of GRS 1915+105 (solid line) with the histogram $h_{\text{sim}}(\text{MCC})$ of MCC from 1000 simulated white noise data sets (dotted line). In this simulation we created random white noise lightcurves for the radio and X-ray data with the same mean value, standard deviation, and sampling as the observed radio and X-ray lightcurves. Then we cross-correlated these simulated lightcurves exactly the way we did with the observed ones and determined the histogram of the corresponding MCC. For the whole data set, i.e., the 120 simultaneous radio and X-ray observations, we ran the simulation 1000 times in order to achieve a sufficient statistical significance. Using a similar technique, we compared the histogram of the observed time lags (determined from the MCC) with the distribution of the time lags obtained from the Monte Carlo simulations (Fig. 5.4b).

Fig. 5.4 shows that both the MCC and the time lag distribution for the observed data of GRS 1915+105 is considerably different from the corresponding white noise distribution. We use the Kolmogorov-Smirnov test statistic D (Keeping 1962) to quantify the difference of two distributions (see Table 5.1a). From Fig. 5.4a we determine D_{obs} , giving us a measure of the difference between the observed distribution of the data set and a standard white noise distribution, obtained by averaging over 1000 simulated white noise data sets. The Kolmogorov-Smirnov test allows the determination of the probability P that the difference D_{test} between a single simulated white noise data set and the standard white noise distribution is equal to or greater than D_{obs} . If P is sufficiently small, the null hypothesis H_0 that the observed and the simulated distributions have been drawn from the same underlying distribution function is to be rejected. Carrying out this analysis for both the MCC and the lag distributions, we find that the null hypothesis is to be rejected at the 0.1% level for the MCC, and at the

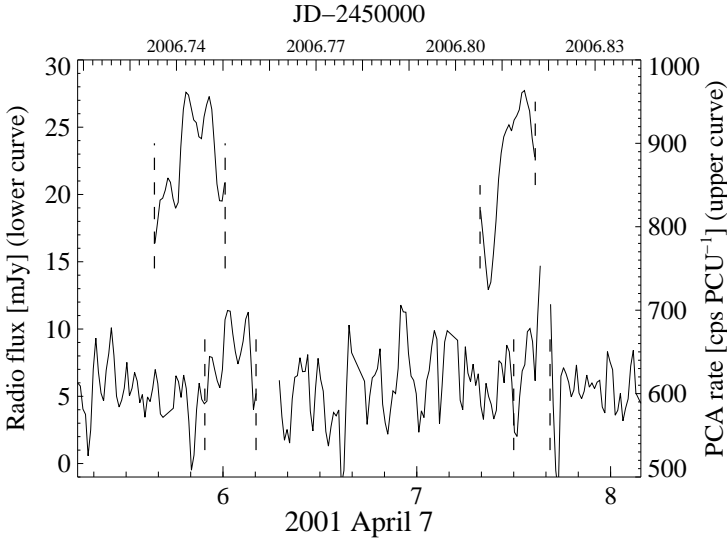


Figure 5.5: Cyg X-1: Joint radio–X-ray lightcurves of 2001 April 7, binned to a resolution of 48 s, showing a possible delay in the radio response to the X-ray variability (MCC is 0.75). Time on the x -axis is in hours.

1.7% level for the time lags (see Table 5.1a).

As expected, the radio–X-ray correlations in GRS 1915+105 which were examined by Klein-Wolt et al. (2002) are reflected by the significant fraction of MCCs with absolute values close to 1. This means that our procedure is capable of finding radio–X-ray correlations in a data set. Furthermore, the time lags that correspond to the MCC distribution for GRS 1915+105 appear as a clearly increased number of observations with time lag in the bin $[-1000 \text{ s}, 0 \text{ s}]$, consistent with earlier observations (Klein-Wolt et al. 2002).

5.3 Results for Cygnus X-1

5.3.1 Short Term Correlations

Checking the simultaneous lightcurves of Cyg X-1 by eye reveals several observations that show a similar pattern in the X-ray and radio lightcurve, with a delay in the radio response in the range of minutes. The time delays between X-ray and radio are not constant in all observations but vary from a few minutes to tens of minutes. Fig. 5.5 shows the most convincing of these observations. The first X-ray lightcurve segment

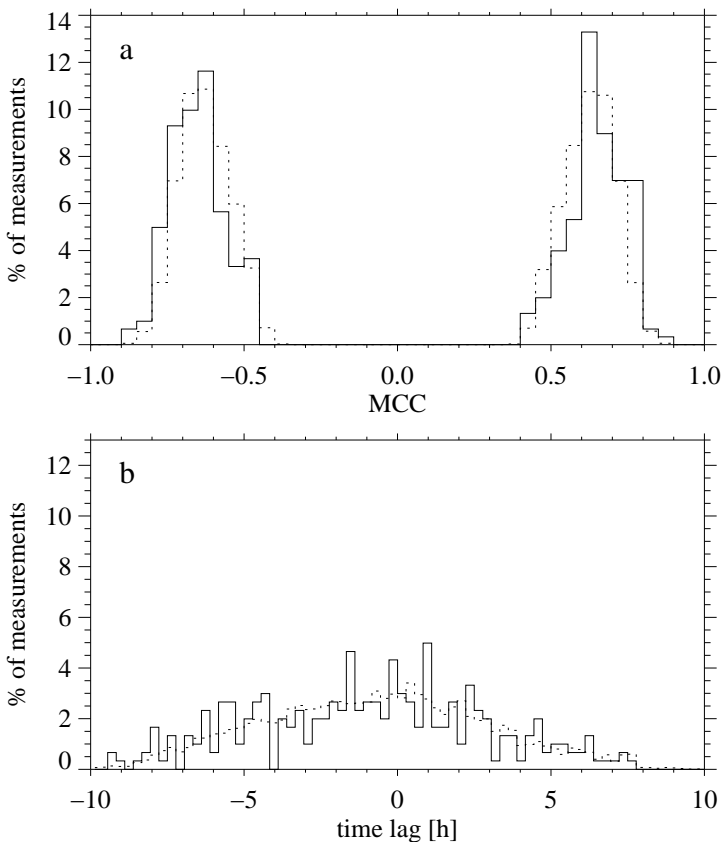


Figure 5.6: Cyg X-1: Histograms of **a**) the distribution of MCC and **b**) the distribution of time lags for observed data (solid line) and simulated white noise data (dotted line). The histograms takes into account 301 separate lightcurve pairs. The MCC have been binned to 40 bins with bin widths of 0.05 from -1 to $+1$, the time lags have been binned to 72 bins with bin widths of 1000 s from -10 h to $+10$ h. Original lightcurves have been binned to 32 s and have been smoothed by the Savitzky-Golay filter.

leads the radio echo by ~ 13 min whereas the second X-ray segment lies not more than ~ 8 min before the corresponding radio pattern.

To systematically investigate these apparent correlations we applied the cross-correlation procedure outlined in section 5.2. In Fig. 5.6a we compare the histogram $h_{\text{obs}}(\text{MCC})$ of the available data set, i.e., 301 simultaneous radio and PCA X-ray ob-

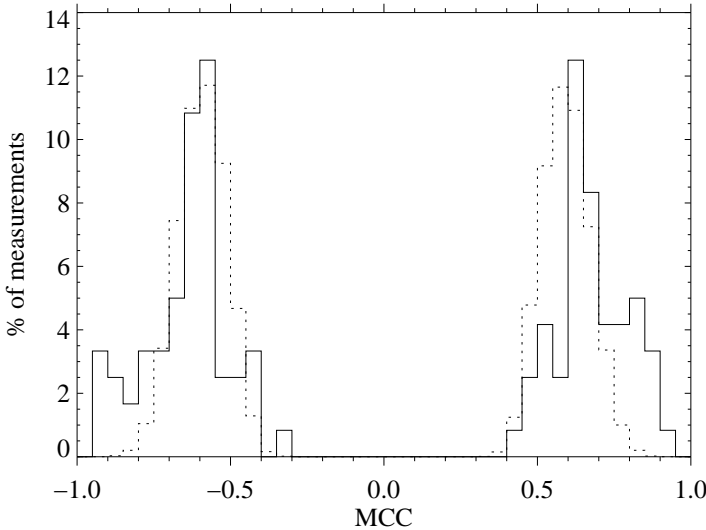


Figure 5.7: GRS 1915+105: Histogram of the distribution of MCC for observed data, rescaled to the S/N -level of Cyg X-1 (solid line) and simulated *white noise* data (dotted line). The histogram takes into account 120 separate lightcurve pairs. Original data have been binned to 32 s and has been smoothed by the Savitzky-Golay filter.

servations of Cyg X-1 with $h_{\text{sim}}(\text{MCC})$ from 1000 white noise simulations of this data set. The Kolmogorov-Smirnov test shows that the two histograms bear significant similarities such that the null hypothesis of identical distributions is to be accepted (Table 5.1b). We conclude that the MCC distribution of the observed and the simulated lightcurves are similar. The same conclusion is drawn from a comparison of the distributions of the time lags (Fig. 5.6b and Table 5.1b). Unlike GRS 1915+105, the time lag distribution of Cyg X-1 does not show any distinctive features and is consistent with that of the white noise simulation. This leads us to the assumption that the similar patterns seen on short time scales in the X-ray and in the radio lightcurves are random events which are a natural outcome in white noise lightcurves.

5.3.2 Rescaling GRS 1915+105 to the Level of Cygnus X-1

Although more than 4 times closer to us, Cyg X-1 is relatively dim in X-ray and radio, compared to GRS 1915+105. The average *PCA* X-ray flux level of Cyg X-1 in the hard state is $\sim 1000 \text{ counts s}^{-1} \text{ PCU}^{-1}$, in the radio band it has a flux of $\sim 14 \text{ mJy}$. In the χ class state, which is thought to be associated with the canonical

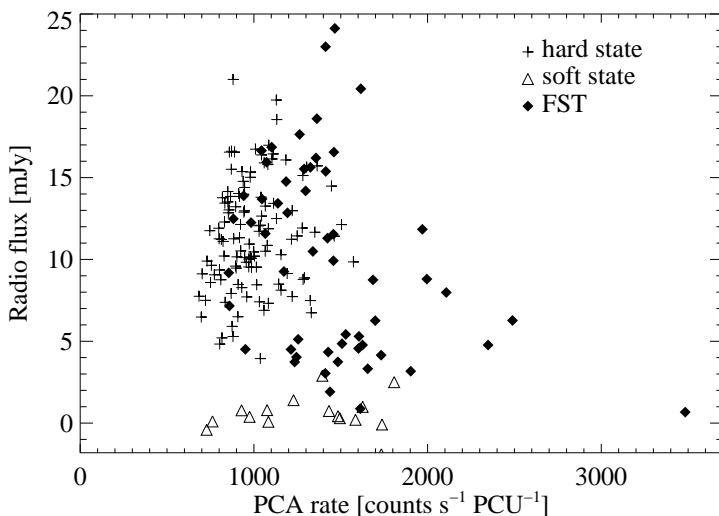


Figure 5.8: Cyg X-1: PCA X-ray and radio flux-flux plot for data from 1999 Jan 14 to 2003 Apr 06 with $0.25 \leq \Phi_{\text{orb}} \leq 0.75$, PCA channels 0–128 (mainly sensitive in the range ~ 2 –15 keV).

hard state of other BH candidates, GRS 1915+105 has an average X-ray flux level of $\sim 8000 \text{ counts s}^{-1} \text{ PCU}^{-1}$ and a 15 GHz (Ryle Telescope) radio flux of $\sim 40 \text{ mJy}$ (Klein-Wolt et al. 2002). This raises the question: is the negative result obtained in the previous section caused by the low signal to noise, S/N , level, or would our correlation procedure be able to find radio–X-ray correlations in Cyg X-1 if they were present the same way as in GRS 1915+105 but on the lower S/N level of Cyg X-1?

In order to answer this question we scaled the X-ray and radio lightcurves of GRS 1915+105 to the observed level for Cyg X-1, adding the appropriate amount of Gaussian noise. Fig. 5.7 shows that the MCC distribution of these rescaled lightcurves differs from that of the corresponding white noise simulation distribution, similarly to Fig. 5.4a. This result proves that our correlation procedure is sufficiently sensitive to detect any radio–X-ray correlations in Cyg X-1 if these are at the level of GRS 1915+105. We conclude that the negative result of section 5.3.1 is not caused by an insufficient signal to noise ratio.

5.3.3 Long Term Correlations

In this section long term correlations, i.e., on time scales from days to weeks and months are considered. As described in section 4.2, no clear correlation on long

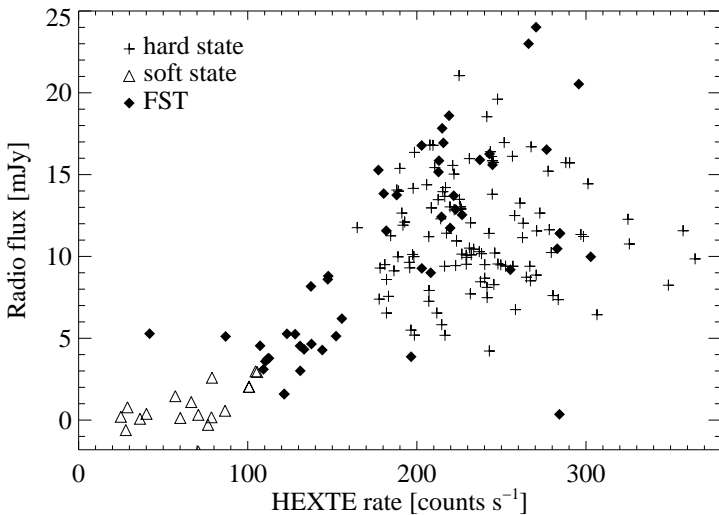


Figure 5.9: Cyg X-1: *HEXTE* X-ray and radio flux-flux plot for data from 1999 Jan 14 to 2003 Apr 06 with $0.25 \leq \Phi_{\text{orb}} \leq 0.75$, *HEXTE* channels 15–255 (~ 15 –255 keV).

term time scales between the radio emission and the *RXTE* *ASM* soft (2–10 keV) X-ray flux is found (Pooley et al. 1999; Brocksopp et al. 1999a). The availability of the pointed observations allows us to extend these studies to harder energies, using the data from the *PCA* (which is mainly sensitive below 15 keV) and the *HEXTE* (channels 15–255, sensitive above 15 keV). All observations from hard and soft states as well as from FST have been included (for state definition see section 5.1). To account for known orbital modulation (Brocksopp et al. 1999a,b, 2002), we limit the data set in orbital phase, Φ_{orb} , to observations with $0.25 \leq \Phi_{\text{orb}} \leq 0.75$.

Fig. 5.8 shows that no correlation between the soft X-rays from the *PCA* data and the radio exists. We note that this pattern is similar to that seen in GX 339–4 (Corbel et al. 2000). For the *HEXTE* band, above 15 keV, however, a long term correlation between the radio and the X-rays is evident, particularly for the FST (Fig. 5.9). Spearman rank correlation coefficients, r_s , have been calculated for the subplots of hard state and FST data points, and for all data points shown in Figs. 5.8 and 5.9, confirming this result (see Table 5.2).

In terms of Comptonization models, the > 15 keV band is dominated by Compton reflection and emission from the accretion disk corona, while an appreciable fraction of the soft X-rays can be due to the accretion disk. The correlation displayed in

Table 5.2: Spearman rank correlation coefficients, r_S , of plots in Figs. 5.8 and 5.9. The range of the correlation coefficient is $-1 \leq r_S \leq 1$, with a perfect correlation being indicated by $r_S = 1$ (Keeping 1962).

	Hard state	FST	All data points
Radio/PCA	0.17	-0.37	-0.16
Radio/HEXTE	0.05	0.67	0.50

Fig. 5.9 shows that the radio emission is directly linked to this hard component of the X-ray spectrum, which is present during the state transitions and the hard state, but not during the soft state, consistent with the earlier findings cited in section 4.2. The correlation is also remarkably similar to the correlation between the rms variability at > 15 keV and the *BATSE* hard X-ray flux discovered by Crary et al. (1996).

5.4 Estimating the Time Scale for Traversing the Jet

We can use the constraints of the radio observations (see 4.3.3) to set limits on the time delay between any event in the accretion disk that might alter the jet flux, and the time when the change in jet flux is observed. This limit on the time delay is simply given by the light travel time from the base of the jet to the photosphere, modulated by relativistic aberration.

Since the jet spectrum is flat (see 4.3.3), we conclude that the jet photosphere is located at about the projected distance, but somewhat closer in (since only a fraction of the flux is resolved). We will call this (projected) distance the photospheric radius, $l_{\text{phot}} \lesssim l_{\text{VLBA}}$. Any emission from well within the photospheric radius (where the jet becomes optically thin) will be strongly suppressed by synchrotron self-absorption.

Furthermore, the jet emission region is extended, with a projected size scale l_{emiss} comparable to, but again somewhat smaller than the photospheric radius, $l_{\text{emiss}} \lesssim l_{\text{phot}}$. For a given jet inclination θ_{LOS} , the deprojected size scale is then $r_{\text{emiss}} = l_{\text{emiss}} / \sin(\theta_{\text{LOS}})$. Therefore, any variability imprinted on the flow on size scales much smaller than this will be washed out and will not be observable. The PSD of the radio emission should therefore show a significant cutoff at frequencies above $\nu_c \gtrsim v_{\text{jet}} / r_{\text{emiss}} \approx \beta_{\text{jet}} c \sin(\theta_{\text{LOS}}) / l_{\text{phot}}$, where $\beta_{\text{jet}} = v_{\text{jet}} / c$ is the jet velocity.

Correcting for projection, the intrinsic photospheric radius r_{phot} is given by $r_{\text{phot}} = l_{\text{phot}} / \sin(\theta_{\text{LOS}})$. Using the limits from eq. (4.28), the travel time for any signal from

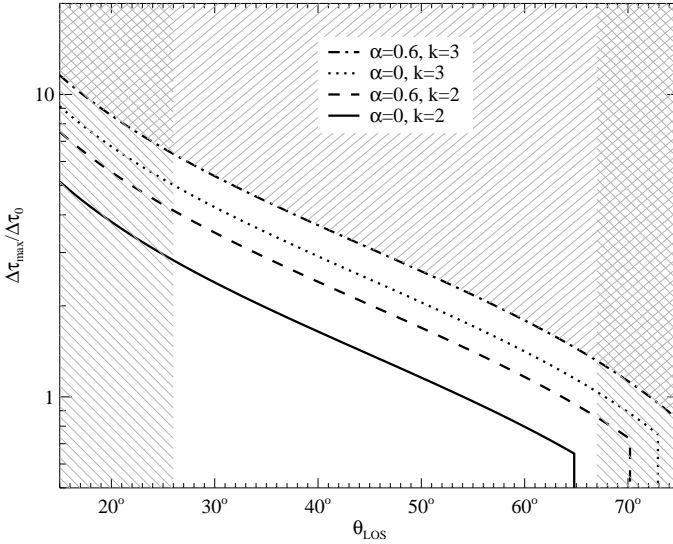


Figure 5.10: Maximum delay time $\Delta\tau_{\max}$ between the (X-ray) signal in the accretion disk and the (radio) emission in the jet as a function of angle θ_{LOS} between jet and line of sight. The delay time $\Delta\tau_{\max}$ is given in units of the light travel time $\Delta\tau_0$ over the observed ($\nu = 8.4$ GHz) jet length. For a jet of 15 mas at a distance of 2 kpc the light travel time $\Delta\tau_0$ is ~ 4.2 h. The lines denote from bottom to top: continuous jet with flat spectrum (most probable case), continuous jet with steep spectrum, discrete jet with flat spectrum, discrete jet with steep spectrum. (Diagram courtesy S. Heinz.)

the base of the jet to the photosphere will then be shorter than

$$\begin{aligned} \tau_{\text{phot}} &= \frac{1}{\beta_{\text{jet}} c \sin(\theta_{\text{LOS}})} \frac{l_{\text{phot}}}{\sin(\theta_{\text{LOS}})} \\ &\leq \frac{l_{\text{phot}}}{\sin(\theta_{\text{LOS}}) \frac{c}{\cos(\theta_{\text{LOS}})} \frac{\delta^{1/(k+\alpha)} - 1}{\delta^{1/(k+\alpha)} + 1}} \end{aligned} \quad (5.1)$$

Assuming that the signal traveling down the jet started in the accretion disk and is observable in the X-rays, we can now set a limit on the delay between the X-ray and

the radio signals reach the observer. This time delay is simply

$$\begin{aligned}\Delta\tau_{\text{obs}} &= \tau_{\text{phot}} - \frac{l_{\text{phot}} \cos(\theta_{\text{LOS}})}{c \sin(\theta_{\text{LOS}})} \\ &\leq \frac{l_{\text{phot}}}{c} \cot(\theta_{\text{LOS}}) \frac{2}{\delta^{1/(k+\alpha)} - 1} \equiv \Delta\tau_{\text{max}}.\end{aligned}\quad (5.2)$$

This is the upper limit on the time delay between the X-ray and radio signals imposed by the observed length of the jet and the observational limit on the jet-to-counterjet brightness ratio δ . We have plotted this upper limit for different values of k and α in Fig. 5.10, in units of the projected delay, $\Delta\tau_0 \equiv l_{\text{emiss}}/c$. We have also included limits on the inclination from the binary orbit. It is clear from this figure that $\Delta\tau_{\text{obs}}$ is not larger than a few times $\Delta\tau_0$. Note that this limit will not change significantly if the source of the X-ray is the jet and not the accretion disk, since the X-ray emission must be coming from well within the radio photospheric radius.

At frequencies higher than 8.4 GHz, the photosphere will be located somewhat further in, depending on the preferred jet model and geometry (e.g., Markoff et al. 2003; Heinz & Sunyaev 2003). Conservatively estimating that $l_{15.4\text{GHz}} \gtrsim l_{8.4\text{GHz}}/2$, we find that

$$\begin{aligned}\Delta\tau_0 &= \frac{l_{15.4\text{GHz}}}{c} \approx \frac{2.5 \times 10^{14} \text{ cm}}{c} \left(\frac{l_{15.4\text{GHz}}}{l_{8.4\text{GHz}}/2} \right) \left(\frac{D_{\text{CygX1}}}{2 \text{ kpc}} \right) \\ &\lesssim 3 \text{ h} \left(\frac{l_{15.4\text{GHz}}}{l_{8.4\text{GHz}}/2} \right) \left(\frac{D_{\text{CygX1}}}{2 \text{ kpc}} \right)\end{aligned}\quad (5.3)$$

This is an upper limit because the size of the photosphere is somewhat smaller than the measured 15 mas extent of the resolved jet. In summary, we do not expect that the observed time delay between any event happening at the base of the jet and its radio signature will be longer than about 10 hours (and it might be quite a bit shorter if the jet in Cyg X-1 is more relativistic than implied by the moderate brightness ratio limit of 6).

The variability cutoff imposed by the extent of the jet is similarly simple. Using the same limit on β_{jet} from eq. (4.28), it is

$$v_c \geq \frac{\tan(\theta_{\text{LOS}}) \delta^{1/(k+\alpha)} - 1}{\Delta\tau_0 \delta^{1/(k+\alpha)} + 1} \left(\frac{l_{\text{phot}}}{l_{\text{emiss}}} \right)\quad (5.4)$$

Finally, it should be noted that measurements of both $\Delta\tau_{\text{obs}}$ and v_c can be used to constrain the viewing angle of the source, the source velocity, and the size of the emission region.

5.5 Discussion

We have described the correlation between the radio and the X-ray emission of Cyg X-1 as seen with observations with the Ryle Telescope and the pointed instruments on *RXTE*. The major result of our analysis is that there is a correlation between the radio flux and the hard X-rays, particularly during intermediate states (flares, transitions, etc.), on time scales of days and weeks to months (Fig. 5.9), and no clear correlation between the soft X-rays and the radio flux on this time scale (Fig. 5.8). This result lends further support to the jet/disk concept (Brocksopp et al. 1999a; Fender 2002; Markoff et al. 2003). The overall connection of disk and jet has been affirmed in many observations, while the geometry at the base of the jet is still unclear. During the soft state, the radio emission is quenched and no jet is produced. In the hard state, the outflow from the accretion disk into the jet is relatively smooth, as represented by continuous radio emission over the length of the jet (Stirling et al. 2001), washing out smaller variability features. When the mass accretion rate in the disk varies significantly on time scales of several hours to days, this behavior is seen as X-ray flares and corresponding radio flares, resulting in radio–X-ray correlations during the flaring state.

On time scales of minutes to ~ 5 hours, no statistically significant correlation could be detected (Fig. 5.6). An explanation for this behavior could be that on time scales shorter than the propagation time between emission regions other factors, e.g., intervening turbulence, smooth out or distort any variability present.

We can roughly estimate the time scale for traversing the jet to place a limit on the correlation times. It was found in simultaneous broadband jet model fits to over 10 different BH candidates that the 15 GHz emission stems from distances $d = 10^{12}$ – 10^{14} cm out along the jet (Markoff et al. 2001, 2003, S. Markoff, private communication). Although the exact speed of the plasma in the jet is not known, we can set a reasonable range. From studies of the radio–X-ray correlation (Gallo et al. 2003) and state-transition luminosity (Maccarone 2003), the beaming near the base of jets should be necessarily low, with velocities $\beta \sim 0.2$ – 0.3 (Lorentz factor $\Gamma \sim 1.02$ – 1.05). The simplest free jet (no additional accelerating forces) would be expected to be accelerated by its longitudinal pressure gradient, so these values can safely be taken as a lower limit to the jet flow speed in its frame. There is still significant uncertainty as to whether the steady jets associated with the hard state can achieve the high bulk Lorentz factors associated with ballistic events in MQs (e.g., $\Gamma \sim 17$, $\beta \sim 1$, in V4641 Sgr, M. Rupen, private communication), but these can be used as the hard upper limit. The value of $\beta > 0.6$ as derived by Stirling et al. (2001) fits well into this range. Taking these numbers as guidelines and using the simple relation $t = d/\beta c$ without accounting for any additional effects like cooling, etc., one can estimate that the time scale for traveling from the base of the jet to the 15 GHz radio-producing

region will be between $10^{12} \text{ cm}/c \approx 33 \text{ s}$ and $10^{14} \text{ cm}/0.2c \approx 4.6 \text{ h}$. Depending on the inclination of the jet, the delay between the X-ray and the radio signals when they reach the observer will be in the same time range.

A similar time scale is also obtained from the radio imaging of the jet of Cyg X-1 (Stirling et al. 2001). We estimate the upper limit on the time delay between the X-ray and radio signals, $\Delta\tau_{\text{max}}$, imposed by the observed length of the jet and the observational limit on the jet-to-counterjet brightness ratio δ . Fig. 5.10 shows that for the most probable case of a continuous jet with flat spectrum (Fender et al. 2000) and $\theta_{\text{LOS}} \approx 35^\circ - 40^\circ$ (Herrero et al. 1995), $\Delta\tau_{\text{max}}$ amounts to $2.0 \times 4.2 \text{ h} \approx 8 \text{ h}$.

The VLBA observations provide a relatively reliable value of $d = 10^{14} \text{ cm}$ for the jet length. Thus, while there may be further uncertainty due to viscosity and other factors, we deem it safe to say that an absence of radio–X-ray correlations at time scales under 5–10 hours – as found for Cygnus X-1 – is a clear indication for a rather low jet speed. Taking into account the time range of $\Delta\tau_{\text{max}}$, a jet speed of $\beta \sim 0.6$, as deduced by Stirling et al. (2001), may indeed be a realistic estimate.

Given that no radio–X-ray correlations on short time scales like minutes to hours can be identified and that we indeed have correlations on time scales like days and months, it is consequent to look for correlations on intermediate time scales like hours to days. Probing these intermediate time scales will be the aim of an approved *RXTE* observation during 2004.

CHAPTER 6

Summary

In this thesis, observational data from Cygnus X-1 are analyzed which were taken by the X-ray satellite *RXTE* and at radio wavelengths by the Ryle Telescope at Cambridge (UK). Since its discovery, Cygnus X-1 has been attracting attention because there is convincing evidence that it is indeed a black hole and because it is a persistently bright source.

One of the key properties of black hole X-ray binaries like Cygnus X-1 is the highly variable X-ray emission, containing a wealth of information on the emitting system. Recently, it has been affirmed by the detection of a relativistic jet that Cygnus X-1 belongs to the subclass of microquasars. Microquasars are especially interesting as they seem to hold the key for the understanding of AGN.

Taking up these issues, the main results of this thesis derive from two parts, one dealing with the rms-flux relation of the X-ray emission, and the other concerning radio–X-ray correlations on short and long time scales.

6.1 *The rms-Flux Relation*

Before the work presented here, the linear relationship between the root mean square (rms) variability and flux (the “rms-flux relation”) had only been investigated for a few hard state observations of Cygnus X-1 and for single observations of an accreting neutron star (Uttley & McHardy 2001).

Here it was shown that the rms-flux relation of the X-ray lightcurves of Cygnus X-1 is valid throughout all states and energy ranges observed. The relation applies not only on short time scales $\gtrsim 5$ s but also on longer time scales of weeks to months.

The slope, k , of the linear rms-flux relation is steeper in the hard state than in the soft and intermediate states. Since k reflects the fractional rms variability, this result was anticipated (cf. section 1.4). The flux intercept, C , of the linear rms-flux relation is relatively constant and positive in the hard state but is diverse in the soft state: in the 1996 soft state, C is positive and slightly higher than during the hard state, in the atypical 2001/2002 “soft state”, C is decreasing relative to the hard state level,

with several observations showing a negative C . During “failed state transitions”, C is smaller than in the hard state, similar to the soft state behavior.

In the case of a positive C , these results argue for two lightcurve components, one variable component responsible for the linear rms-flux relation and one non-variable component with a constant count rate equal to C . If C is negative, the interpretation as a non-variable component would be unphysical, and a constant rms component is suggested instead.

In the hard state, the slope of the rms-flux relationship is correlated with its flux intercept, but the correlation is increasingly degenerate at higher values of k and C , forming a fan-like distribution in the k - C plane. The hidden parameter governing the degeneracy is the long term average flux, $\langle F \rangle$, and the k - C - $\langle F \rangle$ relation maps out a “fundamental plane” in the hard state.

6.2 Radio–X-ray Correlations

The main result of this part is that the radio–X-ray correlations of Cygnus X-1 on long times scales (= days to months) seem to break down on short times scales (= minutes to hours).

It was confirmed that correlations between the radio and the *hard* X-ray emission of Cygnus X-1 exist on time scales of weeks to months, particularly during intermediate states (flares, bursts, etc.). Similar, although less convincing conclusions had also been drawn with independent data by Pooley et al. (1999) and Brocksopp et al. (1999a). Correlations between the radio and the *soft* X-ray emission cannot be clearly established.

These results fit into the picture of a strong disk/jet connection during flaring states, with the jet formation significantly reduced or even stalled during the soft state.

Radio–X-ray correlations on short time scales as they have been proven for another BH XRB, GRS 1915+105, do not seem to be present in Cygnus X-1. Apparent radio–X-ray correlations in the lightcurves of Cygnus X-1 with a radio time lag of ~ 10 min with respect to the X-ray signal have been shown to be coincidental events of white noise statistics.

Taking into account the existence of radio–X-ray correlations on long times scales, the absence of radio–X-ray correlations on short times scales could be interpreted as a relatively long propagation time between the X-ray and the radio emission region. Any variability features on shorter time scales are distorted and washed out.

Within the framework of a jet model, these results argue for a rather low jet speed in Cygnus X-1, in agreement with independent work by Stirling et al. (2001).

6.3 Outlook

The *RXTE* monitoring of Cygnus X-1 is being continued. This ensures that the valuable data base of the temporal and spectral evolution of this prominent source is extended. In the past having focused on the study of the temporal properties, a coming task will be the spectral analysis of Cygnus X-1 with respect to its continuous evolution from the beginning of the monitoring, 1998, until today.

Likewise, the simultaneous observations with the Ryle Telescope will go on. The work on radio–X-ray correlations will be resumed by an approved *RXTE* observation later this year. Hopefully, it will show whether the radio–X-ray correlations, absent on time scales of a few hours, set in when proceeding to intermediate time scales of hours to days.

Following a general trend in the field of microquasars, the main attention in the coming years will be on linking the knowledge from different wavelength bands into one consistent picture.

Bibliography

- Alpar M.A., Shaham J., 1985, *Nature* 316, 239
- Baade W., Zwicky F., 1934, *Phys.Rev.* 45, 138
- Bachiller R., 1996, *ARA&A* 34, 111
- Bak P., Tang C., Wiesenfeld K., 1988, *Phys. Rev. A* 38, 364
- Balbus S.A., Hawley J.F., 1991, *ApJ* 376, 214
- Bardeen J.M., Petterson J.A., 1975, *ApJ* 195, L65
- Bastian T.S., Bridle A.H., (eds.) 1995, *The VLA development plan*, NRAO, Socorro, NM
- Beenakker C., Schöenberger C., 2003, *Physics Today* Vol. 56, issue 5, p. 37
- Belloni T., Hasinger G., 1990, *A&A* 230, 103
- Belloni T., Hasinger G., 1990, *A&A* 227, L33
- Belloni T., Klein-Wolt M., Méndez M., et al., 2000, *A&A* 355, 271
- Belloni T., Méndez M., King A.R., et al., 1997a, *ApJ* 488, L109
- Belloni T., Méndez M., King A.R., et al., 1997b, *ApJ* 479, L145
- Belloni T., Méndez M., van der Klis M., et al., 1996, *ApJ* 472, L107
- Benlloch S., 2003, Ph.D. thesis, Eberhard-Karls-Universität Tübingen
- Benlloch S., Pottschmidt K., Wilms J., et al., 2004, In: Kaaret P., Lamb F.K., Swank J.H. (eds.) *X-Ray Timing 2003: Rossi and Beyond.*, Melville, NY: American Institute of Physics, in press (astro-ph/0403070)
- Blandford R.D., Begelman M.C., 1999, *MNRAS* 303, L1
- Blandford R.D., Königl A., 1979, *ApJ* 232, 34
- Blandford R.D., Payne D.G., 1982, *MNRAS* 199, 883
- Blandford R.D., Znajek R.L., 1977, *MNRAS* 179, 433
- Blumenthal G.R., Gould R.J., 1970, *Reviews of Modern Physics* 42, 237
- Bolton C.T., 1972, *Nature* 235, 271
- Bondi H., 1952, *MNRAS* 112, 195
- Bondi H., Hoyle F., 1944, *MNRAS* 104, 272
- Bowyer S., Byram E.T., Chubb T.A., Friedman H., 1965, *Science* 147, 394
- Bridle A.H., Perley R.A., 1984, *ARA&A* 22, 319
- Brocksopp C., Fender R.P., Larionov V., et al., 1999a, *MNRAS* 309, 1063
- Brocksopp C., Fender R.P., Pooley G.G., 2002, *MNRAS* 336, 699
- Brocksopp C., Tarasov A.E., Lyuty V.M., Roche P., 1999b, *A&A* 343, 861
- Chandrasekhar S., 1931, *ApJ* 74, 81
- Churazov E., Gilfanov M., Revnivtsev M., 2001, *MNRAS* 321, 759
- Coppi P.S., 1999, In: *ASP Conf. Ser. 161: High Energy Processes in Accreting Black Holes.*, San Francisco: Astronomical Society of the Pacific, p. 375
- Corbel S., Fender R.P., Tzioumis A.K., et al., 2000, *A&A* 359, 251
- Crary D.J., Kouveliotou C., van Paradijs J., et al., 1996, *ApJ* 462, L71
- Cui W., Feng Y., Ertmer M., 2002, *ApJ* 564, L77
- di Matteo T., 1998, *MNRAS* 299, L15
- Done C., 2002, *Philosophical Transactions of the Royal Society of London, Series A* 360, 1967
- Dove J.B., Wilms J., Maisack M., Begelman M.C., 1997, *ApJ* 487, 759
- Dove J.B., Wilms J., Nowak M.A., et al., 1998, *MNRAS* 289, 729
- Durouchoux P., Fuchs Y., Rodriguez J., (eds.) 2003, *New Views on Microquasars*, Kolkata: Centre for Space Physics
- Esin A.A., McClintock J.E., Narayan R., 1997, *ApJ* 489, 865
- Fabian A.C., Rees M.J., 1979, *MNRAS* 187, 13P
- Falcke H., Beckert T., Markoff S., et al., 2002, In: Gilfanov M., Sunyaev R., Churazov E. (eds.)

- Lighthouses of the Universe. ESO Astrophysics Symposia, Berlin: Springer, p. 428
- Falcke H., Biermann P.L., 1995, *A&A* 293, 665
- Falcke H., Biermann P.L., 1996, *A&A* 308, 321
- Falcke H., Körding E., Markoff S., 2004, *A&A* 414, 895
- Falcke H., Markoff S., 2000, *A&A* 362, 113
- Fender R.P., 2001, *MNRAS* 322, 31
- Fender R.P., 2002, Relativistic Outflows from X-ray Binaries ('Microquasars'). In: Guthmann A., Georganopoulos M., Marcowith A., Manolakou K. (eds.) *Relativistic Flows in Astrophysics. Lecture Notes in Physics* 589, Berlin: Springer, p. 101
- Fender R.P., Garrington S.T., McKay D.J., et al., 1999, *MNRAS* 304, 865
- Fender R.P., Hendry M.A., 2000, *MNRAS* 317, 1
- Fender R.P., Pooley G.G., 2000, *MNRAS* 318, L1
- Fender R.P., Pooley G.G., Brocksopp C., Newell S.J., 1997, *MNRAS* 290, L65
- Fender R.P., Pooley G.G., Durouchoux P., et al., 2000, *MNRAS* 312, 853
- Fender R.P., Wu K., Johnston H., et al., 2004, *Nature* 427, 222
- Frank J., King A.R., Raine D.J., 1992, *Accretion Power in Astrophysics*, Cambridge Astrophysics Series 21, Cambridge: Cambridge University Press, 2nd edition
- Fried D.B., Castor J.I., 1982, *ApJ* 261, 293
- Galeev A.A., Rosner R., Vaiana G.S., 1979, *ApJ* 229, 318
- Gallo E., Fender R.P., Pooley G.G., 2003, *MNRAS* 344, 60
- Gierliński M., Zdziarski A.A., 2003, *MNRAS* 343, L84
- Gierliński M., Zdziarski A.A., Poutanen J., et al., 1999, *MNRAS* 309, 496
- Gies D.R., Bolton C.T., 1982, *ApJ* 260, 240
- Gies D.R., Bolton C.T., Thomson J.R., et al., 2003, *ApJ* 583, 424
- Gilfanov M., Churazov E., Revnivtsev M., 1999, *A&A* 352, 182
- Ginzburg V.L., Syrovatskii S.I., 1965, *ARA&A* 3, 297
- Gleissner T., Wilms J., Pooley G.G., et al., 2004a, In: Sion E., Tovmassian G. (eds.) *IAU Colloq. 194: Compact Binaries in the Galaxy and Beyond. Rev. Mex. Astron. Astrophys.*, Conference Series, in press (astro-ph/0312636)
- Gleissner T., Wilms J., Pooley G.G., et al., 2004b, *A&A*, in press (astro-ph/0407070)
- Gleissner T., Wilms J., Pottschmidt K., et al., 2003, in Durouchoux et al. (2003), p. 46
- Gleissner T., Wilms J., Pottschmidt K., et al., 2004c, *A&A* 414, 1091
- Golenetskii S., Aptekar R., Mazets E., et al., 2002, *IAU Circular* 7840, 1
- Gruber D.E., Blanco P.R., Heindl W.A., et al., 1996, *A&A* 120, C641
- Hannikainen D.C., Hunstead R.W., Campbell-Wilson D., Sood R.K., 1998, *A&A* 337, 460
- Harris R.W., Ledwidge T.J., 1974, *Introduction to noise analysis*, Applied Physics Series 7, London: Pion
- Hawking S.W., 1974, *Nature* 248, 30
- Hawking S.W., 1975, *Commun. Math. Phys.* 43, 199
- Hawking S.W., Ellis G.F.R., 1973, *The Large Scale Structure of Space-Time*, Cambridge: Cambridge University Press
- Heinz S., Sunyaev R.A., 2003, *MNRAS* 343, L59
- Herrero A., Kudritzki R.P., Gabler R., et al., 1995, *A&A* 297, 556
- Hjellming R.M., Han X., 1995, Radio properties of X-ray binaries., in Lewin et al. (1995), Ch. 7, p. 308
- Hjellming R.M., Johnston K.J., 1988, *ApJ* 328, 600
- Ichimaru S., 1977, *ApJ* 214, 840
- Jahoda K., Swank J.H., Giles A.B., et al., 1996, In: Siegmund O.H., Gummin M.A. (eds.) *EUV, X-Ray, and Gamma-Ray Instrumentation for Astronomy VII. Proc. SPIE* 2808, Bellingham, WA: SPIE, p.59
- Jernigan J.G., Klein R.I., Arons J., 2000, *ApJ* 530, 875
- Jones M.E., 1991, In: *IAU Colloq. 131: Radio Interferometry. Theory, Techniques, and Applications*. ASP Conf. Ser. 19, San Francisco: Astronomical Society of the Pacific, p.395
- Jones T.W., O'Dell S.L., Stein W.A., 1974, *ApJ* 188, 353
- Karttunen H., Kröger P., Oja H., et al., (eds.) 2003, *Fundamental Astronomy*, Berlin: Springer, 4th edition
- Keeping E.S., 1962, *Introduction to statistical inference*, Princeton: Van Nostrand
- King A.R., 1995, *Accretion in close binaries.*, in Lewin et al. (1995), Ch. 10, p. 419
- Klein-Wolt M., Fender R.P., Pooley G.G., et al., 2002, *MNRAS* 331, 745

- Koide S., Meier D.L., Shibata K., Kudoh T., 2000, *ApJ* 536, 668
- König M., Staubert R., Wilms J., 1997, *A&A* 326, L25
- Kortright J.B., 2001, Fluorescence Yields for K and L Shells. In: Thompson A.C., Vaughan D. (eds.) *X-ray Data Booklet*, Berkeley: Lawrence Berkeley National Laboratory, p. 1.28, electronically published at <http://xdb.lbl.gov/>
- Kotov O., Churazov E., Gilfanov M., 2001, *MNRAS* 327, 799
- Kraus J.D., 1986, *Radio Astronomy*, Powell: Cygnus-Quasar Books, 2nd edition
- Laplace P.S., 1796, *Exposition du Système du Monde*, Vol. II. Des Mouvements Réels des Corps Célestes, Paris: Duprat
- Larwood J., 1998, *MNRAS* 299, L32
- Laurent P., Titarchuk L., 1999, *ApJ* 511, 289
- Leahy D.A., Darbro W., Elsner R.F., et al., 1983, *ApJ* 266, 160
- Lehto H.J., 1989, In: Hunt J., Battrick B. (eds.) *Proc. 23rd ESLAB Symp. on two topics in X-ray astronomy*. ESA SP-296, Noordwijk: ESA Publications Division, p. 499
- Levine A.M., Bradt H., Cui W., et al., 1996, *ApJ* 469, L33
- Lewin W.H.G., van Paradijs J., van den Heuvel E.P.J., (eds.) 1995, *X-Ray Binaries*, Cambridge Astrophysics Series 26, Cambridge: Cambridge University Press
- Liu B.F., Yuan W., Meyer F., et al., 1999, *ApJ* 527, L17
- Livio M., Ogilvie G.I., Pringle J.E., 1999, *ApJ* 512, 100
- Lochner J.C., Swank J.H., Szymkowiak A.E., 1991, *ApJ* 376, 295
- Lyubarskii Y.E., 1997, *MNRAS* 292, 679
- Maccarone T.J., 2002, *MNRAS* 336, 1371
- Maccarone T.J., 2003, *A&A* 409, 697
- Maccarone T.J., Coppi P.S., 2002a, *MNRAS* 336, 817
- Maccarone T.J., Coppi P.S., 2002b, *MNRAS* 335, 465
- Maccarone T.J., Coppi P.S., Poutanen J., 2000, *ApJ* 537, L107
- Maraschi L., Ghisellini G., Celotti A., 1992, *ApJ* 397, L5
- Margon B., 1984, *ARA&A* 22, 507
- Markoff S., Falcke H., Fender R.P., 2001, *A&A* 372, L25
- Markoff S., Nowak M.A., Corbel S., et al., 2003, *A&A* 397, 645
- Marković D., Lamb F.K., 1998, *ApJ* 507, 316
- Marscher A.P., Gear W.K., 1985, *ApJ* 298, 114
- McClintock J.E., Remillard R.A., 2004, *Black Hole Binaries*. In: Lewin W.H.G., van der Klis M. (eds.) *Compact Stellar X-ray Sources*, Cambridge: Cambridge University Press, Ch. 4, in press (astro-ph/0306213)
- McConnell M.L., Zdziarski A.A., Bennett K., et al., 2002, *ApJ* 572, 984
- Meier D.L., 2001, *ApJ* 548, L9
- Meier D.L., Koide S., Uchida Y., 2001, *Science* 291, 84
- Merloni A., Fabian A.C., 2001, *MNRAS* 328, 958
- Merloni A., Fabian A.C., 2002, *MNRAS* 332, 165
- Michell J., 1784, *Philosophical Transactions of the Royal Society of London* 74, 35
- Milgrom M., 1979, *A&A* 76, L3
- Miller M.C., Colbert E.J.M., 2003, *Int. J. Mod. Phys. D*, submitted (astro-ph/0308402)
- Miller M.C., Lamb F.K., Psaltis D., 1998, *ApJ* 508, 791
- Mineshige S., Ouchi N.B., Nishimori H., 1994a, *PASJ* 46, 97
- Mineshige S., Takeuchi M., Nishimori H., 1994b, *ApJ* 435, L125
- Mirabel I.F., Dhawan V., Chaty S., et al., 1998, *A&A* 330, L9
- Mirabel I.F., Rodríguez L.F., 1994, *Nature* 371, 46
- Mirabel I.F., Rodríguez L.F., 1999, *ARA&A* 37, 409
- Mitsuda K., Inoue H., Koyama K., et al., 1984, *PASJ* 36, 741
- Miyamoto S., Kitamoto S., 1989, *Nature* 342, 773
- Miyamoto S., Kitamoto S., Iga S., et al., 1992, *ApJ* 391, L21
- Narayan R., Igumenshchev I.V., Abramowicz M.A., 2000, *ApJ* 539, 798
- Narayan R., Mahadevan R., Quataert E., 1998, *Advection-dominated accretion around black holes*. In: Abramowicz M.A., Björnsson G., Pringle J.E. (eds.) *Theory of Black Hole Accretion Discs*, Cambridge: Cambridge University Press, p. 148
- Narayan R., Yi I., 1995, *ApJ* 452, 710
- Narayan R., Yi I., Mahadevan R., 1995, *Nature* 374, 623
- Nayakshin S., Dove J.B., 2001, *ApJ* 560, 885

- Nayakshin S., Rappaport S., Melia F., 2000, *ApJ* 535, 798
- Ninkov Z., Walker G.A.H., Yang S., 1987, *ApJ* 321, 425
- Novikov I.D., Thorne K.S., 1973, *Astrophysics of Black Holes*. In: DeWitt C., DeWitt B. (eds.) *Black Holes — Les Astres Occlus.*, New York, London: Gordon and Breach, p. 345
- Nowak M.A., 2000, *MNRAS* 318, 361
- Nowak M.A., 2003, in Durouchoux et al. (2003), p. 11
- Nowak M.A., Dove J.B., Vaughan B.A., et al., 1998, In: Scarsi L., Bradt H., Giommi P., Fiore F. (eds.) *The Active X-ray Sky: Results from BeppoSAX and RXTE*. Nuclear Physics B Proc. Supp. 69, Amsterdam: Elsevier Science, p. 302
- Nowak M.A., Vaughan B.A., 1996, *MNRAS* 280, 227
- Nowak M.A., Vaughan B.A., Wilms J., et al., 1999, *ApJ* 510, 874
- Nowak M.A., Wagoner R.V., 1991, *ApJ* 378, 656
- Nowak M.A., Wilms J., Dove J.B., 2002, *MNRAS* 332, 856
- Oppenheimer J.R., Volkoff G.M., 1939, *Phys. Rev.* 55, 374
- Page D.N., Hawking S.W., 1976, *ApJ* 206, 1
- Penrose R., Floyd G.R., 1971, *Nature Physical Science* 229, 177
- Persi P., Ferrari-Toniolo M., Grasdalen G.L., Spada G., 1980, *A&A* 92, 238
- Petterson J.A., 1977, *ApJ* 216, 827
- Piran T., 1978, *ApJ* 221, 652
- Pooley G.G., Fender R.P., 1997, *MNRAS* 292, 925
- Pooley G.G., Fender R.P., Brocksopp C., 1999, *MNRAS* 302, L1
- Pottschmidt K., 2002, Ph.D. thesis, Eberhard-Karls-Universität Tübingen
- Pottschmidt K., König M., Wilms J., Staubert R., 1998, *A&A* 334, 201
- Pottschmidt K., Wilms J., Nowak M.A., et al., 2000, *A&A* 357, L17
- Pottschmidt K., Wilms J., Nowak M.A., et al., 2003, *A&A* 407, 1039
- Poutanen J., Fabian A.C., 1999, *MNRAS* 306, L31
- Poutanen J., Zdziarski A.A., 2003, in Durouchoux et al. (2003), p. 87
- Press W.H., Teukolsky S.A., Vetterling W.T., Flannery B.P., 1992, *Numerical Recipes in C: The Art of Scientific Computing*, Cambridge: Cambridge University Press, 2nd edition
- Priedhorsky W.C., Terrell J., Holt S.S., 1983, *ApJ* 270, 233
- Pringle J.E., 1981, *ARA&A* 19, 137
- Psaltis D., Belloni T., van der Klis M., 1999, *ApJ* 520, 262
- Psaltis D., Norman C., 2000, *ApJ*, submitted (astro-ph/0001391)
- Puls J., Kudritzki R.P., Herrero A., et al., 1996, *A&A* 305, 171
- Reynolds C.S., Nowak M.A., 2003, *Phys. Rep.* 377, 389
- Richer J.S., Shepherd D.S., Cabrit S., et al., 2000, *Molecular Outflows from Young Stellar Objects*. In: Mannings V., Boss A.P., Russell S.S. (eds.) *Protostars and Planets IV.*, Tucson: University of Arizona Press, p. 867
- Rosenfeld A., 1964, *Life* Vol. 56, issue 4, p. 11
- Rothschild R.E., Blanco P.R., Gruber D.E., et al., 1998, *ApJ* 496, 538
- Rybicki G.B., Lightman A.P., 1979, *Radiative Processes in Astrophysics*, New York: Wiley
- Savitzky A., Golay M.J.E., 1964, *Anal. Chem.* 36, 1627
- Schödel R., Ott T., Genzel R., et al., 2003, *ApJ* 596, 1015
- Schmidt M., 2002, *IAU Circular* 7856, 2
- Schwarzschild K., 1916, *Sitzber. Dtsch. Akad. Wiss. Berlin, Kl. Math. Phys. Tech.* 189
- Shakura N.I., Sunyaev R.A., 1973, *A&A* 24, 337
- Shapiro S.L., Lightman A.P., Eardley D.M., 1976, *ApJ* 204, 187
- Shapiro S.L., Teukolsky S.A., 1983, *Black Holes, White Dwarfs, and Neutron Stars*, New York: Wiley
- Shklovskii I.S., 1960, *Soviet Astronomy* 4, 243
- Shrader C.R., Titarchuk L., 1997, *Bulletin of the American Astronomical Society* 29, 1222
- Smith D.M., Heindl W.A., Swank J.H., 2002, *ApJ* 569, 362
- Spencer R., de la Force C., Stirling A., et al., 2001, *Ap&SS* 276, 255
- Stella L., Vietri M., 1998, *ApJ* 492, L59
- Stella L., Vietri M., 1999, *Physical Review Letters* 82, 17
- Stirling A., de la Force C., Spencer R., et al., 2001, *MNRAS* 327, 1273
- Stirling A., Spencer R., Garrett M., 1998, *New Astronomy Review* 42, 657
- Stone J.M., Pringle J.E., Begelman M.C., 1999, *MNRAS* 310, 1002

- Sunyaev R.A., Trümper J., 1979, *Nature* 279, 506
- Tanaka Y., Lewin W.H.G., 1995, Black-hole binaries., in Lewin et al. (1995), Ch. 3, p. 126
- Terrell N.J.J., 1972, *ApJ* 174, L35
- Thorne K.S., Price R.H., 1975, *ApJ* 195, L101
- Tout C.A., Pringle J.E., 1992, *MNRAS* 259, 604
- Unsöld A., Baschek B., 2002, *Der neue Kosmos*, Berlin: Springer, 7th edition
- Uttley P., McHardy I., Vaughan S., 2003, In: *Active Galactic Nuclei: From Central Engine to Host Galaxy*. ASP Conf. Ser. 290, San Francisco: Astronomical Society of the Pacific, p. 131
- Uttley P., McHardy I.M., 2001, *MNRAS* 323, L26
- van der Klis M., 1989, In: Ögelman H., van den Heuvel E.P.J. (eds.) *Timing Neutron Stars*. NATO ASI C262, Dordrecht: Kluwer Academic Publishers, p. 27
- van der Klis M., 1995, Rapid aperiodic variability in X-ray binaries., in Lewin et al. (1995), Ch. 6, p. 252
- van der Klis M., 2000, *ARA&A* 38, 717
- van der Klis M., 2001, *ApJ* 561, 943
- van der Laan H., 1962, *MNRAS* 124, 125
- van Straaten S., van der Klis M., Méndez M., 2003, *ApJ* 596, 1155
- Wijnands R., van der Klis M., 1999, *ApJ* 514, 939
- Wilms J., Nowak M.A., Dove J.B., et al., 1999, *ApJ* 522, 460
- Wilms J., Reynolds C.S., Begelman M.C., et al., 2001, *MNRAS* 328, L27
- Witt H.J., Czerny B., Życki P.T., 1997, *MNRAS* 286, 848
- Wolfram S., (ed.) 1986, *Theory and Applications of Cellular Automata*, Advanced Series on Complex Systems 1, Singapore: World Scientific
- Young A.J., Fabian A.C., Ross R.R., Tanaka Y., 2001, *MNRAS* 325, 1045
- Zdziarski A.A., Lubiński P., Gilfanov M., Revnivtsev M., 2003, *MNRAS* 342, 355
- Zdziarski A.A., Poutanen J., Paciesas W.S., Wen L., 2002, *ApJ* 578, 357
- Zhang S.N., Cui W., Harmon B.A., et al., 1997a, *ApJ* 477, L95
- Zhang S.N., Mirabel I.F., Harmon B.A., et al., 1997b, In: Dermer C.D., Strickman M.S., Kurfess J.D. (eds.) *AIP Conf. Proc. 410: Proceedings of the Fourth Compton Symposium.*, Melville, NY: American Institute of Physics, p. 141
- Zhang W., Jahoda K., Swank J.H., et al., 1995, *ApJ* 449, 930
- Zurita C., Casares J., Shahbaz T., 2003, *ApJ* 582, 369
- Życki P.T., 2003, *MNRAS* 340, 639

Acknowledgments

First of all, I would like to thank my advisor Prof. Dr. Rüdiger Staubert for the trust he showed in me when accepting me as a Ph.D. student although I was new to Tübingen. The work on this thesis benefited from many helpful discussions and furthering suggestions. His well-balanced way of leading the X-ray group accounted to a great extent for the good atmosphere at the institute.

Dr. Jörn Wilms continuously provided input of new ideas and showed me that doing astronomy research is both privilege and fun. His experience and optimism was a great asset for our cooperation.

Thanks also go to Dr. Katja Pottschmidt who introduced me into the realm of monitoring Cygnus X-1. Our joint work was enriched by her foresight and reliability.

The spirit of an institute is formed by its members. I was lucky to be together with friendly people who helped me with science, computers, and administration. As representatives of all the names I would have to list here, I only want to mention Ingo Kreykenbohm and Heinz Lenhart, who always assisted me whenever I needed them with the computer network. Besides work, I shared unforgettable recreational experiences with my colleagues, ranging from espresso to playing in a rock band and running a pico light-year.

Since astronomy is a very international field, I enjoyed meeting and collaborating with a lot of people from around the globe. Among other researchers, I should particularly mention Dr. Michael A. Nowak, Dr. Sera Markoff, and Dr. Sebastian Heinz at MIT, Dr. Philip Uttley at Southampton, Dr. Guy G. Pooley at Cambridge (UK), and Marc Klein-Wolt and Dr. Robert P. Fender at Amsterdam who kindly made available the data of GRS 1915+105. Their contributions considerably improved this work.

I am also much obliged to my wife's aunt Vaso and to my parents for helping out at home when I was away for conferences.

To my wife Maria and my daughters Eleni and Sophia, I owe a debt of gratitude for all the hours stolen from them.

Lebenslauf

geboren am 9.9.1968 in Weiden i. d. OPf.

Familienstand: verheiratet, 2 Kinder

Schule

09.1974–07.1978 Grundschule Bechtsrieth
 09.1978–06.1987 Augustinus-Gymnasium Weiden
 26.6.1987 Abitur

Wehrdienst

10.1987–12.1988 3./Panzerartilleriebataillon 105, Weiden

Studium der Physik

10.1988–10.1990 Universität Regensburg
 25.10.1990 Vordiplom
 11.1990–09.1994 Bayerische Julius-Maximilians-Universität Würzburg
 09.1991–05.1992 State University of New York at Albany (SUNY)
 17.5.1992 Master of Science (SUNY)
 07.1993–07.1994 Diplomarbeit über „IR-Strahlungstransport in dispersen Medien“ unter Anleitung von Herrn Prof. Dr. J. Fricke am Bayerischen Zentrum für Angewandte Energieforschung Würzburg (ZAE Bayern e.V.)
 23.9.1994 Diplom
 04.2001–03.2004 Anfertigung der Dissertation mit dem Titel „X-ray and Radio Variability of Cygnus X-1“ unter Anleitung von Herrn Prof. Dr. R. Staubert am Institut für Astronomie und Astrophysik (IAAT) der Eberhard-Karls-Universität Tübingen

Praktische Tätigkeiten

1993–1994 Wissenschaftliche Hilfskraft am Physikalischen Institut der Universität Würzburg
 08.1994–05.1995 Wissenschaftlicher Mitarbeiter am Bayerischen Zentrum für Angewandte Energieforschung Würzburg (ZAE Bayern e.V.)
 07.1995–09.1999 Physiker in der Abtl. Forschung & Entwicklung der Ingenieurgesellschaft Schmidt Reuter Partner, Köln

- 30.7.1999 Staatlich anerkannter Sachverständiger für Schall- und Wärmeschutz (Ingenieurkammer-Bau NRW)
- 10.1999–09.2000 Projektleiter bei Ebert-Ingenieure Nürnberg
- 01.2001–03.2001 Wissenschaftliche Hilfskraft am Institut für Astronomie und Astrophysik Tübingen (IAAT)
- 04.2001–03.2004 Wissenschaftlicher Angestellter am Institut für Astronomie und Astrophysik Tübingen (IAAT)

Meine akademischen Lehrer waren neben anderen die Professoren und Dozenten Dres.:

Astronomie und Astrophysik: J. Isserstedt, R. Staubert, K. Werner, J. Wilms

Chemie: G. Gliemann

Experimentelle Physik: M. Alam, E. Bangert, R. Bonart, J. Fricke, W. Hink, H. Langhoff, M. Maier

Mathematik: G. Tamme, R. Warlimont

Theoretische Physik: T. Das, H. Fraas, A. Inomata, J. Kimball, R. Oppermann, U. Schröder